UNIVERSITÀ DI PISA

DEPARTMENT OF CHEMISTRY AND INDUSTRIAL CHEMISTRY
RESEARCH DOCTORATE SCHOOL IN BIOLOGICAL AND MOLECULAR SCIENCES

PH.D. IN BIOMATERIALS

Advaced Microtomographic Techniques for *in vitro* and *in vivo* evaluation of Biomaterials in Orthopedic Research

Annapaola Parrilli

SUPERVISOR
Prof. Roberto Giardino

TUTOR
Dr. Milena Fini

Biocompatibility, Technological Innovations and Advanced Therapies Laboratory
Rizzoli Research and Innovation Technology Department
Rizzoli Orthopaedic Institute – Bologna

2012 - 2014

An experiment is a question which science poses to Nature,
and a measurement is the recording of Nature's answer.

Max Planck

Acknowledgments

Special thanks to my supervisor prof. Roberto Giardino, who offered me the opportunity to start my research activity at the Rizzoli Orthopaedic Institute and gave me constant encouragement and invaluable guidance through the years.

Thanks to my tutor Dr. Milena Fini, who has made this research possible and helped me in the various aspects of this Ph.D study sharing her knowledge on orthopedics and regenerative medicine issues.

Thanks to prof. Roberto Toni, for the support and the important feedback given throughout the Ph.D study.

Thanks to all the researchers of the Preclinical and Surgical Studies Laboratory and of the BITTA Laboratory of the Rizzoli Orthopaedic Institute.

Contents

List of Figures

micro-CT scan detail of a sample at 8 weeks of experimental time. c) Micro-CT sections of a sample at 8 weeks of experimental time. No sign of mineralization are present in both sides.

Figure 13.1 – Box plot of results of a) BMD and b) TMD of the study for the evaluation of bone quality in terms of mineral content in a study of osteoarthritis treatment in a large animal model with engineered hyaluronic acid scaffolds.

List of Tables

List of Abbreviations

°C	Celsius
µCT	Micro-Computed Tomography
2D	Two-dimensional
3D	Three-dimensional
4D	Four-dimensional
A/D	Analog/Digital conversion
AIFA	Italian Medicines Agency
ALVAL	Aseptic Lympocytic Vasculitis-Associated Lesions
ASBMR	American Society for Bone and Mineral Research
Av.Obj.ECD	Average object equivalent circle diameter per slice
BHR	Birmingham Hip Resurfacing
BIC	Bone to Implant Contact
BMD	Bone Mineral Density
BMI	Bone Mineralization Index
BSE	Backscattered Electron
BV/TV	Bone Volume
CCD	Charge Coupled Device
CLSM	Confocal Laser Scanning Microscope
Cm.Th	Cement Thickness
CMC	Carboxymethylcellulose
CMC-NPs	Carboxymethylcellulose with iron magnetic NP
CMM	Coordinate Measuring Machine

CS	Cranial Substitute
CT	Connective Tissue
DA	Degree of anisotropy
DABCO	1,4-diazabicyclo[2.2.2]octane
DAPI	4′,6-diamino-2-phenylindole
DNA	Deoxyribonucleic acid
Ecc	Mean eccentricity
EDTA	Ethylenediaminetetraacetic acid
F-actin	Cytoskeleton filamentous actine
FBP	Filter Back Projection
FBS	Fetal Bovine Serum
FD	Fractal dimension
FE	Finite Element
Fib.Tis.Th	Thickness of Fibrous Tissue
FITC	Fluorescein isothiocyanate
FOV	Field Of View
Fr.I	Fragmentation Index
GEL	gelatin
GEL-HA10	GEL with 10% Hydroxyapatite
HA	Hydroxyapatite
hADSC	primary human adipose derived stromal cells
hMSC	human mesenchymal stromal cells
HR	Hip Resurfacing arthroplasty
HV	Vickers Hardness Index
HYAFF	hyaluronic scaffold
JPG	Joint Photographic Experts Group File Format
LA	Left Anterior
LP	Left Posterior
Mat.Conn	Material Connectivity
Mat.p.ESDA	Material diameter as surface equivalent sphere diameter
Mat.p.ESDV	Material diameter as volume equivalent sphere diameter
Mat.p.V	Average Material granules Volume
Mat.V/TV	Material Volume

MBS	Multiphasic Bone Substitute
micro-CT	Micro-Computed Tomography
MIP	Maximum Intensity Projection
MMI (polar)	Mean polar moment of inertia
MMX	medial meniscectomy
N	number
NB	Newly formed Bone
New BV/TV	newly formed Bone Volume
NP	Nanoparticles
Obj.Ar	Mean total section object area
Obj.N	Number of objects
Obj.N	Mean number of object per slice
Obj.S	Object surface
Obj.S/Obj.V	Object surface/volume ratio
Obj.S/TV	Object surface density
Obj.V	Object Volume
Obj.V/TV	Percent Obj. Volume
PB	Peri-implant Bone
PBS	Phosphate Buffered Saline
PCL	Polycaprolactone
PE	Polyethylene
PhD	Doctor of Phylosophy
PLY	Polygon file format
PMMA	Polymethylmetacrylate
Po(cl)	Closed porosity
Po(op)	Open porosity
Po(tot)	Total porosity
PoreSP	Pore Separation
PoreTh	Pore Thickness
PoreV/TV	Porosity
R^2	Coefficient of determination
RA	Right Anterior
RFU	Relative Fluorescence Unit

RGBA	Red Green Blue Alpha
ROI	Region of Interest
RP	Right Posterior
S/N	Signal to Noise ratio
s/w	software
SD	Standard Deviation
SEM	Scanning Electron Microscopy
SMI	Structure model Index
SSD	Shaded Surface Display
St.N	Structure number
St.Sp	Structure separation
St.Sp(pl)	Structure separation (plate model)
St.Th	Structure thickness
St.Th(pl)	Structure thickness (plate model)
STL	Stereolitography
Tb.N	Trabecular Number
Tb.Sp	Trabecular Separation
Tb.Th	Trabecular Thickness
TCP	Tricalcium phosphate
TG	Thermoplastic gelatin
THR	Total Hip Replacement
TIFF	Tagged Image File Format
TMD	Tissue Mineral Density
TTCP	Tetracalcium phosphate
TV	Tissue Volume or VOI Volume
v/v	Volume to volume
VOI	Volume Of Interest
VR	Volume Rendering
w/w	Weight to weight
Z	Atomic number

PART I
INTRODUCTION

Chapter 1
Preface

Over the recent years, the micro-computed tomography (micro-CT) has increasingly become a necessary technique for characterization and evaluation of biomaterials used in orthopedic research due to its intrinsic ability to provide a huge amount of data and a complete volumetric visualization. Micro-CT (Figure 1.1) is a non-destructive technique that represents an evolution of the computerized tomography normally used in medicine. Besides, with its micron (μm) level of resolution, it is set, among the non-destructive techniques, as one of the most advanced, due also to the constantly evolving technological advancements and to the elevated power of calculation of computers [1]. In particular, the volumetric micro-CT methods have some advantageous characteristics such as the relatively short time of each specimen scanning, the ability to evaluate specimens without touching their surfaces and the capability to analyse the specimens structures also locally. These micro-CT characteristics allow the evaluation of implanted biomaterials by studying the three-dimensional (3D) structure and their efficacy by studying the regenerated tissue morphology. In the only orthopedic research, microtomography can be used for numerous typologies of evaluation. For example biomaterials analysis before the implant to evaluate porosity or mechanical characteristics; analysis of metallic devices in which it is very important the study of bone growth through regeneration and osteointegration; analysis of polymeric or ceramic devices that are usually studied for regeneration in defects and for bone losses. Besides, after the

implantation of a biomaterial it is important not only the quantitative analysis of bone growth, but also the quality of the regenerated bone.

The microtomographic techniques, which are used both during the acquisition (scanning and reconstruction) of the sample and during the analysis of the produced images, are not, however, applicable in a standard and repeatable way to any kind of biomaterials because of their different attenuation of the X radiation. In addition, other fundamental and critic steps in micro-CT analysis stems from finding an adequate gray value threshold for image segmentation because all dimensional measurements using micro-CT are based on the determination of the material boundary.

The main aim of this PhD research was to develop innovative techniques and procedures of 3D image analysis for the characterization of polymeric, ceramic and metal biomaterials used in various fields of bone tissue preclinical research. The project consisted in assessing new reliable experimental procedures, widening the knowledge and elaboration of new interpretative models of the bone regeneration mechanisms and creating more sophisticated 3D graphic rendering that allow the virtual exploration of the analysed samples internal structure.

Figure 1.1 *– Micro-CT system of the Preclinical and Surgical Studies Laboratory at Rizzoli Orthopaedic Institute in Bologna, Italy.*

Chapter 2
Microtomography

Micro-CT is a non-destructive technique that represents an evolution of the computerized tomography (CT) normally used in medicine. It can reach high resolutions (micron range) and allows the visualization of the internal structures of the objects [2]. The conventional microscopy (optical or electron) allows to visualize bi-dimensional images only of the sample surfaces. Theoretically, a 3D model of the object structure can be interpolated from the bi-dimensional information of very thin sections visualized by a microscope. This method, besides being cumbersome, is also not very reliable because the real structure of the object may have been altered by the technique used for sample preparation and, furthermore, the distance between the sections is usually too coarse to avoid loss of 3D information.

Currently, one of the demands warned more strongly in the productive cycle and in research is the development of non-destructive methodologies for the analysis of the microstructure of different types of materials. Micro-CT, with its resolutions at the level of μm, is placed between the non-destructive techniques as one of the most advanced, due especially to the continuously evolving technological developments [1].

Micro-CT is based on the interaction of X-rays with matter and it derives directly from the radiographic technique in which the complete 3D internal structure of an object is visualized in a bi-dimensional projection. This happens because the intensity of the non-absorbed radiation, after the sample crossing, is recorded on the plan of a detector

set at the opposite side of the X-ray source [3]. The principal disadvantage of radiography is to overlap the different internal structures in only one bi-dimensional projection mixing, in this way, the information concerning the depth.

The tomography uses the radiographic images of the object gotten at different angles. For example, in Figure 2.1 two images taken at an angle of 0° and an angle of 90° of a microtomographic scan are shown. Afterwards, using reconstruction algorithms based on the technique of Filter Back Projection (FBP), virtual sections of the internal structure of the object can be created. With a number of consecutive different reconstructed sections it is possible a 3D visualization of the object. The obtained microtomographic consecutive sections are a series of images with different gray levels. These gray levels of every section give a map of the distribution of the absorption coefficients of the X-rays related to the analyzed sample. Such coefficients depend on the material density, on the atomic number of the elements that constitute it and on the incidental energy used.

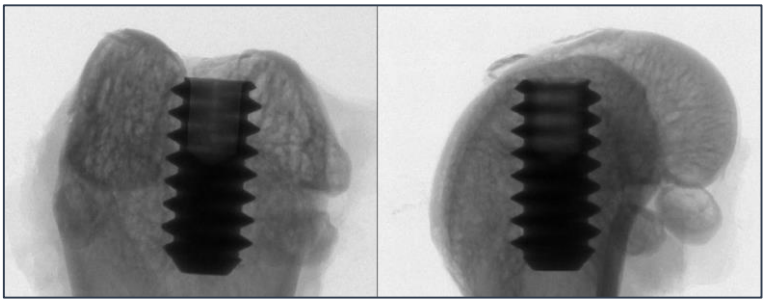

Figure 2.1 *- Images at 0° step and at 90° step of micro-CT scanning.*

Over the years, the development of CT equipment, from the first tomographic scanner realized by Godfrey N. Hounsfield in 1972 [4] onwards, allowed to reach a micrometric resolution and thus allowed the diffusion of the CT, first utilized only in medicine, also in the scientific and industrial fields [5]. In fact, the areas of application include biomedical research, science of biomaterials, development and production of drugs, dental research, electronic components research,

geology, zoology, botany, construction materials research, paper manufacture and many others. In the only biomedical and dental research, micro-CT can be used for numerous typologies of evaluations. With regard to biomaterials, analysis could be carried out for example before the implantation to evaluate the porosity or the mechanical characteristics. Besides, the analysis of metallic devices after implantation, used frequently in orthopedics, is usually based on the study of bone growth, of bone regeneration and osteointegration, while the analysis of polymeric or ceramic devices is based principally on the regeneration in defects and the bone losses evaluation. Moreover, after the biomaterial implantation, it is important not only the quantitative analysis of bone growth, but also an evaluation of the quality of the regenerated bone.

Using micro-CT, virtual 3D models of the analyzed object can be created (Figure 2.2). This kind of visualization gives a huge help to understand the structures that are normally studied and observed in 2D images typical of histology or of classical radiology. The models can be also used for creating movies of the analyzed object in movement, or as a base for prototypes in tissue engineering. Therefore, micro-CT results to be, especially for the preclinical evaluations of implant materials destined to the musculoskeletal system, an important and valid non-destructive method. This technique results to be also very useful to characterize the devices both in pre-implant phase and in the explant phase, in order to appraise possible deformations and/or degradations of the samples [1].

Figure 2.2 *- 3D model of a femur head with an insight of the internal trabecular structure*

In the last years, the progress in manufacturing micro-CT technology has led to sophisticated *in vivo* high-resolution low-dose X-ray scanners with details detectability down to 9 microns inside small and medium laboratory animals (rats, mice and rabbits) and integrated physiological monitoring for gating and time resolved tomography.

2.1 General principles

The fundamentals concerning instrumental aspects and the theory of the physical principles of micro-CT systems are essential for a correct use and for obtaining the best results in terms of both image quality and morphological measurements. To study the interaction between bone and implanted biomaterials is indeed important to set X-ray source voltage and image reconstruction corrections depending on the involved material attenuation, i.e. the reduction of the intensity of the radiation due to the passage through the matter.

2.1.1 X-rays source

An X-ray source, shown in Figure 2.3, is composed of a target-anode complex and a cathode placed under vacuum within a tube (X-ray tube). When the cathode filament is heated, electrons are ejected from its surface (thermionic emission). The intensity of the ionic current that passes in the tube is a function of the number of electrons emitted from the filament. The potential tension (voltage) between the anode and the cathode causes the electrons to accelerate towards the anode. When these electrons collide with the atoms of the target, generally made of tungsten, they transfer their kinetic energy to the anode. The electrons interact with both the orbital electrons and the nucleus of the tungsten atoms and these interactions conduct to the conversion of kinetic energy into heat energy and electromagnetic energy, the latter in form of X-rays. Generally, more than 99% of the kinetic energy is converted into thermal energy, leaving only 1% available for the production of X-rays.

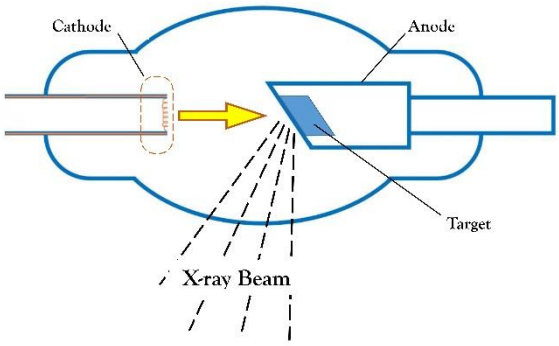

Figure 2.3 *– X-ray source scheme.*

The amount of X-rays or photons emitted from the target is a function of the number of electrons emitted from the filament: the greater the number of the incident electrons, the greater is the number of the atoms interested and the greater is the number of X-rays emitted. The energy of the emitted X-rays is instead a function of the only kinetic energy of the incident electrons, and thus of the potential tension between anode and cathode.

2.1.2 Interactions between X-ray and the matter

Theoretically, X-rays interact with matter in four ways: they can interact with the atomic electrons, with the atomic nuclei, with the electric fields associated to the electrons and/or atomic nuclei, and with the meson field surrounding nuclei [2]. Moreover, there are only three different possible situations because of an interaction between X-rays and matter: the incident beam is fully absorbed, the incident X-ray beam scatters elastically, or it scatters inelastically. In this way, twelve different ways in which photons can interact with matter are theoretically possible, but some of those interactions have not yet been physically observed.

The main photon-matter interactions involved in the creation of the images obtained by scanning objects through X-rays are: the photoelectric effect, the Compton scattering and the pair production. Their incidence

depends on the atomic number (Z) of the material (the absorber) and on the photon energy. The other processes are usually either irrelevant or energetically forbidden. The photoelectric effect is the complete absorption of a photon by an atom with the emission of an orbital electron (photoelectron). If the energy transferred from the photon to the electron is higher than the electron-nucleus bound energy, the electron is torn from its orbit and projected outward. The removal of the electron of the atom causes its rearrangement resulting in the formation of an X-photon. The photoelectric effect is predominant at low energy of X radiation and depends strongly on the atomic number of the absorber. The Compton or incoherent scattering is a process in which an X-photon interacts with an electron weakly bound to the nucleus. The effect is a transmission of energy to the electron (Compton electron) and the production of a photon, with reduced energy, that diffuses in a direction different from the incident one. The Compton scattering is predominant at medium energies of X radiation and varies directly with the atomic number per mass unit of the absorber.

The pair production is the process that occurs when the incident X-ray beam interacts with the strong electric field around the nucleus, is completely absorbed and determines the creation of an electron - positron couple. It is the predominant process for radiation energies exceeding 1.022 MeV (out of the energy range normally used in microtomography).

2.1.3 X-ray attenuation

For monochromatic X-rays, the attenuation, i.e. the reduction of the intensity of the radiation due to the passage through the matter, depend to the linear attenuation coefficient specific for every material [2]. The attenuation is given by the Beer-Lambert law that says that each layer with the same thickness absorbs an equal fraction of the radiation that passes through. Mathematically it is expressed by:

$$\frac{dI}{I} = -\mu \, ds \tag{2.1}$$

with I the incident radiation intensity, dI/I the fraction of the radiation removed from the beam when it crosses a thin layer (ds) of the material, and μ the linear attenuation coefficient [6].

After integration, the formula becomes more familiar:

$$I = I_0 e^{-\mu s} \tag{2.2}$$

with I_0 the original intensity not attenuated and I the intensity of the beam after it passed through a material with a thickness of s.

If the X-rays pass through a non-homogeneous material, the equation is expressed in the following general form:

$$I = I_0 e^{-\int \mu(s)\ ds} \tag{2.3}$$

The line integral is taken along the direction of X-ray propagation and $\mu(s)$ is the linear attenuation coefficient at each point of the beam path.

In CT, the fraction of the transmitted intensity, I/I_0, is measured for a large number of radiation paths through the scanned object. This fraction allows obtaining a set of integrals, which will serve as inputs to the reconstruction algorithm [2]. Primary integrals will have this form:

$$\int \mu(s)\ ds = -\ln\left(\frac{I}{I_0}\right) \tag{2.4}$$

2.1.4 X-ray detectors

After passing through the object, the X-rays are registered by a detector system. An X-ray detector is composed mainly by three parts: a CCD (acronym of Charge Coupled Device) camera, that provide the digital images; the scintillator, that is used to convert X-rays into visible light

photons; and optical fibers, that are used because the difference in size between the emitting material and the CCD sensor.

The resolution is a crucial element of any system that captures images. In the case of CCD sensors, it is determined by the size of the pixels, i.e. the sensitive component parts of the chip. Substantially a CCD camera consists of three basic elements: the sensor or chip, the control electronics and the cooling system. The latter has the task of minimize the noise due to the environment temperature [7]. The chip is essentially constituted by electrodes made of polycrystalline silicon (gate) separated by a silicon substrate (the sensitive part) by a thin insulating layer of silicon dioxide. The photons that interact with the silicon generate electrons that are accumulated in microscopic wells. A pixel, which is the fundamental component, like in a mosaic, of the final image, is an image element that corresponds to a well. In fact, in practice, the two terms often overlap. The greater the number of photons hitting the pixel, the greater is the charge accumulation. Once the exposure has been completed, the data packets of recorded charges are transferred to the control electronics (i.e. the readout station) in order to be processed. The control electronics is thus the stage that has the task of collecting information from the chip and transforming it into numbers, in order to construct the digital image. The analog/digital conversion (A/D) of the signal may occur with different precision depending on the converter used (Table 2.1).

Converter	Grayscale levels
8 bit	256
10 bit	1024
11 bit	2048
12 bit	4096
14 bit	16384
16 bit	65536

Table 2.1 *– A/D conversion*

2.2 Acquisition and image Reconstruction

During the acquisition, the object is rotated until 180° or 360° with fixed intervals of rotation. A projected image (transmitted image similar to a radiograph) is acquired at each angular position. The acquisition data (projections) are saved usually as 16-bit or 12-bit files. The dataset after the scanning process consists of a set of images of X-ray transmission. The number of files after the acquisition depends on the rotation steps and the total degree of rotation chosen.

When the acquisition is completed, the micro-CT reconstruction process can start. The images obtained from acquisition (the projections) are used for the reconstruction of the analyzed object in virtual slices dataset.

In the case of acquisitions X-ray, the image contains information on the reduction of intensity that occurs when the radiation passes through the 3D object. Since the absorption responds to an exponential law (the Beer-Lambert, section 2.1.3), the information of linear absorption can be restored from the projection images making the logarithm. To minimize errors in the reconstruction phase, an average of the initial data can be used, or the exposure time can be optimized in order to achieve the most representative information and improve the signal to noise ratio (S/N). An even more effective method for reducing the noise in the reconstruction process is the selection of corrections or filtering functions before the back projection, i.e. the reconstruction algorithm [8]. In the X-ray microtomography, the information is detected from voxels with very small physical dimensions. The right choice of parameters for the noise reduction becomes thus very important.

First, a raw data of the cross-section is generated using the reconstruction algorithm. Then, the cross-section is reconstructed as a matrix containing the attenuation values after reconstruction, and turned into an image with usually 256 gray values (8 bits).

2.3 Factors influencing micro-CT image quality

Some factors and procedure steps are important and can be modified in order to optimize the image quality. These factors imply the correct positioning of the sample inside the analyzing chamber, the right choice of settings for the X-ray beam emitted, and the choice of the right filters for a correct microtomographic reconstruction of the sections.

Positioning the sample on the support requires the use of an adhesive material such as plastic or double-sided tape. If the sample consists of biological tissue not included (normally in methacrylate resin or paraffin), an additional “custom-made” support in polystyrene (i.e a material that is practically radiolucent to X-rays) is created to secure the sample on the metal support. Besides, the sample has to be placed in the center of the support to keep it in the field of view (FOV) during the full rotation and to achieve the highest possible magnification. Once the sample is positioned correctly for scanning, it is important to ensure enough absorption contrast.

The emission spectrum is radically changed by any filtration and the change is a function of the thickness and the filter material. The filtration has the effect of eliminating the lower energy radiation (defined "soft"), and of reducing the emission intensity of the remaining radiation. For example, the option "no filter" is typically used for objects with a low X-ray absorption, i.e. samples with compositions having a low average of atomic number. On the other side, different metal filters can be used to cut the X-ray radiation with low energy and reduce the non-linear absorption to X-rays ("beam hardening") in dense materials. The beam hardening is a phenomenon related to the fact that the surface layer of dense materials works as a filter for X-rays to the rest of the sample [9-10]. In fact, the polychromatic character of the used X-ray spectrum implies that the linear attenuation coefficient μ of the material changes non-linearly along the propagation path. Low energy photons are attenuated more rapidly than high-energy photons while they are

penetrating materials and, then, the ray beam becomes harder. The beam hardening causes cupping artifacts on the reconstructed images [11-13]. This means that the reconstructed value in the central area of a homogeneous analyzed object is lower than in the proximity of its surface border, looking like a density change depending on the position in its volume [12]. This reduces the information relative to the center of the samples and distorts the distribution of the reconstructed density. Therefore, the surface could be seen denser than it should be and the internal parts appear less dense (Figure 2.4). Metal filters, such as aluminum or copper filters, can cut the "soft" radiation and let pass through only the high-energy, which works in a similar manner on the surface and in the inner parts. However, cutting a part of the X-ray radiation the number of photons detected will be reduced and therefore the filtration has to be compensate with a longer exposure time and consequently with a longer acquisition cycle.

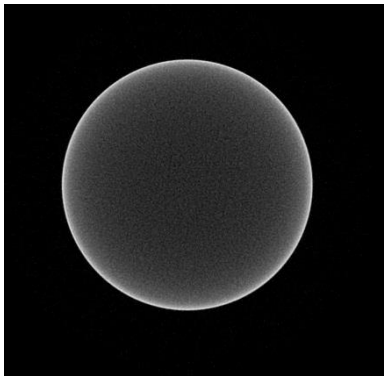

Figure 2.4 *– Beam hardening effect. Due to the severe beam hardening effect occurred, the reconstructed CT section of a Zirconium dioxide (ZrO_2) femoral head component of a prosthesis appears with the outer surface much lighter than the inner core.*

Other parameters that can be modified to suit the needs for the acquisition in a micro-CT analysis are the frame averaging and the rotation angle. The frame averaging improves the image quality making an average of several projections captured at every angular position. The value is given by the number of frames, which means that increasing the

number of frames will increase the quality but the acquisition time will be longer. Making a 360° rotation instead of a 180° rotation can reduce the asymmetric artifacts of dense samples surrounded by materials with low absorption. Increasing the rotation angle will increase the scan time by almost double.

Regarding the reconstruction process, some corrections can be applied such as ring artefacts correction (Figure 2.5), post-alignment correction (Figure 2.6) and beam hardening correction.

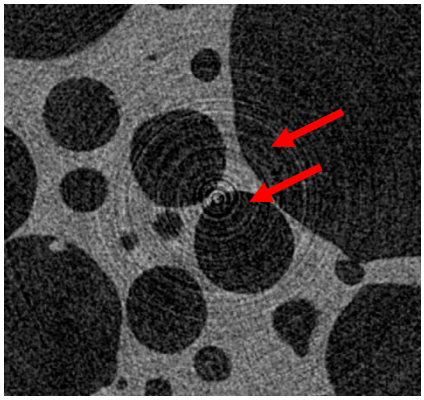

Figure 2.5 *– Ring artefacts are highlighted with the red arrows in a reconstructed section of a ceramic porous biomaterial for bone regeneration.*

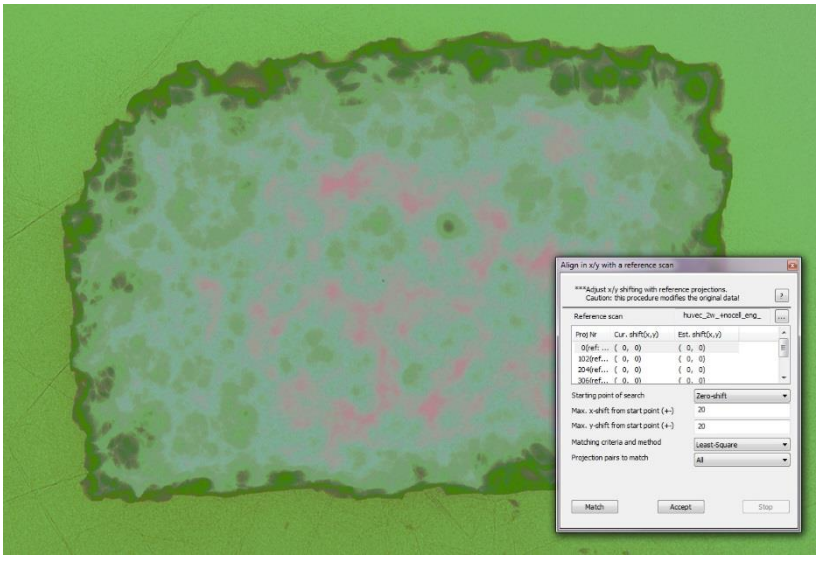

Figure 2.6 *– Post-alignment correction applied to projections of a ceramic porous biomaterial for bone regeneration.*

Chapter 3
Biomaterials for orthopedics

Tissue engineering and regenerative medicine are one of the most promising areas of research and combine the disciplines from engineering to life sciences [14-15]. Research in this field is allowing the creation of biological tissue replacement using innovative biomaterials with or without *in vitro* seeded cells [16]. In fact, biomaterials are often used as scaffolds for the cells and must be capable of promoting cell growth and stimulate differentiation within the tissue that has to be regenerated. Since the properties of the material depend on the application site, a comprehensive knowledge of the structure of the tissue to repair is crucial. In fact, the properties of the biomaterial should be as similar as possible to the tissue to be replaced.

3.1 The bone

Bone tissue is a type of connective tissue with a remarkable regenerative capacity. However, there are clinical conditions in which the bone is not able to self-regenerate or, at least, not in a physiologically appropriate time. These conditions are for example the skeletal reconstruction of large bone defects derived by trauma, infection or oncological disease, situations of avascular necrosis, atrophic non-unions or osteoporosis in which the regeneration process is compromised [17]. In relation to these clinical problems, new therapeutic strategies that

allow the regeneration of bone tissue even in cases where it would not occur spontaneously have been developed [18].

Understanding the biology of bone tissue, at the macroscopic and microscopic structure level, the cellular components, and the mechanisms of bone formation and bone remodeling is fundamental.

3.1.1 Bone structure

Bone tissue is a specialized connective tissue consisting of cells embedded in a mineralized extracellular matrix that is able to confer resistance to mechanical stress [19].

Mature bone tissue is composed of collagen lamellae arranged in parallel and cemented by amorphous substance, which make it more resistant to traction. It can be divided into two categories with different architecture: cortical bone tissue and trabecular bone tissue (Figure 3.1).

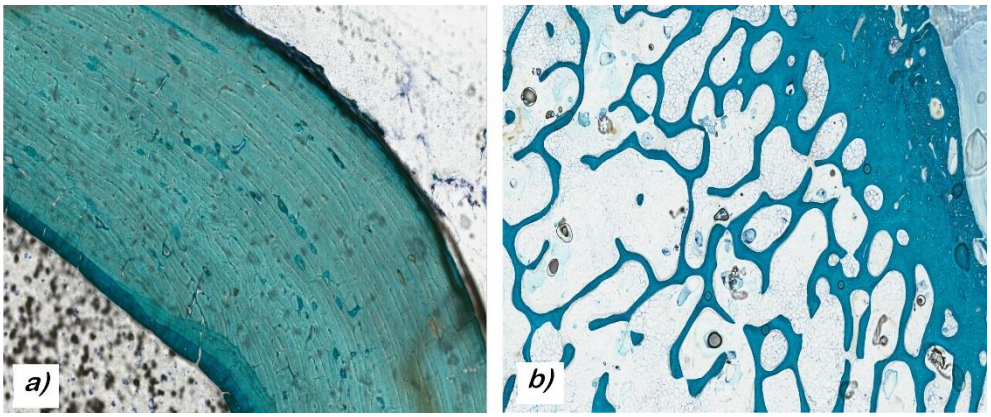

Figure 3.1 *– Bone structures. a) Section of cortical bone of sheep tibia colored with Fast green and at 3,5X of magnification. b) Section of trabecular bone of sheep iliac crest stained with Fast green and at 2,5X of magnification.*

The cortical bone is composed by a mineralized extracellular matrix and lamellae arranged in concentric layers to form a structural unit called osteon. The osteon is composed of four/twenty lamellae that form circular orbits around channels, i.e. Haversian canals, containing blood

vessels and nerve fibers. Biological communication in these channels is ensured by another group of channels arranged transversely: the Wolkmann canals, also vascularized. Inside the lamellae system, the osteocytes (i.e. bone cells) are placed inside gaps called lacunae and, thanks to the extensive network of canals and capillaries, are able to receive nutritional and perform metabolic exchange [20].

The trabecular bone tissue is structured differently from the compact cortical bone. Haversian canals are rare, often absent, however the communication with the medullary cavity is permitted by cytoplasmic processes. The trabeculae are arranged along the force lines and are responsible for the bone resistance to mechanical stress. The osteocytes are distributed unevenly and with variable quantities.

The cortical bone is mainly present in the diaphysis and in the outer cover of bone, while the trabecular bone is observable in the short bones and in the epiphysis of long bones.

The bone is also coated with a layer of connective tissue with osteogenic potential called periosteum, which is rich in osteoblasts and osteo-progenitors responsible of bone production. The endosteum is instead a further layer of connective tissue thinner of the periosteum, also composed of progenitor cells, which delimits the medullary cavity, containing bone marrow, within the diaphysis.

3.1.2 Bone cellular components

The cellular components of bone tissue are the osteoprogenitor cells, the osteoblasts, the osteoclasts and the osteocytes (Figure 3.2) [21].

The osteoprogenitor cells are undifferentiated mesenchymal cells able to evolve in osteogenic way during the bone growth phase. Osteoblasts are involved in the production of the osteoid tissue, the first step of bone formation. Osteoclasts are multinucleated large cells responsible for bone resorption. Their morphology changes based upon functional undergoing, passing from the resting to the active phase. Osteocytes,

located in the bone lacunae are able to fulfill the metabolic exchanges that would otherwise be limited by the mineral component of the matrix.

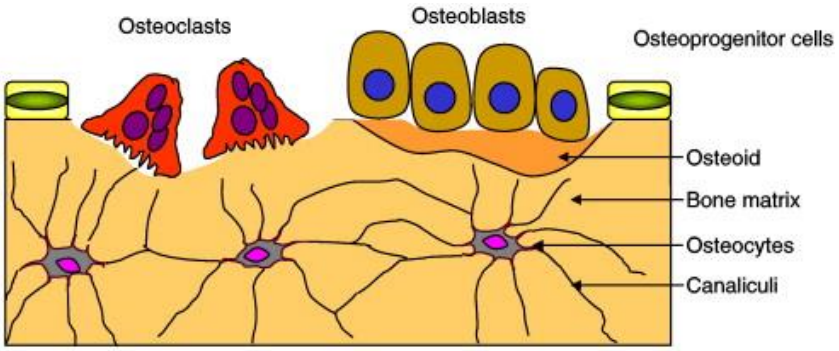

Figure 3.2 *– Schematic diagram of bone structure at cellular level. Reprinted from Advanced Drug Delivery Reviews, Volume 61, Issue 12, 5 October 2009, Jang JH, Castano O, Kim HW, Electrospun materials as potential platforms for bone tissue engineering, Figure 1 Page No.1066, with permission from Elsevier, Licence number 3558260313279.*

3.1.3 Bone matrix

In addition to the cellular component, the bone tissue is composed by an average of about 2/3 of inorganic substances and 1/3 of organic substances.

The main constituents of the organic phase are collagen and non-collagenous proteins, which regulate the interactions between cells and matrix. The collagen, that is the nearly 90% of the organic phase, is able to provide support and resistance to mechanical stress. The main constituent of the inorganic matrix of bone is a mixture of hydroxyapatite (HA) and tricalcium phosphate (TCP) [22].

3.1.4 Bone formation and remodeling

The bone formation process can follow a mechanism of direct and intramembranous ossification, in which the bone is generated from

mesenchymal tissue, or a mechanism of indirect ossification, in which hyaline cartilage differentiate into bone [22].

During the direct ossification, in which bone is created from connective tissue, mesenchymal cells differentiate into osteoblasts specialized in deposit osteoid that will later mineralized in order to form first a primitive non-lamellar bone which will be then replaced by lamellar tissue.

During the indirect ossification a pre-existing cartilage structure is formed which will then be replaced by bone tissue. This kind of bone formation is typical of most of the skeletal bones.

In addition to the processes of ossification, the bone is constantly modified by the activities of modeling and remodeling in order to respond to the different functional needs [23]. This bone turnover is ongoing through a mechanism of resorption, due to osteoclasts activity, followed by a mechanism of bone replacement, due to osteoblast activity. Cells can be stimulated by a variety of signals, for example, they are activated by micro-damages that occur in bones everyday due to mechanical stress.

However, despite the ability to reshape and regenerate the bone after a fracture, the bone remains subjected to degenerative diseases. For example in case of osteoarthritis or in the case of injuries caused by trauma which cannot heal spontaneously and require mechanical osteosynthesis. For these reasons, the need of reconstructive surgery that is based on the use of biomaterials is growing.

3.2 Biomaterials

By definition, a biomaterial is a "substance systematically and pharmacologically inert" [24] that is designed to be implanted in living tissue and to be incorporated with them. In the context of reconstructive surgery, biomaterials have the function of replacing tissues and organs that have been damaged by pathological or traumatic events and that are no longer active and functional. The use and applications of these

materials are increased considerably in recent years and the progress in treatments have allowed the functional recovery of injured organs to a very high number of patients. In fact, currently biomaterials are used to create devices and biomedical implants that are designed specifically to perform certain functions, such as for example:

- orthopedic devices (such as knee, hip, shoulder, ankle prosthesis, osteosynthesis systems such as screws, nails, plates or external fixators);
- implants for soft tissue (such as collagen or hyaluronic acid injection);
- dental implants (such as teeth, roots, bone tissue replacement);
- implantable devices for the controlled release of drugs.

However, the main features that biomaterials must fulfill are the biocompatibility, the biofunctionality and the bioactivity. In case of bone tissue, several biomaterials can be used depending on the disease to be addressed. They can be made by polymers, ceramics, metals, composites or be biologically derived.

Polymeric biomaterials are used principally because of their biodegradability. During the last years, absorbable polyesters have had an extensive significate in regenerative medicine and bone tissue engineering. For example, polycaprolactone (PCL) is subjected to hydrolytic degradation of its ester linkages in physiological conditions. These materials are used principally as scaffold for tissue engineering, i.e. as supports for cells and/or growth factors in order to induce bone regeneration [25]. Hydrogels are also polymeric biomaterials used principally for the release of biological agents or drugs [16].

Ceramic biomaterials can be used either as coatings (for example for metallic prosthesis), as the only components of bone substitutes (for example HA or TCP) or as prosthesis components, such as aluminum oxide (Al_2O_3, alumina) or zirconium dioxide (ZrO_2, zirconia). The latters are inert bioceramics with corrosion and wear resistance, and thus utilized as load-bearing bone replacements.

Metals are used principally because their mechanical properties (Figure 3.3). Their biocompatibility is ensured in most cases on a passive oxide layer that is present on the metallic surface. Currently, the titanium

Figure 3.3 *– Radiograph of a metallic support in the treatment of pseudoarthrosis in an experimental sheep model.*

alloy Ti6Al4V is the most used and a particularly advantageous material for implants due to its low elasticity modulus, a good resistance to fatigue, tension and compression. It has also an excellent biocompatibility and it is virtually bioinert [26].

Composites are combined biomaterials in order to obtain innovative and advanced characteristics [27]. In fact, the properties of each single component are different from the ones of their combination both at structural and chemical-physical level. They are usually divided and classified depending on their structure: fibrous laminar or particulate. Typical examples of composites are the fiber-reinforced polymer.

Biologically derived biomaterials are natural polymers generally more subjected to enzymatic degradation in physiological conditions. Besides, the degradation products are usually easily eliminated or incorporated in the metabolic process. These materials are the polypeptides, the polysaccharides and the bacterial polyesters.

3.2.1 Biocompatibility

One of the most important factors to be assessed for the implantation of a biomaterial is its biocompatibility with the host organism. No significant adverse effects are essential for an effective outcome. Biocompatibility can be divided in three main categories: mechanical, chemical and biological [28].

Mechanical biocompatibility is the geometric and mechanical characteristics of the system in order to function and resist to any stress without deforming. For this purpose, the mechanical properties of the biomaterial should not be too different from that of the host tissue. For example, there are porous materials, such as ceramics, which are more fragile and therefore more exposed to the risk of cracks. The geometrical and mechanical characteristics, together with the resistance to impact, should be analyzed as well as for ceramic, metallic and composite implants.

Chemical biocompatibility regards the chemical phenomena resulting from the presence of the implant in the physiological environment. The most frequent event is the corrosion, which depends mainly on the type of material that is used. The consequences is a reduction in the size and a loss of mechanical capacity of the implant as well as a dispersion of debris inside the host organism. However, in some cases, the remodeling of the implanted biomaterial is exploited, e.g. when it is necessary a bioabsorbable material. For example in the regeneration of a bone defect, the implanted biomaterial is gradually replaced by bone tissue regenerated until its complete replacement.

The biological biocompatibility is the absence of immunological responses and rejection by the host organism. In fact, a "foreign body reaction" can occur, with an acute inflammatory reaction. This condition can develop into a chronic inflammation with the formation of a fibrous capsule that isolate the biomaterial (Figure 3.4).

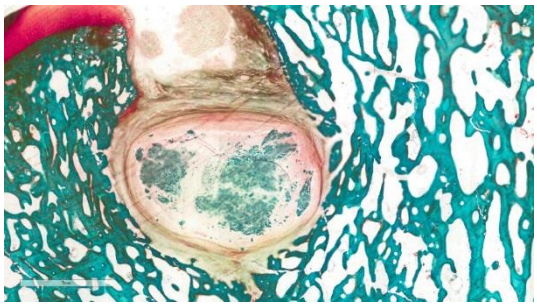

Figure 3.4 *– Histological section of a biomaterials implanted in the femoral condyle of a sheep surrounded by a fibrous capsule. Stained with Safranin-O for articular cartilage matrix proteoglycan assessment and Fast Green for bone. Magnification 1X.*

3.2.2 Other factors controlling bone implant outcome

The optimal implant outcome depends by biomaterial factors (such as design, surface properties, structure, etc.), biomechanical factors, surgical factors and patient factors (such as bone quality, pathologies etc.) [29].

Based on the characteristics of the biomaterial, the effects produces in the implant site are divided into the following properties: osteo-induction, osteo-conduction, osteophilic response and osteo-stimolation.

The osteo-induction is the ability to stimulate bone formation in a host tissue where normally there is no bone (i.e. soft tissue).

The osteo-conduction is the ability to stimulate osteogenesis when the biomaterial is in direct contact with the bone tissue [30].

The osteophilic response is related to the affinity between the surface of the biomaterial and the osteoblasts and is the ability of the material to induce bone growth along its surface.

The osteo-stimolation occurs when a material possesses both osteoinductive and osteophilic properties and stimulates the production of bone tissue either directly or through the release of growth factors.

Another important process during healing at the implant site is the osteointegration. Osteointegration is defined as the lasting and solid anchorage of an implant achieved by the direct contact between living bone and biomaterial [31]. The basic requirement to establish real and lasting integration tissue by a biomaterial is based on the understanding of the response of the hard and soft tissues at peri-implant site [32].

Chapter 3. Biomaterials for orthopedics

PART II
MICRO-CT APPLICATIONS IN ORTHOPEDICS

Chapter 4
Micro-CT evaluation of biomaterials

Translating experimental biomaterials into products with clinical applications involves multiple challenges. Key issues include manufacturing, biomechanical and structure assessment, preclinical *in-vitro* and *in-vivo* assessment. In orthopaedic preclinical research, the study of the interactions between bone and biomaterials is assessed through different levels of analysis: general macroscopic evaluations, biomechanical evaluations, histological, histomorphometric analysis Micro-CT.

In the recent years, micro-CT has increasingly become a necessary technique due to its non-destructive nature. Currently one of the most incisive needs in the industry and in research is the development of non-destructive methods to analyse the microstructure of various types of material. Furthermore, the only 2D analysis, provided for example by histology, is totally inadequate in the case of samples which are too fragile to be cut (for example powders) or in the case of connectivity or tortuosity quantification of different material phases. The images dataset produced by a microtomographic system generally constitutes the entire volume of the analyzed sample and create a large amount of 3D morphological information both of the external and internal features. The intrinsic ability to provide a huge amount of data and a complete volumetric visualization allow the evaluation of biomaterials in two different ways:

by studying the 3D structure or by studying the regenerated tissue morphology and thus their efficacy in case of implantation. In addition, 3D models (Figure 4.1) could be used to create movies of the analyzed object in motion, or they could be used as a basis for the creation of prototypes (e.g. STL or PLY files, useful in the additive manufacturing technique) or for the creation of 3D meshes useful in the finite element (FE) analysis.

Given the non-destructive nature of the technique, another important aspect is the possibility to follow the evolution of a microstructure under controlled environmental conditions (e.g. load, temperature and/or corrosive environment). This aspect is sometimes called 4D imaging (3D + time). In this case, the quantitative analysis can then be extended to the definition of dynamic parameters such as flow, damage accumulation, degradation and the possibility of mapping the induced deformations or displacements. The 4D imaging can also be used to validate numerical predictions of structural and microstructural evolution (mathematical modeling).

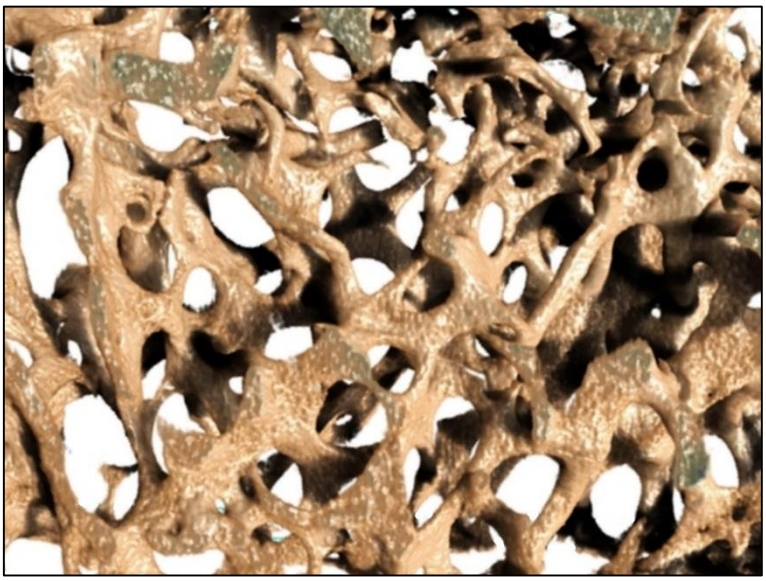

Figure 4.1 *– 3D model of trabecular bone.*

4.1 Image analysis

The extraction of quantitative parameters of 3D images requires proper image processing, segmentation and analysis.

Image processing is generally applied in order to "improve" the image and it mainly involves the modification of gray levels (equalization, normalization of brightness and contrast, etc.) and filtration (to remove noise or to subtract the background).

Segmentation is the process in which a gray scale is continuously divided into discrete groups, usually based solely on their gray levels that depend on the local attenuation of X-ray due to the scanned object. The aim is to define which regions of the image belong to different phases present in the material. Finding an adequate segmentation threshold is fundamental because all dimensional measurements using micro-CT are based on counting voxels (i.e. volumetric pixel) inside a determined boundary. There are several types of algorithms to segment an image (Figure 4.2); the most used are based on the histogram of gray level. The histogram plots the number of pixels for each gray level, e.g. for an 8 bit image the number of pixels for each of the 256 gray levels.

After the image segmentation of the micro-CT sections, it is possible to extrapolate the morphometric parameters according to the individual 3D discrete objects detected.

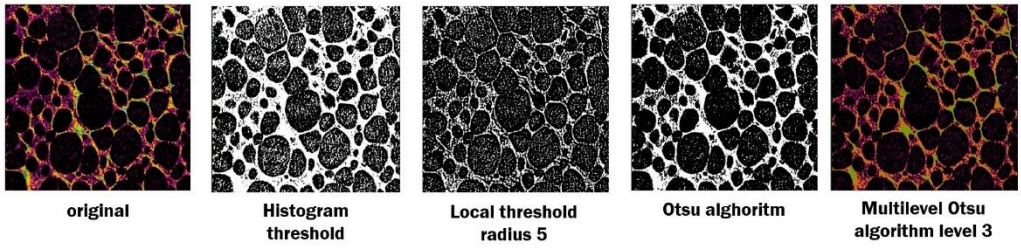

Figure 4.2 *– Some different thresholding (segmentation) methods applied to the original image of a porous collagen-derived biomaterial.*

The size and the shape of the sample to analyze in addition to affect the scanning time and the resolution of images, affect the resulting feasibility of processing for a 3D analysis. Depending on the result and the parameters, which will be obtained from this type of analysis, different strategies for sample acquisition and the related image processing should be adopted.

The morphological image analysis can be performed both in 2D, carried out sequentially at each individual image of the microtomographic dataset, or directly in 3D by means of special algorithms. In this way the quantification of geometries or significant parameters. For example, the manufacturing steps of a medical device, the microstructural characteristics in complex morphologies, such as cracks due to corrosion or wear, measurements on the porosity, its interconnectivity and the tortuosity of a biomaterial (useful for the mathematical model of the transport properties, such as permeability) can be evaluated.

Defining a reference volume is necessary for many morphometric standard parameters. This reference volume, often called Volume of Interest (VOI), can be delineated either automatically using software routines or manually.

Some of the most used morphological parameters calculated using image analysis software are described in Tables 4.1 and 4.2. Important morphometric parameters derived from micro-CT analysis are derived from histomorphometry. In fact, for bone measurements, the ASBMR (American society for bone and mineral research) system is adopted [33].

Parameter	Symbol	Unit
VOI volume	TV	mm^3
Object volume	Obj.V	mm^3
Percent object volume	Obj.V/TV	%
Object surface	Obj.S	mm^2
Object surface/volume ratio	Obj.S/Obj.V	mm^{-1}
Object surface density	Obj.S/TV	mm^{-1}
Fragmentation Index	Fr.I	mm^{-1}
Structure model Index	SMI	
Structure thickness	St.Th	mm
Structure number	St.N	mm^{-1}
Structure separation	St.Sp	mm
Degree of anisotropy	DA	
Fractal dimension	FD	
Number of objects	Obj.N	
Closed porosity	Po(cl)	%
Open porosity	Po(op)	%
Total porosity	Po(tot)	%

Table 4.1 *– 3D most used morphological parameter for a micro-CT analysis.*

Parameter	Symbol	Unit
Mean total section object area	Obj.Ar	mm^2
Mean number of object per slice	Obj.N	
Average object equivalent circle diameter per slice	Av.Obj.ECD	mm
Mean polar moment of inertia	MMI (polar)	mm^4
Mean eccentricity	Ecc	
Structure thickness (plate model)	St.Th(pl)	mm
Structure separation (plate model)	St.Sp(pl)	mm

Table 4.2 *– Some other 2D parameters frequently used for a micro-CT analysis in addition to those of the 3D analysis.*

4.2 Densitometric analysis

In addition to the evaluation over time of morphological 3D parameters, it is possible to evaluate the mineral content and its variations due to the principle that the gray levels of every micro-CT section give a map of the distribution of the absorption coefficients of the X-rays related to the analyzed sample. Such coefficients depend on the material density, from the atomic number of the elements that constitute it and from the incidental energy used. This kind of analysis can be performed when the object to be tested is composed principally by a specific material that is the main responsible for the X-ray absorption. In the bone tissue densitometric analysis gives information on the mineral content, and thus on the healing process, for example, at the peri-implant site. Moreover, mineralization is an important aspect in several bone disease evolution such as, for example, osteoporosis or osteoarthritis. The X-ray attenuation within the mineralized tissues such as bone can be approximated as the X-ray attenuation of hydroxyapatite. Using phantoms with bone equivalent material and a known density allows the calibration of the gray level contrast of the images.

In orthopedic preclinical studies, usually two different densitometric parameters are evaluated: Bone Mineral Density (BMD) and Tissue Mineral Density (TMD) [34]. The main differences is that TMD is calculated from only the volume of calcified tissue excluding the surrounding soft tissue or “non-bone” voxels. Typically, trabecular bone is assessed for BMD, while cortical bone is assessed for TMD.

4.3 3D Models

The most important computer algorithms for 3D visualization and modelling are: maximum intensity projection (MIP), shaded surface display (SSD) and volume rendering (VR) (Figure 4.3).

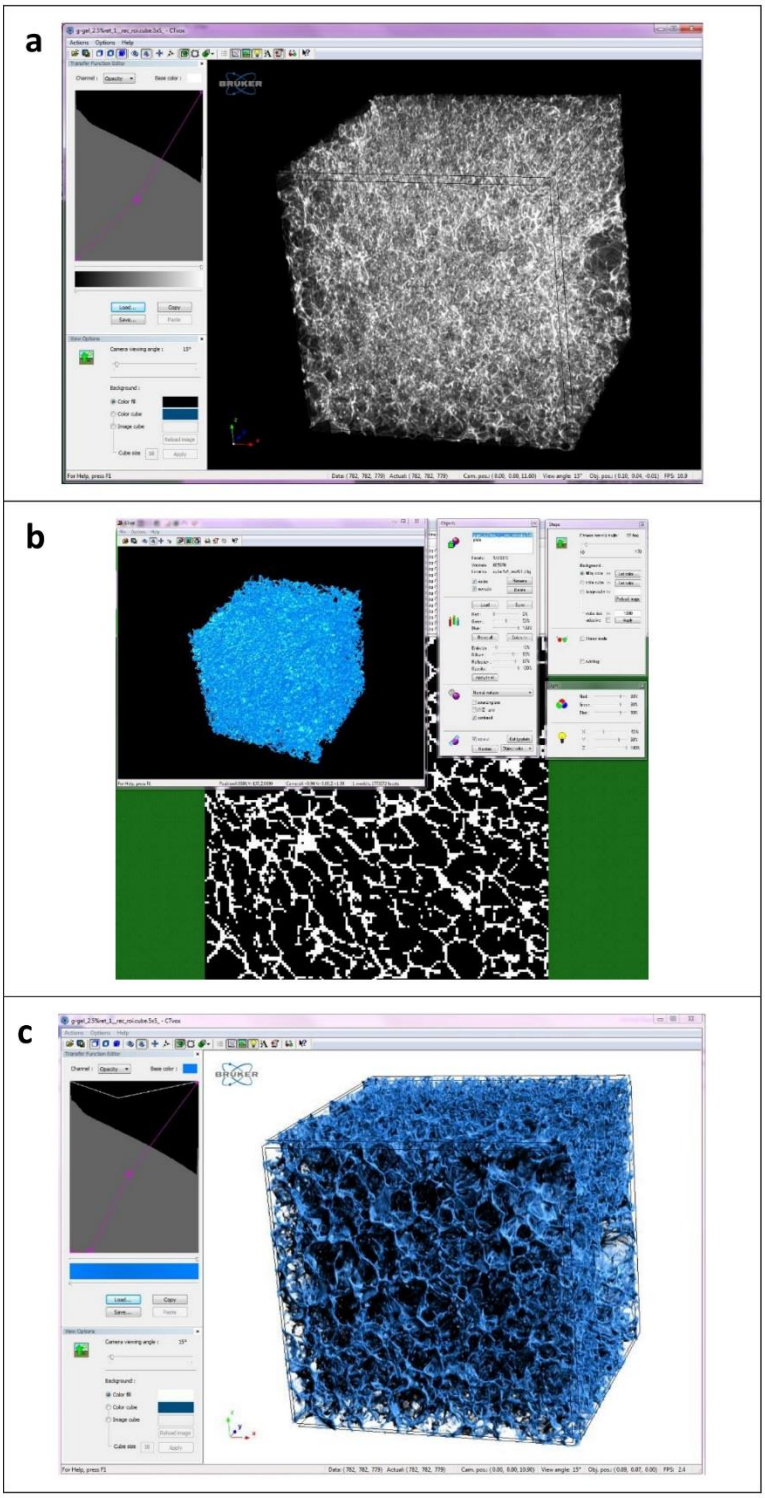

Figure 4.3 *– 3D models of a gelatin scaffold obtained with different visualization techniques: a) MIP; b) SSD and c) VR.*

MIP is a rendering technique that selects the maximum intensity voxel value along the *z*-axis for each xy coordinate. This maximum intensity is displayed and it constitutes the 3D rendering image. This technique allows the identification of denser structure in the entire volume analyzed.

SSD is sometimes called feature extraction or iso-surfacing. The micro-CT dataset that constitute the analyzed object is first segmented, and then the resulting surfaces are displayed as a number of polygons.

VR is a modelling process that calculates the contribution of each voxel in the entire micro-CT dataset. The resulting data are displayed as a RGBA (red, green, blue and alpha) volume.

PART III
EXPERIMENTAL RESEARCH STUDIES

Chapter 5
Experimental design

The PhD research consisted in three main topics: 1) microtomographic studies on different kinds of biomaterials before the implantation or tested in-vitro, 2) ex-vivo microtomographic studies on biomaterial application in orthopedic preclinical research and 3) in-vivo microtomographic studies on biomaterial application in orthopedic preclinical research.

The first year of the research was dedicated to the micro-CT analysis of different kinds of biomaterials in the pre-implantation phase studying new procedures in order to widen the acquisition setting possibilities and the kinds of quantitative analytical methods. During the first year, the project followed three different research lines using advanced micro-CT techniques:

a) the study of thixotropic carboxymethylcellulose (CMC) hydrogels added with iron magnetic-nanoparticles (CMC-NPs) examining the differences in magnetic particle distribution and using a micro-CT freezing chamber to overcome the limitation of movements during the acquisition;

b) the study of the 3D cell distribution seeded onto a polymeric scaffold using OsO_4 as contrast agent and developing a new micro-CT segmentation protocol;

c) the study in the field of dimensional metrology establishing an approach for the quantification of wear in ZrO_2 head prosthesis

components using micro-CT and to validate the method comparing it with gold standard gravimetric analysis.

The second year of the research was dedicated to the applications of biomaterials in orthopedic research through *ex vivo* micro-CT analysis. In particular it was studied the interaction between X-ray and different kinds of biomaterials implanted in bone tissue, and the strategies to apply in order to obtain quantitative morphologic parameters. The main objective was to identify the mechanisms of material resorption and degradation in physiological environment and the mechanisms of bone remodelling. During the second year, the project followed three different research lines using advanced micro-CT techniques:

a) the evaluation of the *in vivo* behaviour of a ceramic custom made prosthesis in a suitable animal model (adult sheep) at 6 and 12 months from surgical cranioplasty;

b) the evaluation of the characteristics of bone quality and its microarchitecture in retrieved metal-on-metal hip resurfacing arthroplasties (HR);

c) the analysis of granules characteristics using a new injectable multiphasic bone substitute based on gel-coated OsproLife® HA/TTCP.

The third year of the research was dedicated on improving the knowledge in microtomographic techniques for orthopedic research following two main topics: the *in vivo* analysis and the densitometric analysis. In particular, the interaction between X-ray and tissues and the strategies to apply in order to obtain in-vivo micro-CT images without movement artefacts and using low doses of X-rays was studied. Besides, the analysis of bone quality from a densitometric point of view, through the calibration by means of phantoms with known BMD, was explored.

Thus, during the third year, the project was divided in the following research lines using advanced micro-CT techniques:

a) the evaluation of the in vivo osteoinductive behaviour of three-dimensional interconnected porous scaffolds of gelatin with or without contents of nanocrystalline hydroxyapatite (HA) over time;

b) the evaluation of bone quality in terms of mineral content in a study of osteoarthritis treatment in a large animal model with engineered hyaluronic acid scaffolds.

All the analysis were performed at the Preclinical and Surgical Studies laboratory and at the BITTA (Biocompatibility, Technological Innovations and Advanced Therapies) laboratory of Rizzoli Orthopaedic Institute. The laboratories are equipped with two different micro-CT systems: Skyscan 1172 and *in vivo* Skyscan 1176 by Bruker Micro-CT (Belgium).

Chapter 6
Micro-CT analysis of thixotropic carboxymethylcellulose (CMC) hydrogels

6.1 Introduction

Recently polysaccharide-based hydrogels have becoming increasingly studied due to their properties and to their biocompatibility [35-36]. Characteristics such as softness, the possibility of incorporating drugs in a smart way, and the ability to store water constitute the attractiveness of material scientists towards the hydrogels [37]. One of the most interesting smart applications regards the possibility of the controlled release of drugs. An innovative strategy is found in the use of magnetic nanoparticles (NP) for targeted drug delivery, which consists in guiding the NP towards the target using external magnetic fields [38]. CMC hydrogels added with iron magnetic NP behave in a thixotropic way when they are syringe extruded. Information about the NP distribution inside the hydrogels before and after the syringe extrusion can be extrapolated from a micro-CT analysis. However, Micro-CT needs that the analyzed object is completely still during the acquisition. When the hydrogels are syringe extruded they become liquid and the nanoparticles

move with the hydrogel during the scanning procedure. To overcome the limitation due to movements, a micro-CT freezing chamber (Bruker micro-CT, Belgium) was used. The chamber contains all necessary parts to cool down the sample and measure and stabilize the sample stage temperature.

6.2 Materials and Methods

The hydrogels, both before and after syringe extrusion, were cooled until -10 °C in the freezing chamber. After the reconstruction in tomographic images, for each sample, three cylindrical VOIs with a diameter of 1 mm and a high of 1 mm were considered. The VOIs were placed randomly in different zones of the hydrogels volume. The metallic nanoparticles inside the VOIs were then segmented in order to calculate their number and their volume.

6.3 Results and Discussion

The results of the volume and the number of NP are summarized in Table 6.1 and Table 6.2.

The results showed no difference in distribution of clusters of NP between the material before and after syringe extrusion. Both distribution and number seem to be more dependent on the sample or on the VOIs position analyzed than on extrusion (Figure 6.1).

CMC-NPs		3D Analysis (%)			
		VOI 1	VOI 2	VOI 3	Average ± SD
Before syringe extrusion	sample 1	0.61	0.19	0.07	0.29 ± 0.28
	sample 2	0.10	0.05	0.09	0.08 ± 0.02
	sample 3	0.09	0.05	0.33	0.15 ± 0.15
After syringe extrusion	sample 1	0.48	0.13	0.24	0.28 ± 0.18
	sample 2	0.21	0.05	0.27	0.17 ± 0.11
	sample 3	0.08	0.05	0.07	0.07 ± 0.01

Table 6.1 *–Percentage of the NPs volume detected in the total volume of each VOI.*

CMC-NPs		3D Analysis (number)			
		VOI 1	VOI 2	VOI 3	Average ± SD
Before syringe extrusion	sample 1	4312	2442	2374	3043 ± 1100
	sample 2	2261	1711	1845	1939 ± 287
	sample 3	526	247	639	471 ± 202
After syringe extrusion	sample 1	7072	8575	5872	7173 ± 1354
	sample 2	2994	2662	3387	3014 ± 363
	sample 3	1047	1033	1249	1110 ± 121

Table 6.2 *– Number of 3D NPs detected in all the three VOIs.*

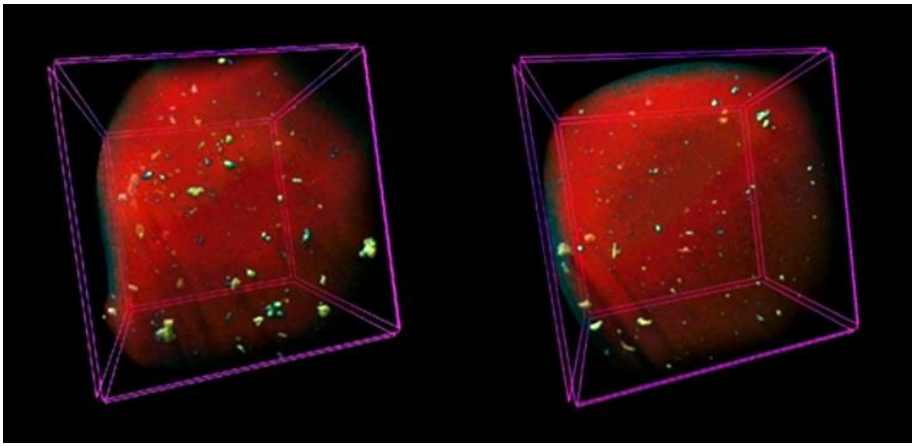

Figure 6.1 *–3D models of CMC-NPs hydrogels before (left) and after (right) syringe extrusion. In yellow are highlighted the magnetic NPs clusters.*

Chapter 7
3D cellular distribution in polymeric scaffolds for bone regeneration: a microCT analysis compared to SEM, CLSM and DNA content [39]

Reprinted with permission from John Wiley and Sons, Licence Number 3556531150197

Annapaola Parrilli[1], Stefania Pagani[1,2], Maria Cristina Maltarello[3,4], Spartaco Santi[3,5], Aurelio Salerno[6,7], Paolo Antonio Netti[6,8], Roberto Giardino[1], Lia Rimondini[9], Milena Fini[1,2]

[1] Biocompatibility, Technological Innovations and Advanced Therapies Laboratory (BITTA), Rizzoli RIT Department, Rizzoli Orthopaedic Institute, Via di Barbiano 1/10, 40136,Bologna, Italy

[2] Laboratory of Preclinical and Surgical Studies, Rizzoli Orthopaedic Institute, Via di Barbiano 1/10, 40136, Bologna, Italy

[3] Laboratory of Muscoskeletal Cell Biology, Rizzoli Orthopaedic Institute, Via di Barbiano 1/10, 40136, Bologna, Italy

[4] RAMSES Laboratory, Rizzoli RIT Department, Rizzoli Orthopaedic Institute, Via di Barbiano 1/10, 40136, Bologna, Italy

[5] CNR, Institute of Molecular Genetics, Via di Barbiano 1/10, 40136, Bologna, Italy

[6] Interdisciplinary Research Centre of biomaterials, University of Naples Federico II, Piazz.le tecchio 80, 80125, Naples, Italy

[7] Institute for Composite and Biomedical Materials, National Research Council, (IMCB-CNR), Piazz.le tecchio 80, 80125, Naples, Italy

[8] Centre for Advanced Biomaterials for Health Care (CRIB-IIT), Istituto Italiano di Tecnologia, Piazz.le tecchio 80, 80125, Naples, Italy

[9] Department of Health Sciences, University of Piemonte Orientale "Amedeo Avogadro", via Solaroli 17, 28100, Novara, Italy

ABSTRACT

In orthopedic surgery the tissues damaged by injury or disease could be replaced using constructs based on biocompatible materials, cells and growth factors. Scaffold design, porosity and early colonization are key components for the implant success. From biological point of view, attention may be also given to the number, type and size of seeded cells, as well as the seeding technique and cell morphological and volumetric alterations. The present paper describes the use of the microCT approach (to date used principally for mineralized matrix quantification) to observe construct colonization in terms of cell localization, and make a direct comparison of the microtomographic sections with SEM images and CLSM analysis. Briefly, PCL scaffolds were seeded at different cell densities with MG63 osteoblastic-like cells. Two different endpoints, 1 and 2 weeks, were selected for the 3D colonization and proliferation analysis of the cells. By observing all images obtained, in addition to a more extensive distribution of cells on scaffolds surfaces than in the deeper layers, cell volume increased at 2 weeks compared to 1 week after seeding. Combining the cell number quantification by DNA analysis and the single cell volume changes by CLSM, we validated the microCT segmentation method by finding no statistical differences in the evaluation of the cell volume fraction of the scaffold. Furthermore, the morphological results of this study suggest that an effective scaffold colonization requires a precise balance between different factors, such as number, type and size of seeded cells in addition to scaffold porosity.

KEYWORDS: microCT; microtomography; scaffold; 3D cell distribution; tissue engineering

7.1 Introduction

Nowadays the incidence of skeletal lesions is gradually increasing, especially that of injuries and degenerative joint diseases due to lifestyles and longer life expectancy respectively. In orthopedic and in maxillofacial and oral surgery the great need to replace damaged or lacking tissues can be only partially obtained from autologous and allogenic grafts and usually these approaches are associated with several drawbacks [40-41]. In order to overcome these limits, the new challenge might be regenerative medicine, which aims to repair, replace or regenerate tissues and organs damaged by injury or disease by using biocompatible and bioactive materials [42].

Tissue engineering and regenerative medicine are multidisciplinary sciences, resulting from different skills that combine the study of biomaterials, growth factors and cells to repair failing organs [43]. Cells, scaffolds and growth factors are combined in the in vitro phase, which is a crucial moment for the successful outcome of applied tissue engineering. The need to display the architecture of materials and especially the cellular distribution inside the constructs has consequently triggered different technical efforts. The most common method for examining cells in scaffolds is still microscopy. Based on embedding the sample, sectioning and finally histological staining, this technique is destructive and only semi-quantitative. For example, fluorescence microscopy can provide a quantitative evaluation, but only if combined with a confocal equipment. Besides, the analyzed depth is very limited and the interior of opaque materials is still a drawback for a complete imaging [44].

To predict the complete 3D cell colonization of the scaffold (the key request in tissue engineering), there are numerous microtomographic studies focusing on the porosity and pore interconnectivity of the scaffold itself [45-49], but very few concerning 3D cell visualization within the scaffold [44, 50-51]. In microCT slice images, contrast is on a linear grayscale that means the lighter the pixel, the higher the voxel

absorption. Cells do not have the intrinsic X-ray attenuation ability to be clearly visualized by microCT thus it becomes necessary to use a contrast agent [52]. The studies that have approached 3D cellular distribution analysis by microCT used osmium tetroxide as contrast agent [44, 50] because of its great affinity with lipids: it reacts with unsaturated lipids by forming black compounds containing hexavalent osmium that are visible by microCT. Despite the use of contrast agent, we believe that the intensity-based segmentation of polymeric scaffolds seeded with cells is still problematic. Establishing a segmentation protocol is necessary to improve the reliability of the results, overcome the variability and make the analysis repeatable regardless of the operator.

In the present study microCT was used to visualize and quantify the distribution of cells seeded in polycaprolactone (PCL) scaffolds. PCL is often used in regenerative medicine for orthopedics because of its biocompatibility and its ability to resorption, thus leaving space for the new formed bone. The study was designed in two phases: 1) osteoblast-like cells (MG63) were seeded at various concentrations and experimental times into 3D PCL scaffolds, and the surface visualization by scanning electron microscopy (SEM), which is the technique that routinely uses osmium tetroxide as agent, was compared with the surface visualization by microCT; 2) after the establishment of a protocol for image segmentation, the microCT 3D volume fraction quantification of cells within the scaffolds was compared to DNA content quantification in association to Confocal Laser Scanning Microscope (CLSM) analysis.

7.2 Materials and Methods

7.2.1 Fabrication of PCL scaffolds

Porous PCL scaffolds with a bi-modal pore size distribution and characterized by micro-structural properties suitable for bone tissue engineering applications were prepared as described in a previously

reported work [53]. Briefly, PCL was melt-mixed with thermoplastic gelatin (TG) with a 3/2 (w/w) ratio and, subsequently, the PCL/TG blend was gas foamed by using a 4/1 (v/v) N_2/CO_2 blowing mixture and selecting a foaming temperature of 44 °C. The TG was subsequently removed by soaking the foamed samples in dH_2O at 38 °C for 1 week to allow for the formation of the final pore structure of the scaffold.

7.2.2 Scaffold treatment and Cell culture

Before cell seeding, 78 cylindrical PCL scaffolds were divided along the major axis into 2 equal pieces (n= 156), sterilized by soaking in 70% ethanol (overnight), then in 1% antibiotic/PBS solution (2 hours). Finally, the materials were washed with PBS and pre-wetted in complete medium for 1 hour, to permit protein absorption, and promote material hydrophilicity and then cell adhesion onto PCL. A culture of MG63 (osteoblastic-like cell, from human osteosarcoma) was used and maintained in D-MEM medium (SIGMA, St. Louis, MO), containing 10% fetal bovine serum (FBS), 2 mM L-glutamine, 100 units/ml penicillin and 100 μg/ml streptomycin in saturated humidity atmosphere (5% CO_2/95% air), at 37° C. The cells were sub-cultured in flasks, detached by 0.25% trypsin/EDTA, (GIBCO, Invitrogen, NY, USA), counted and seeded onto the scaffolds for different kinds of analysis. The MG63 seeding was performed drop-wise in 20 μl of medium onto ≈ 0.25 cm^2 PCL surface at different cell densities: $1x10^5$cells/cm^2 (100k cells/cm^2), $2x10^5$cells/cm^2 (200k cells/cm^2) and $4x10^5$cells/cm^2 (400k cells/cm^2), repeating carefully the deposition and the recovery of the cells. This procedure should allow cell adhesion to the surface of the materials, infiltration into the porous structure and also prevent cell dispersion. After 1 hour, each scaffold was carefully removed into a new 24-well plate (Costar, NY, USA) and covered with 1 ml of complete medium. Two different endpoints, 1 and 2 weeks, were selected for the analysis of the 3D MG63 colonization and proliferation. Furthermore, PCL without cells was used as negative control, with the

same culture conditions as the seeded constructs and at the same endpoints. The groups, the number of scaffold and the kind of analysis at the two experimental times are reported in Table 7.1.

	Groups	Number of scaffolds
MicroCT/SEM	no cells	6
	100k cells/cm^2	20
	200k cells/cm^2	20
	400k cells/cm^2	20
DNA content	no cells	6
	100k cells/cm^2	20
	200k cells/cm^2	20
	400k cells/cm^2	20
CLSM	no cells	6
	100k cells/cm^2	6
	200k cells/cm^2	6
	400k cells/cm^2	6

Table 7.1 *– Description of experimental design of the study reporting in detail the groups, the scaffold number and the kind of analysis at the two experimental times.*

7.2.3 DNA content

Cell number was obtained by quantification of DNA content. After sample washing with PBS, 100 µl of lysis solution (0.01% Triton in TE buffer) were added to each construct and cell lysis was then completed

by three freeze-thaw cycles. DNA content was calculated from the lysates by addition of 100 µl of fluorescent nucleic acid stain to each sample (Quant-iT PicoGreen dsDNA Assay Kit, Invitrogen, Oregon, USA), after 5 min of incubation at room temperature and protected from light, according to manufacturer's instructions. The fluorescence was measured at 490ex-520em wavenlenghts (Spectra Max Gemini plate fluorometer - Molecular Devices, Sunnyvale, CA), and readings were expressed as relative fluorescence units (RFU). Referring to the DNA standard curve set with Pico Green kit reagents, first it has been calculated the DNA content of each sample. Secondly, cell number has been obtained as ratio between these values and the mean cellular DNA amount, suitably evaluated by NANODROP spectrophotometer onto MG63 at known density. MG63 plated at serial known densities and specifically evaluated as DNA content proved the fairness of this evaluation. The 3D cell volume fraction was obtained as the ratio between the cell number multiplied by the volume of a single cell and then divided by the total volume of the scaffold.

7.2.4 Confocal Laser Scanning Microscope (CLSM)

Phalloidin staining for detecting the cytoskeleton filamentous actin (F-actin) of the MG63 cell line seeded in PCL scaffolds was conducted according to the manufacturer's protocol (Sigma). In brief, the PCL scaffold/cells were fixed with 4% paraformaldehyde for 15 minutes at 4° C, rinsed twice 10 min with 1X PBS, permeabilized with 0.5% Triton-X100 in PBS for 30 min at room temperature, rinsed twice 20 min with 1X PBS, then incubated with Phalloidin (100 µg/ml, conjugated with FITC), in the dark for 40 min at room temperature rocking, and rinsed 4-5 times 10 min with 1X PBS. Afterwards, the cell nuclei were counterstained with 4′,6-diamino-2-phenylindole (DAPI, Sigma) in the dark for 5 minutes. The specimens were then mounted in 80% Glycerol, 2% DABCO (Sigma) diluted in PBS and then imaged.

Confocal imaging was performed on a Nikon A1R spectral confocal laser scanning microscope equipped with Plan Apo VC 20x (0.75 N.A.) lens. The samples were sequentially excited with 405 and 488 nm for DAPI and Phalloidin-FITC detection. The structure of the PCL scaffolds was investigated by means of the signal based on auto-fluorescence at 561 nm as revealed by spectral analysis. A z-step of 2.0 µm was used to optically section the samples. Data files were digitized with a scanning mode format of 512 x 512 pixels and 4096 grey levels. To create the maximum intensity projections and 3D images, the original z-stack acquired data was treated using the NIS-Elements software (Nikon) with surface shaded option. No deconvolution was applied to the images. The images of DAPI staining and Phalloidin staining were used to quantify the volume of a single MG63 cell at 1 week and at 2 weeks. An adaptive thresholding was applied for the image analysis i.e. for each voxel, the threshold was calculated as the median of all voxel grayscales within the selected radius of 5. The average ratios between the volume of Phalloidin staining and the total number of cells detected by DAPI staining were considered as the volumes of single MG63 cells at the two different experimental times.

7.2.5 Scanning Electron Microscopy (SEM)

Seeded and control scaffolds were fixed for 2 hours in 2.5 % glutaraldehyde in 0.1 M cacodylate buffer at pH 7.2, at 4° C, followed by post-fixation in 1% OsO_4 in the same buffer, 1 hour at room temperature, rocking; they were dehydrated in graded series of ethanol and in hexamethyldisilazane. After gold-coating, the samples were observed at scanning electron microscope (Stereoscan200, Cambridge). The backscattered electron (BSE) observations were performed at 30 KV.

7.2.6 MicroCT

Seeded and control scaffolds were analyzed by microtomographic system Skyscan 1172 (Bruker MicroCT, Belgium) before gold-coating and the subsequent SEM analysis. Three scaffolds were also analyzed without any staining to evaluate their porosity and interconnectivity. Each specimen was scanned at a source voltage of 30 kV and a source current of 175 μA without filters. The samples were rotated to 180° with a rotation step of 0.4° and a frame averaging of 4. The pixel size was 2.5 μm and the scan duration was nearly one hour. The scanning dataset obtained after the cone beam acquisition consisted of approximately 500 images in 16-bit tiff format (4000 X 2096 pixels). The acquisition images were later reconstructed by the software NRecon (version 1.6.2.0) without corrections except for the specific misalignment for each acquisition and an accurate ring artifact reduction because of the small rotation step and the small pixel size. The image datasets in 8-bit jpg format (approximately 1000 images 4000 X 4000 pixels) were visualized with DataViewer software (version 1.4.3) to identify surface sections and allow the direct comparison with SEM surface images.

The threshold value for image segmentation for quantification and relevant distribution of seeded cells was chosen according to attenuation histograms of the sample X-rays, i.e. scaffolds cultured with MG63 at 1 week and 2 weeks and scaffolds without MG63 at the same experimental times (Figure 7.1a). The attenuation histograms of the samples refer to a cylindrical volume of interest (VOI) with a diameter of 4 mm and a height of 1.5 mm for each sample analyzed and placed within the scaffold. This VOI was placed so that it was included inside the sample and had the first section made of air outside the scaffold itself as its upper limit. The grey level value corresponding to the point where the attenuation graphs calculated in the VOIs are no longer superimposable was chosen as the single global threshold value. The area where the histograms are overlapping is associated with absorption contrasts relevant only to the scaffold (the same in each sample analyzed), whereas

the absorption due to the presence or not of cells detected by cell membrane binding with osmium tetroxide is found in the area where the graphs differ from each other. Therefore, to define the value when the histograms begin to separate a graph was made with standard deviation values and their means (Figure 7.1b). Then the trendline of the curve defined by the values corresponding to 25% and 75% of the maximum value of the standard deviation graph was calculated. The intercept of this trendline rounded down was considered as the threshold value for quantifying cell distribution three-dimensionally within the scaffolds.

For quantitative analysis of the cells the CTAnalyzer (Bruker MicroCT, Belgium) version 1.12.11 software program was used. Images were thus segmented from 139 to 255. The cell volume within the total volume of the scaffold was calculated in 3D and the result was expressed as 3D cell volume fraction in percent.

To calculate scaffold 3D porosity and interconnectivity another cylindrical VOI was produced, which was traced from a circular Region Of Interest (ROI) of 2 mm in diameter copied for 546 cross-sectional slices corresponding to nearly 1.4 mm, which can be considered as the height of the cylinder. The VOI was placed inside each specimen so that it was totally enclosed. A binarization of this VOI was subsequently carried out with a global threshold considering the pores as the object (white colored binarization). The porosity was calculated as the ratio between the total pore volume and the total volume of interest, whereas the interconnectivity was calculated as the largest volume of a single connected 3D object detected compared to the total pores volume.

7.2.7 Statistical Analysis

All the microCT and DNA content measurements were summarized as median values and confidence interval. The volume values obtained with the two methods were compared with Mann-Whitney-Wilcoxon test with $\alpha = 0.05$. All the statistical analysis were carried out using the

Statistical Package for the Social Sciences (SPSS Inc., Chicago, Illinois, USA) software version 15.0 (SPSS Inc.,Chicago, USA).

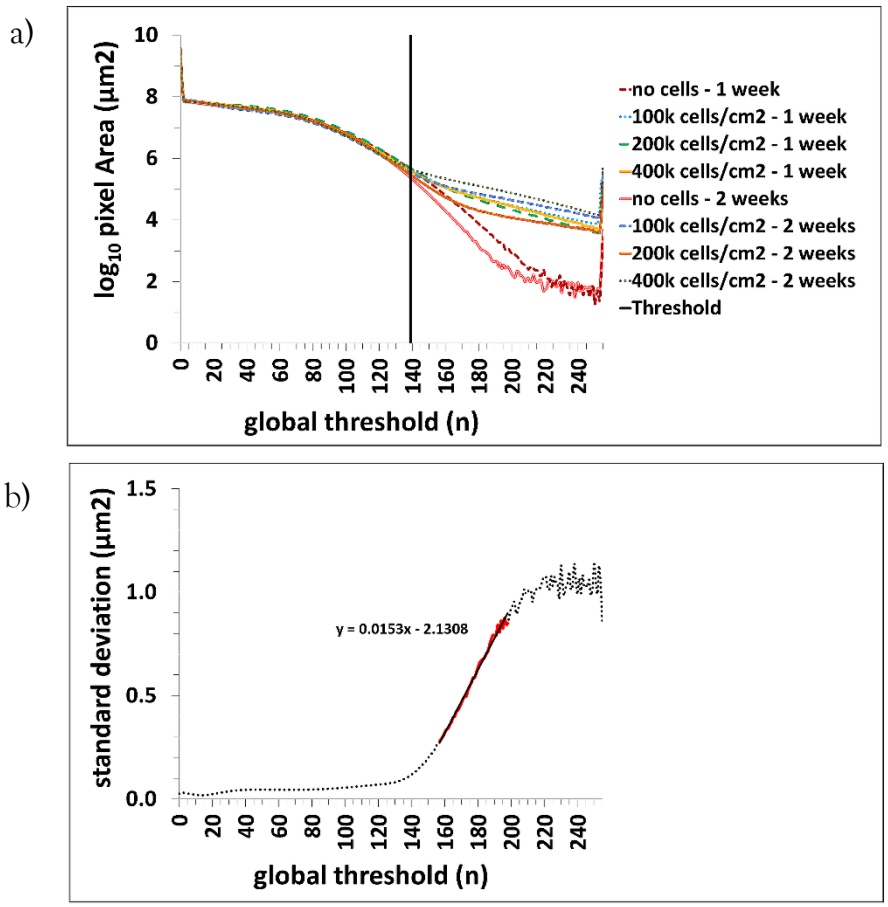

Figure 7.1 *– (a) Attenuation histograms calculated on the VOIs of the preliminary study samples. The black line defines the threshold value considered for quantifying cell distribution within the scaffolds. The grey values relevant only to the scaffold can be seen to the left of this black line, whereas the values relevant to the presence of cells marked by the contrast agent are on the right. (b) Graph of the standard deviations of the means of the attenuation histograms. The portion of the curve corresponding to the values between 25% and 75% of the maximum is highlighted with a grey continuous line. The equation of the trend line of this portion of curve, which was used to calculate the threshold value to apply to the image segmentation to calculate cell distribution within the scaffolds, is also shown.*

7.3 Results

7.3.1 3D Scaffold porosity and interconnectivity

PCL scaffolds showed a fair porosity value (43.04 ± 1.17%) and perfect interconnectivity (99.74 ± 0.12%) to allow cell colonization inside the scaffolds and the contrast agent to pass through them (Figure 7.2a and Figure 7.2b).

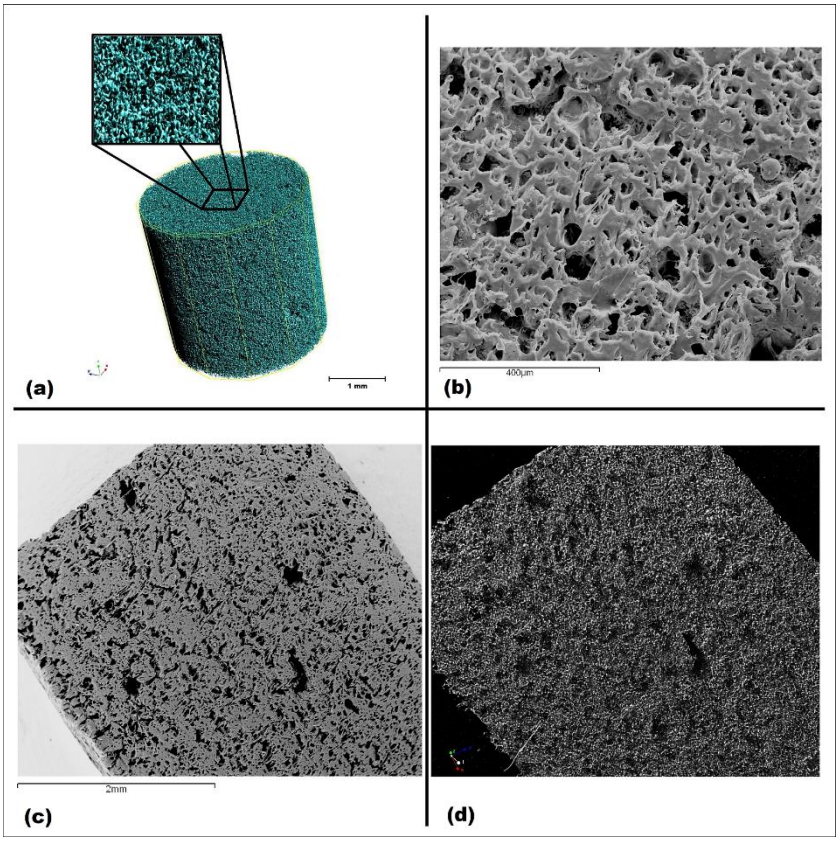

Figure 7.2 *– Control scaffold without cells. (a): The image selected results by a "graphic rendering" and is representative of all the PCL scaffold analyzed. The insert shows an enlarged view of the surface porosity. In (b) the scaffold surface is observed by SEM at high magnification to appreciate the porosity. (c), (d): Surface observations of the same sample before seeding. The SEM (c) and the microCT (d) imagines are compared and show overlapping surface details.*

7.3.2 SEM/MicroCT Visualization

SEM and microCT images of the surface of the scaffold before seeding are reported in Figure 7.2c and Figure 7.2d. SEM images were acquired at a magnification that allows a direct visual comparison with the images of the surface obtained by microCT.

In Figure 7.3 and Figure 7.4 SEM and microCT images of the seeded surface of the cell/scaffold constructs are reported, at one week and at two weeks respectively. As shown, the cells proliferated and almost uniformly colonized the surface of the scaffolds. The cell proliferation is highlighted by a stronger grey level contrast. In fact, the microCT images of the surfaces colonized by cells (Figures 7.3b, 7.3e, 7.3h and Figures 7.4b, 7.4e, 7.4h) were more bright than images of the surfaces before seeding (Figure 7.2d). Moreover, the distribution of the grey level contrasts is well defined and the cells, or the cell clusters, appear as a pointed shape. Differences in cell proliferation were not observed as a function of the starting seeding density.

7.3.3 DNA content and cell number

The cell number evaluation, obtained as the ratio between the total amount of samples DNA and the amount of a single MG63 cell DNA, has revealed similar values in all samples, at both experimental time, independently from the starting seeding density. The range of cell number was 12000 - 13000. The higher number of cells seeded (400k cells/cm^2) showed the lower value after one week but an increasing trend during time.

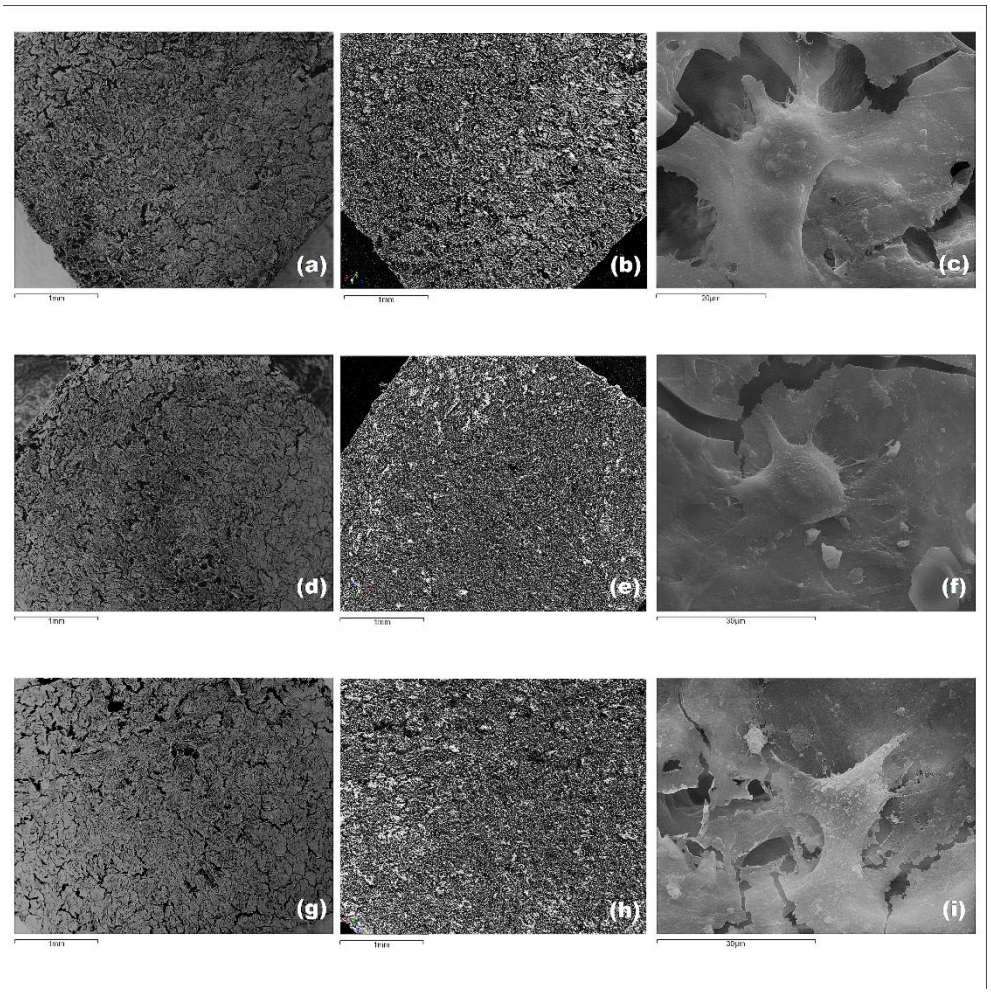

Figure 7.3 *– Images of samples surfaces seeded with MG63 cells at 1 week. SEM image of a PCL scaffold seeded with cell density of 100k cells/cm^2 (a) shows overlapping surface details with microCT image (b) of the same surface. (c): SEM image of a PCL scaffold seeded with cell density of 100k cells/cm^2 at higher magnification shows cell colonization of the surface. SEM (d,f) and microCT (e) images of a PCL scaffold seeded with cell density of 200k cells/cm^2. SEM (g,i) and micro-CT (h) images of a PCL scaffold seeded with cell density of 400k cells/cm^2.*

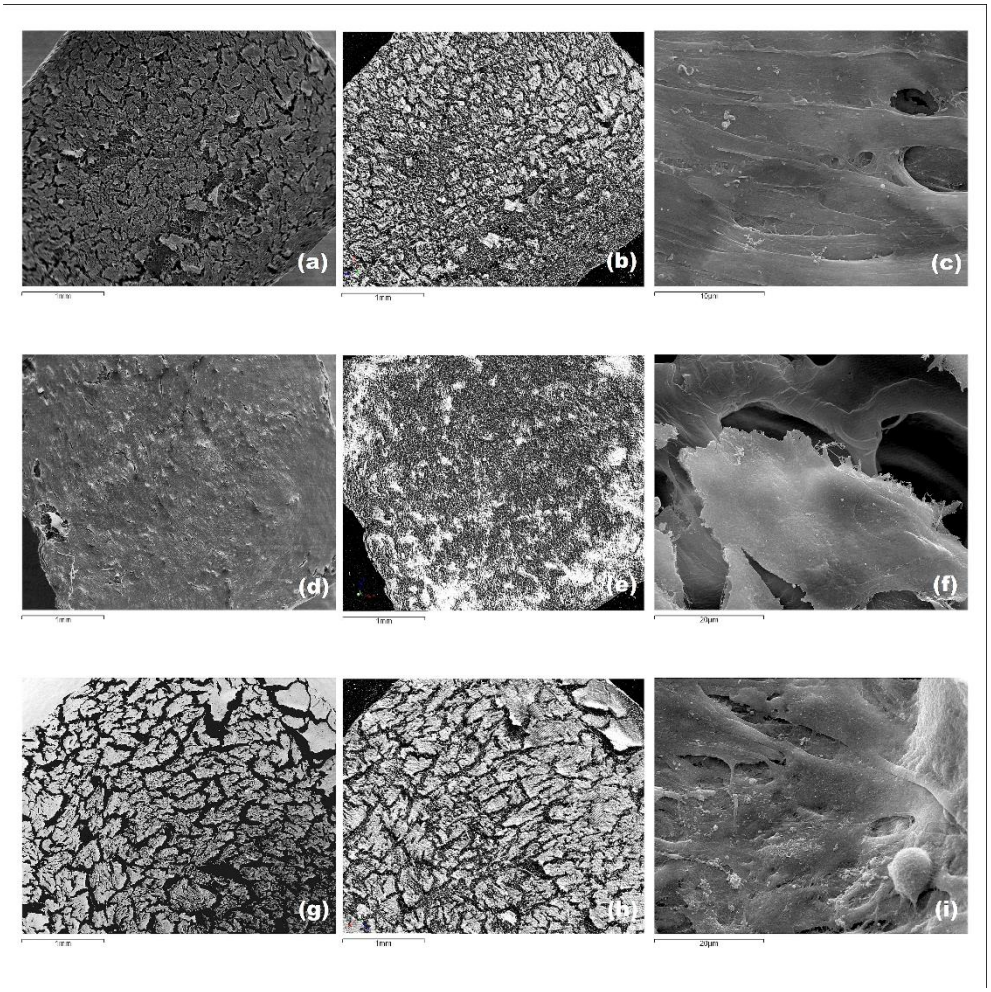

Figure 7.4 *– Images of samples surfaces seeded with MG63 cells at 2 weeks. SEM image of a PCL scaffold seeded with cell density of 100k cells/cm^2 (a) shows overlapping surface details with microCT image (b) of the same surface. (c): SEM image of a PCL scaffold seeded with cell density of 100k cells/cm^2 at higher magnification shows cell colonization of the surface. SEM (d,f) and micro-CT (e) images of a PCL scaffold seeded with cell density of 200k cells/cm^2. SEM (g,i) and microCT (h) images of a PCL scaffold seeded with cell density of 400k cells/cm^2.*

7.3.4 3D Cell Volume Fraction and 3D Cell Distribution

The DNA analysis results of cell volume fraction, expressed as ratio between the volume of cells detected and the total volume of the scaffold, show at 2 weeks a significant increase by 135% for scaffolds seeded with 100k cells/cm^2, 248% for scaffolds seeded with 200k cells/cm^2, and 178% for scaffolds seeded with 400k cells/cm^2 compared to the same results at 1 week. In the same way, the 3D microCT results of cell volume fraction within the scaffold show an increase over time for all concentrations of cells seeded (Figure 7.5). At 2 weeks the cell volume values increased significantly by 163% for scaffolds seeded with 100k cells/cm^2, 340% for scaffolds seeded with 200k cells/cm^2, and 181% for scaffolds seeded with 400k cells/cm^2.

Differences between the two methods of analysis (DNA and microCT) were compared using Mann–Whitney–Wilcoxon test and no statistical differences were founded.

The picture of the 3D models also shows the spatial distribution of scaffold cell colonization (Figure 7.6c) and provides a vision of the cell proliferation trend over time. The increase in cell density within the scaffold is thus detected more at the surfaces (Figure 7.6a and 7.6b) in all seeded scaffolds and evenly spread over time.

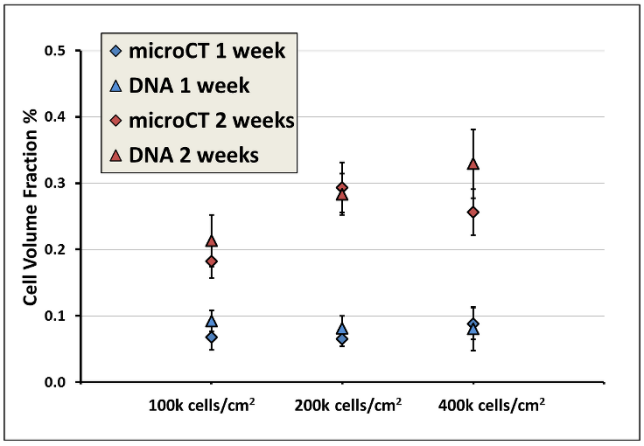

Figure 7.5 *– 3D cell volume fraction (%) medians and confidence intervals of osteosarcoma cell line MG63 seeded in PCL scaffolds at different concentrations and different experimental times calculated by DNA and microCT analysis.*

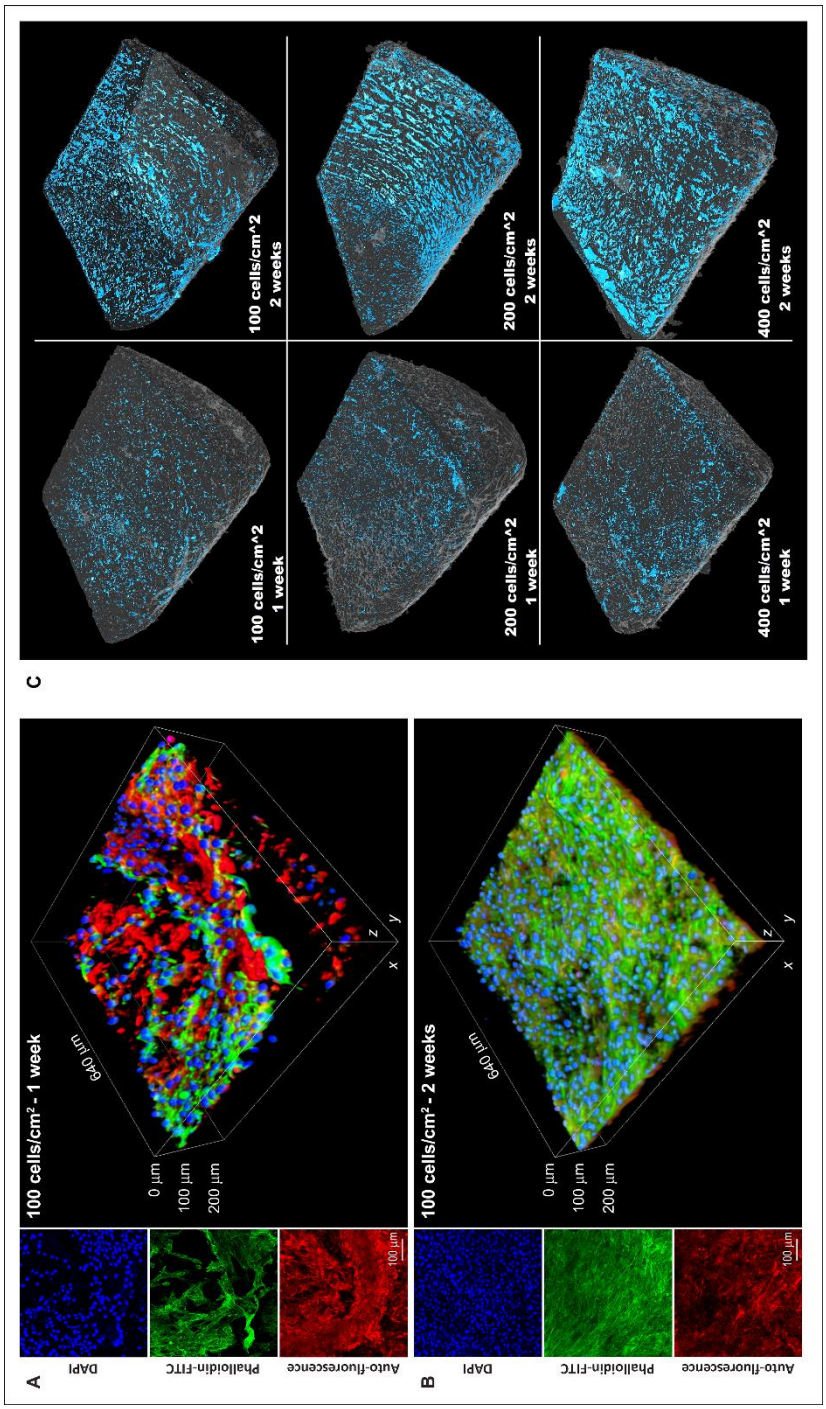

Figure 7.6 *– (A), (B): Confocal imaging of PCL scaffold/cells stained with DAPI (blue) and Phalloidin-FITC (green). The scaffold auto-fluorescence was showed in red. The scaffolds were seeded with 100 cell/cm2 and cultured for (A) 1 week or (B) 2 weeks. On the left side was shown the maximum intensity projections of the single channels, on the right the 3D volume reconstruction of the region of detection. The maximum intensity projections of DAPI/Phalloidin-FITC (blue/green) and scaffold auto-fluorescence (red) was shown to provide a more intuitive view of cellular distribution from the scaffold surfaces to the interior parts. (C): 3D microCT models of PCL scaffolds seeded with different concentrations of MG63 cells at 1 week and 2 weeks after seeding.*

7.4 Discussion

Tissue engineering aims to produce medical devices that will repair, restore or regenerate tissues impaired by disease, injury, or age. The current need to restore or regenerate tissues (in orthopedic, reconstructive and in maxillofacial and oral surgery), cannot be achieved by autografts because of their limited availability and marked associated morbidity rate. Tissue engineering approaches could supply sufficient amounts of bone substitutes by harvesting autologous osteogenic progenitors from alternative sources (bone marrow or fat) associated with suitable porous biomaterials [41].

In the present study, to obtain analytical images of seeded scaffolds commonly used in tissue engineering, back-scattered electrons (BSE) were used that highlighted how the interaction between osmium and an electron beam generates a light imagine of the cells. The same concept was applied to the microCT technique to observe the cell colonization inside the scaffold analytically. The evident overlap of surface images obtained by these alternative ways shows that this new method is a reliable tool for cell visualization. Although currently the most widely used technique to observe the material surface colonization is electron microscopy, these results highlight the usefulness and also the validity of microCT. Thus, SEM and microCT might be two complementary approaches aimed at evaluating from different points of view an engineered construct over time: SEM is useful to investigate the material surface, whereas microCT allows the scaffold to be assessed three-dimensionally in terms of cell colonization and increasing material degradation rate [54]. CLSM technique also allows collection of data in 3D, but there are depth limitations due mostly to the diffusion of the fluorophores into the sample and to the illumination light penetration or internal sample diffraction; the maximum focal plane achievable is in fact considered in the range of 200-300 μm [55].

One of the aim of the present study was to establish a segmentation protocol for microCT images to detect cells within the PCL scaffolds and

validate the method through statistical comparisons with DNA content quantification. In fact, an incorrect determination of the threshold value for the segmentation could affect significantly the accuracy in measurements. The nominal resolution used here (2.5 μm of pixel size) allowed the detection of even isolated cells far from the surface. Furthermore, there were far fewer clusters than in previous studies [44, 50] even though they were still present especially at the surface (Figure 7.6c). Improving the image quality with higher resolution could, in the future, also improve the absolute accuracy increasing the detectability of smaller structural details. Despite the high resolution utilized, histograms of grey levels do not yet allow a precise segmentation of the cells compromising their exact detectability. This is due to the absence of defined peaks and the fact that the use of standard automatic algorithms, such as that proposed by Otsu [56], is not effective since it also includes part of the scaffold material. The characteristic of MG63 osteosarcoma cell line of growing in multilayers and continuing to proliferate over time, was used to ensure the presence of cell colonization even in deeper layers of the scaffold. The method presented here was developed after observing the X-ray attenuation histograms obtained. Given that the histograms of the samples, cultivated with MG63 at different experimental times and different concentrations, started to diverge at a certain level of grey onwards, this value was used to discriminate the polymeric material of the scaffold from the cells present. Obviously, this type of procedure implies a certain amount of error due to signal noise. The presence of noise can be also estimated from the histograms obtained from the scaffolds without MG63 cells (Figure 7.1a). The authors believe that the method described is good for 3D quantification of cell distribution considering the intrinsic properties of microCT analysis. Indeed, due to its 3D analysis nature, microCT allows combining the results with the results obtained by qualitative surface analysis and gives a more complete understanding of cell colonization. By observing all images, in addition to a more extensive distribution of cells on scaffolds surfaces than in the deeper layers, cell volume increased at 2 weeks compared to 1 week after seeding. The possibility to analyze the sample three-dimensionally by

microCT is extremely helpful when there is a need to combine the results with biological data. However, the assessment of the merely cell number by DNA quantification is not proper to validate microCT quantification of cell volume fraction in a scaffold. Volume and shape are indeed important elements to describe the cell viability and its binding to a substrate over time. It is known that the cells have spherical shape before being seeded onto a substrate -such as culture well bottom or different materials scaffold - and if the interaction reveals promising, the cell shape changes even after short time (i.e. 24 hours) to become elongated and flattened. Morphological and volumetric alterations, driven by active reorganization of the cytoskeleton, have thus to be taken into account to obtain a correct value of the scaffold volume colonized by the cells [57]. Surface observation (for example by SEM) or observation of the most superficial layers alone (for example by CLSM) might therefore not be sufficient for a correct correlation with quantitative biological data obtained from the entire scaffold. Combining the cell number quantification by DNA analysis and the single cell volume changes by CLSM, we validated the microCT methods by finding no statistical differences in the evaluation of the cell volume fraction of the entire scaffold.

Furthermore, the morphological results of this study suggest that the correct scaffold colonization for subsequent extracellular matrix synthesis in tissue engineering constructs requires a precise balance between different factors. Usually, the first most important element to be considered is the scaffold porosity but, from a biological point of view, particular attention may be also given to the number, type and size of seeded cells, as well as the seeding technique, to avoid an excessive and fast colonization of the scaffold periphery. An inappropriate combination of all the involved elements might, for example, give rise to a thick, superficial cell layer which can act as an effective barrier to the diffusion of oxygen and nutrients inside the scaffold [58], thus preventing the normal proliferation and viability of the cells in the construct volume. Technically, a superficial cell layer could also hamper the DNA evaluation preventing a correct perfusion of the scaffold by the

lysis solution, that has to be used at minimal quantity, and lead an over-capture of osmium before SEM and microCT analysis.

In this preliminary study, focused on to perform a cells visualization method by microCT, the used cell seeding technique was static. Consequently the imperfect cell distribution observed in 3D model (Figure 7.6c) could be caused by the seeding technique, and the most suitable colonization method will be the aim of next papers. However, a cell infiltration capacity was observed within the scaffolds due to the topological properties of their pore structure, and a dynamic seeding technique could surely represent a further improving of scaffold colonization.

The possibility that both PicoGreen test, which quantifies the DNA and consequently the cell number by binding the double strand of nucleic acid, and osmium tetroxide, which highlights the cells by binding the membrane lipids, could label also dead cells, is another limitation of the proposed method. This problem should be overcome, however, by the repeated medium changes and the series of wash steps performed during the cell colture study.

The use of microCT for the detection of cells seeded onto a scaffold for tissue engineering offers the possibility to show the surface cell density with results comparable to those of SEM and CLSM. This was possible using increasingly sophisticated software and a high resolution (2.5 μm). Not only scaffold properties such as porosity, pore size and pore geometry can be tailored to dictate the mechanism of tissue regeneration and the structure of the resulting tissue [42], but the way in which cells proliferate and adhere to three-dimensional scaffolds can be also tailored. In the future it would be interesting to test other cell lines used in tissue engineering, such as hMSC (human mesenchymal stromal cells), because their ability to infiltrate the PCL scaffold has already been proved [53], and hADSC (primary human adipose derived stromal cells), because of their ability to undergo osteogenic differentiation as well as hMSC [59-60] and the interest in them that is greatly increasing [61-64].

ACKNOWLEDGMENTS

This research has been supported by a grant from the Italian Ministry of Health: Firb TissueNet n. RBPR05RSM2 and Firb n.RBAP10MLK7. The authors are also grateful to Rizzoli Orthopaedic Institute and funds 5 X 1000 (year 2008-2009).

Chapter 8
Preliminary study on the quantification of wear in Zirconium dioxide femoral head using micro-CT

8.1 Introduction

Total hip replacement (THR) is one of the most common surgical procedures in the treatment of chronic arthritis and involves, nowadays a very high number of patients worldwide [65-66].

The main problem associated with THR is orthopedic implant wear, which is directly related to prosthetic failure and revision surgery [65, 67]. Consequently, the evaluation of wear volume is of primary importance and constitutes, amongst others, the preclinical validation of prostheses [67-68]. Wear volume evaluations of worn prosthesis is fundamental for acquiring further knowledge about tribological processes in joint prostheses [65] and guiding future development efforts to solve or reduce wear problems preventing, in this way, the possibility of unexpected failure.

There are several methods to quantitatively evaluate wear including radiographic [69-70], optical [71], gravimetric [72-73] and volumetric techniques [66-68, 74-78]. Nowadays the standard method used to assess wear in hip joint prosthetic components is the gravimetric method. The procedure requires a microbalance with an accuracy of ±0.1 mg and consists in measuring the specimen weight before and after wear and calculating the weight loss as the difference between the two measures [79]. The usefulness of gravimetric method is however limited in some cases. Indeed, for example, information on local form change of the wear surface is not provided, it is not possible to assess wear mechanism on explanted prosthesis, or damages like deformations are not measurable [74]. Recently, the volumetric methods, like coordinate measuring machine (CMM) and micro computed tomography (micro-CT) techniques, are been used as alternatives to overcome the gravimetric method limitations [66-68, 74-78]. In particular micro-CT is considered a promising technology for dimensional metrology [80-82] because of its intrinsic advantages. Micro-CT is a non-destructive testing technique based on X-rays that gives quantitative 3D information of a whole object structure in a relative reduced time and provides geometric information also of inner and hidden surfaces [82-84]. The realization of the reconstructed images, that constitute the 3D dataset of the analyzed object, is based on the assumption that X-rays are attenuated in a certain point independently from the propagation path length. This principle is however valid only for monoenergetic radiation beam, while the common micro-CT systems used in the field of dimensional metrology are equipped with polyenergetic X-ray beam sources. The polychromatic character of the used X-ray spectrum implies that the linear attenuation coefficient μ of the material changes non-linearly along the propagation path. Low energy photons are attenuated more rapidly than high energy photons while they are penetrating materials and, then, the ray beam becomes harder. This effect is called beam hardening and causes cupping artifacts on the reconstructed images [85-87]. This means that the reconstructed value in the central area of a homogeneous analyzed object is lower than in the vicinity of its surface border, looking like a density

change depending on the position in its volume [86]. Materials like steel and Zirconium dioxide (ZrO_2), that are widely used in prosthesis manufacturing field, attenuates a lot X-rays causing severe beam hardening artifacts due to their density [82]. Beam hardening is one of the limitations of micro-CT technique as well as other parameters like the source power (voltage and current) or the appropriate specimen orientation [81]. The choice of a proper voltage for homogeneous high density materials, such as those the femur heads are made, should be set high enough to avoid total beam extinction during the passage through the specimen. The main problem in this context is that most of the microtomographic system normally used in medical labs does not exceed 100kV, which is a source voltage perfect for studies on bone but not enough high for a lot of prosthesis. Indeed, at the state of the art micro-CT analysis on prosthesis components wear consider just those made by polyethylene (PE) [67, 76-77, 88-89]. In addition, other limitation stems from finding an adequate gray value threshold because all dimensional measurements using micro-CT are based on the determination of the material boundary [81]. On the other hand, micro-CT analysis does not require any information about implant geometry (such as head original size) which is an important advantage especially in case of retrieval analysis on an explanted device. In most of the cases is indeed not possible to recover the original manufacturing drawings [67].

The present work describes a pilot study to establishing an approach for the quantification of wear in Zirconium dioxide head prosthesis components using a micro-CT system and to validate the method comparing it with gold standard gravimetric analysis.

8.2 Materials and Methods

As a pilot study, three new, non implanted ZrO_2 femoral head components (Norton Desmarquest) with a diameter of 22.22 mm were used to compare Micro-CT to gravimetric measurements. The heads were

evaluated before and after being worn. To simulate a hip joint severe wear, material was eroded from the surface of the heads. Each component was cleaned with acetone before the measurements with both methods and stored for stabilization in a temperature and humidity controlled room.

For the gravimetric method it was used a microbalance (Denver Instruments, USA) with an expanded measurement uncertainty of ±0.1 mg to measure weight loss from the unworn to the worn status of the heads. Each weight measurement was conducted in triplicate and the average value was stored. The density value used to calculate the weight loss in volume of the ceramic heads was 6.05 g/cm^3.

For the volumetric method it was used the micro-CT system Skyscan 1172 (Bruker Micro-CT, Belgium). To achieve the best possible alignment of the heads, it was built a custom-designed support co-aligning the bottom head surface to the scan chamber surface. All the femoral components were scanned in triplicate before and after being worn at 100 kV of source voltage and 100 μA of source current. The rotation of the specimen was 360° with rotation step of 0.5° and frame averaging of 8. It was used an aluminum filter of 0.5mm between the source and the samples. The image pixel size was 30 μm and the scan duration was nearly 40 minutes each head (s/w Skyscan 1172 version 1.5 build 8). The acquisition was carried out on two vertical connected and consecutive field of view (FOV) to obtain nearly 1500 images in 16-bits TIFF format (1000X524 pixels) each sample.

The reconstructions were performed using s/w NRecon (version 1.6.2.0) and the resulted 8-bits JPG images had 1000X1000 pixels with a pixel size of 30 μm. No corrections were used but the specific misalignment for each acquisition.

The micro-CT analysis was carried out using a dedicated software (CTAnalyzer Bruker Micro-CT, Belgium) on the reconstructed images. The 3D measurement of the head volume was carried out on the upper hemisphere of each scan images dataset.

First, the images were segmented considering a gray value threshold calculated using the method proposed by Otsu in a tri-level mode [90-

92]. Due to the severe beam hardening occurred, it was assumed to identify 2 thresholds in the images. These thresholds divided the original images into 3 classes: the first class identified the surrounding background, the second class identified the inner space of the heads and the third class identified the head surface borders. The tri-level thresholded images were then segmented again with a global threshold that identified just the voxels of the third class relative to the surface borders. Afterwards, the images were completed by software filling of the inner empty space. The volume in mm^3 was directly calculated on these segmented hemispheres.

8.3 Results

Due to the severe beam hardening effect occurred, the reconstructed CT images appear with the outer surface of the femoral head section much lighter than the inner core (Figure 8.1a). After the tri-level segmentation, the images are divided in three classes of objects detected: the background, the specimen inner space and the specimen surface border (Figure 8.1b). A further segmentation isolates the only surface border (Figure 8.1c) that is then used as the boundary for a software filling of the femur head (Figure 8.1d).

The comparison between micro-CT measurement and the golden standard gravimetric method was performed through the following procedure already described by Carmignato et all. [74]:

(a) Gravimetric measurement of unworn specimens.

(b) Micro-CT measurement of unworn specimens.

(c) Controlled wear of specimens.

(d) Gravimetric measurement of worn specimens.

(e) Micro-CT measurement of unworn specimens.

(f) Comparison of gravimetric and Micro-CT volumetric results, considering the material density.

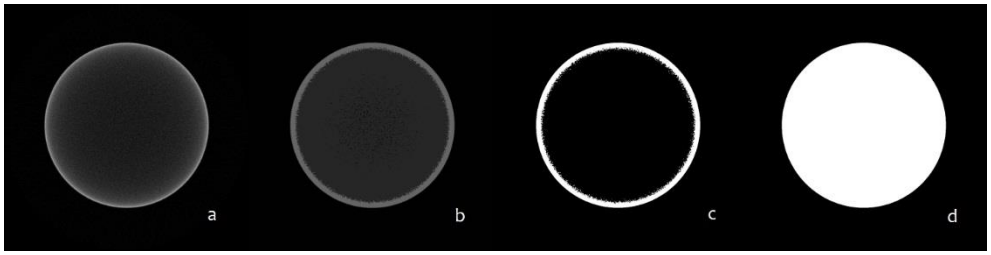

Figure 8.1 *– Micro-CT sections of Zirconia dioxide femoral head components at different step of threshold. a) original image; b) multilevel threshold applied; c) detection of the boundary; d) software filling of the internal part of the femoral head.*

The results of the comparison between wear volume measurements from micro-CT analysis and wear volume measurements from gravimetric method are shown in Table 8.1.

Specimen	Wear Volume, micro-CT (mm^3)± SD	Wear volume, gravimetric (mm^3)± SD
Head #1	7.22 ± 2.36	5.54 ± 0.00
Head #2	6.93 ± 6.94	4.28 ± 0.00
Head #3	8.25 ± 5.35	10.98 ± 0.00

Table 8.1 *– Comparison of micro-CT and gravimetric method.*

The Figure 8.2 shows the difference between the two methods of wear measurements in a graph where micro-CT results are plotted against the gravimetric ones. The graph exhibit an excellent linear correlation (R^2 = 0.9989).

Besides, 3D virtual models of the unworn and worn specimens were created. These models provide a qualitative evaluation and allow in localizing the volume loss and in defining its geometry, actions that are impossible using the gravimetric method (Figure 8.3).

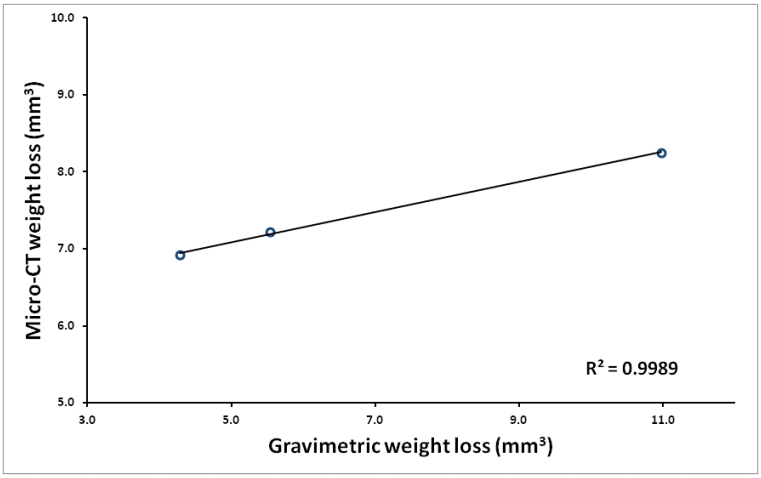

Figure 8.2 *– Correlation between Micro-CT and gravimetric methods in measuring weight loss of a ZrO_2 femoral head.*

8.4 Discussion

The volumetric methods, used to evaluate wear in preclinical prosthesis validation studies, are becoming more and more important and effective. This depends on the information that they provide compared to the golden standard gravimetric method. In particular the volumetric micro-CT method has some advantageous characteristics such as the relatively short time of each specimen scanning, the ability of evaluating specimens without touching their surfaces and the capability of analyzing the specimens structures also locally.

The aim of the present study was to widen the knowledge on micro-CT analysis of wear. For this purpose, the volume loss of ZrO_2 femur heads prosthesis was calculated with a lab commercial high resolution micro-CT system which is relatively frequently suited for routine laboratory or preclinical application.

At the state of the art, there are some other studies that are starting to deal with micro-CT quantification of wear. However, the other authors validated the method just for PE prosthesis [67, 76-77, 88, 93-94]. A lot of orthopedic implants used for THR have however components made by materials with higher densities (ceramic or steel).

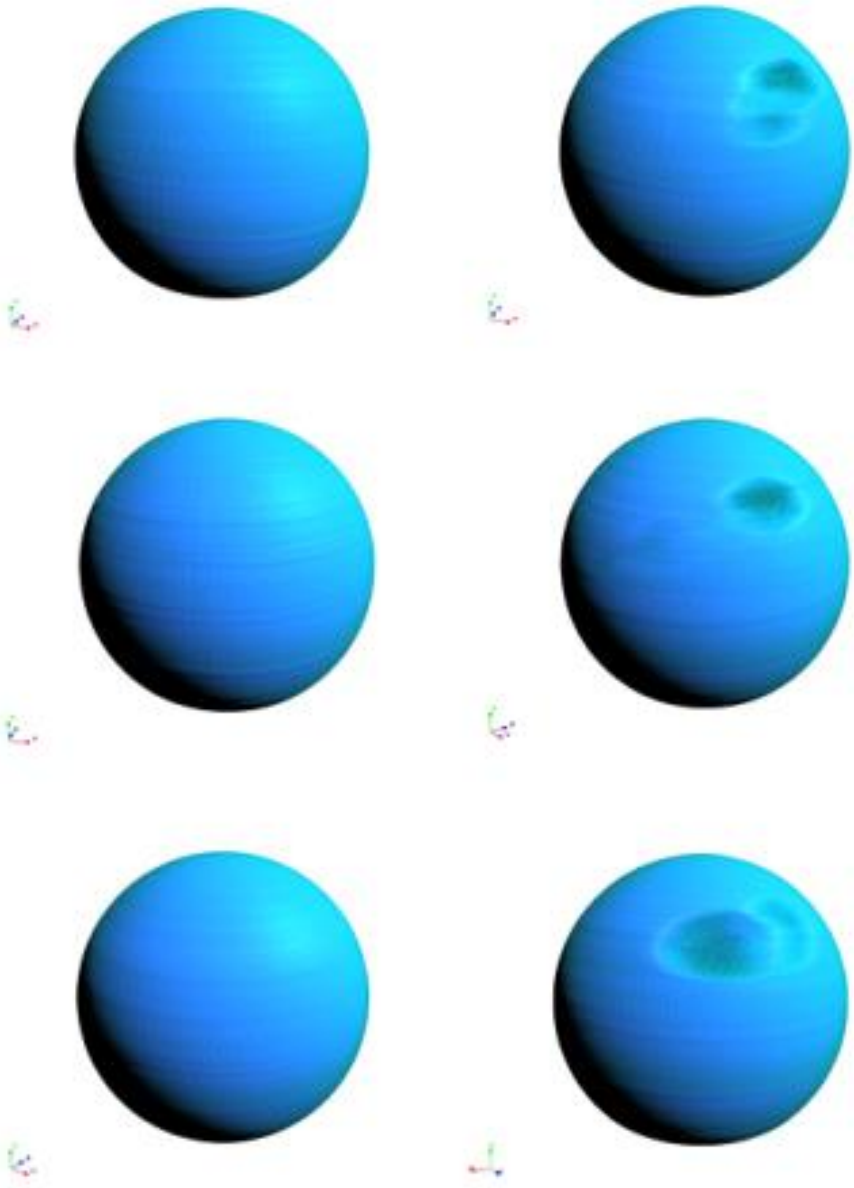

Figure 8.3 *– 3D virtual models, based on the microtomographic sections, of the unworn (on the left) and worn (on the right) specimens.*

The problem in analyzing ZrO_2 prosthesis with a micro-CT system is related to the severe beam hardening artifacts that occurs. In the most of micro-CT systems used in biomedical laboratory for pre-clinical evaluations, the X-ray source works at about 20-100 kV. The maximum applicable voltage is thus not enough elevate for a high dense material such as Zirconium dioxide. This aspect, together with the relative thickness of the femur prosthesis component, implies the beam hardening artifact problem observed within the analysis.

To overcome this limitation, a segmentation protocol taking into account the difference in gray levels between the surface and the core of the heads in the microtomographic sections was established. In addition, it is important to underline that the definition of a segmentation protocol is necessary to improve the reliability of the results, overcome the variability and make the analysis repeatable regardless of the operator [39].

To assess accuracy, the micro-CT volume measurements were compared to the gravimetric measurements, while, to assess the precision of micro-CT wear analysis, the quantification were carried out in triplicate. The results showed an excellent linear correlation between the two methods ($R^2 = 0.9989$). Despite this, the single volume measurement average in mm^3 of each heads is considerably different (about 2 mm^3) if calculated with the micro-CT compared to the gravimetric method. This low agreement could depend on many different factors. The most important is that the measurements were carried out in a free geometrically way. This means that no unworn reference surface geometry was co-aligned to measure the wear but it was just calculated the difference between the worn and the unworn volume of the specimen after the only segmentation. The advantage lies on the fact that without a reference surface the measurements are influenced only on the acquisition and on the segmentation. Thus, other sources of error are removed. Working free geometrically, however, involves the problem of orientation of the specimen during acquisition. In micro-CT systems the X-ray source and the detector are usually fixed, while the specimen rotates between them [81]. A perfect alignment with the axis of the scanning

chamber floor and a perfect rotation barycenter are fundamental to obtain repeatable datasets of microtomographic images. Thus, another factor that affected the agreement of the single volume measurement average between micro-CT and gravimetric analysis was the not perfect alignment of the specimens during the acquisition, although a custom specimen holder was built. The high nominal resolution used (30 μm) did not allow the perfect post-alignment of the specimen at the same scale of measurement. This implied small differences in the hemisphere estimation.

In addition to the possible causes that have affected the precision of the micro-CT volume measurements, the accuracy could have been influenced by the threshold method proposed because the accuracy of the edge detection is directly related to the accuracy of the measurements [95]. In the present study, edge detection was strongly directly related to beam hardening. The nonparametric multi-level Otsu method was used to detect the edge with the higher contrast in the image sections. Instead using beam hardening correction algorithms, whose effectiveness in improving the dimensional accuracy has not yet verified [95], the artifact as an advantage in edge determination was used.

Up to date, there is still no literature available concerning international standards or guidelines to evaluate the uncertainty in CT measurements [81]. The wear evaluation proposed in this study is repeatable and operator independent. The methodology requires anyway further works that will, for example, validate the threshold method finding a correlation coefficient for volume measurements. It would be advisable to consider also the material thickness as a parameter of the correct threshold value finding.

Wear volumes evaluations of hip joints prostheses is a fundamental topic for acquiring further knowledge about tribological processes.

The results obtained from this wear evaluation methodology increase the understanding of using micro-CT in dimensional metrology on ceramic heads components. Further works will improve its reliability and accuracy.

Chapter 9
Long-Term Results following Cranial Hydroxyapatite Prosthesis Implantation in a Large Skull Defect Model [96]

Lucia Martini[1,2], Guido Staffa[3], Gianluca Giavaresi[1,2], Francesca Salamanna[1], Annapaola Parrilli[1], Elena Serchi[4], Daniele Pressato[5], Elena Arcangeli[5], Milena Fini[1,2]

[1] Biocompatibility, Technological Innovations and Advanced Therapies Laboratory (BITTA), Rizzoli RIT Department, Rizzoli Orthopaedic Institute, Italy
[2] Laboratory of Preclinical and Surgical Studies, Rizzoli Orthopaedic Institute, Italy
[3] Division of Neurotraumatology, Umberto I Hospital, Lugo (RA), Italy
[4] Division of Neurotraumatology, Bellaria Hospital, Bologna, Italy
[5] Fin-Ceramica Faenza S.p.A., Faenza (RA), Italy

ABSTRACT

Background: A large skull defect may occur after different events such as trauma, tumour resection, vascular injuries etc. There is still some

doubt about the best material to use for reconstruction. Hydroxyapatite ceramic is one of the materials in use and its biocompatibility and osteoconductivity are well established. This study evaluated the interaction of a commercial hydroxyapatite custom-made prosthesis implanted in a large skull defect, to assess its osteointegration and its habitability with new formed bone over time.

Methods: Ten sheep underwent craniectomy and reconstruction of the skull defect with a porous hydroxyapatite cranial prosthesis. The animals were divided into two groups: Group A was sacrificed after 6 months and Group B after 12 months. At the end of the experimental times each implant was evaluated macroscopically, radiologically and analyzed by micro-CT, histology, histomorphometry and microhardness techniques.

Results: During the study no adverse events occurred and there was no evidence of inflammation or negative tissue reactions. Histology and histomorphometry showed new bone formation inside the implant at both experimental times; newly formed bone had increased significantly (p <0.05) by over 300% between 6 and 12 months. 3D micro-CT analysis showed new bone formation and material remodeling. Microhardness analysis indicated that the mineralization process and the mechanical properties of newly formed bone were not altered.

Conclusions: The hydroxyapatite prosthesis showed its osteoconductivity and good biocompatibility. A low rate of fibrous tissue formation and a high rate of bony regeneration was found.

9.1 Introduction

A cranioplasty should fulfil two main requirements: (1) protect the brain and a (2) provide good cosmetic result. The ideal material for cranioplasty should be chemically inert, biocompatible, biomechanically reliable, easily manufactured, individually shaped, safe, and able to promote osteoblast migration [97-101].

Many devices have been implanted over time, and the advent of

customized prostheses defined a new era in reconstructive skull surgery [97-102].

Fresh autologous bone is theoretically the criterion standard for cranioplasty. However, when the skull defect reconstruction is extensive (≥25 cm^2), limited availability can limit the implant because of the donor site morbidity [97-107].

Conventional materials, such as the acrylic resin, phosphatic cement, and titanium mesh used in the intraoperative modeling approach, partially lack the properties for large and complex cranial defect reconstruction [97, 99, 101-103, 108-113].

The custom-made concept was first applied to porous hydroxyapatite because of the need to overcome the fragility of the material itself. Hydroxyapatite had some crucial advantages over polymeric or metallic materials because of the bone-bonding properties of calcium-phosphate ceramics, and the porous morphology makes this material very similar to the mineral phase of bone. The number and size distribution of pores in the ceramic allow the migration of blood vessels and bone tissue into the prosthesis [114-115]. Moreover, the density and interconnection of the pores ensure the durability of this material as a bone substitute [116].

The use of porous hydroxyapatite in experimental models and clinical applications for cranioplasty has been successful because of its similar chemical composition to the mineral phase of bone [97-98, 102, 104, 108-109]. The purpose of this study was to evaluate the *in vivo* behavior of a custom-made hydroxyapatite prosthesis, implanted in a sheep model, 6 and 12 months after cranioplasty. The evaluation focused on the osteointegration process of the prosthesis at the edge of host bone and on the habitability of the prosthesis by the newly formed bone over time. Because the routine procedure to treat large skull lesions (e.g., the removal of a large cranial tumor) is to reconstruct the bone defect in the same surgical setting, the current authors applied the same one-step procedure to all of the animals.

9.2 Materials and Methods

9.2.1 Prosthesis Manufacture

A standard implant was manufactured on the basis of sheep cranial bones collected from animals previously euthanized in an uncorrelated study. A chalk prototype of the skull defect was made; the prostheses were then manufactured according to the internal standard procedure for CustomBone Service Cranial prostheses production (Fin-Ceramica S.p.A., Faenza, Italy), and sterilized with gamma irradiation (GammaRad Italia S.p.A., Bologna, Italy) [105]. The implant porosity (macroporosity, 200 to 500 μm; microporosity, 1 to 10 μm) was the best compromise between a microarchitecture ensuring a structural biomimesis, mechanical strength, and handling properties of the implant.

9.2.2 Study Design and Surgical Procedure

This study was carried out according to Italian law on animal experimental testing and the Guide for the Care and Use of Laboratory Animals and approved by the ethics committee of the Rizzoli Orthopaedic Institute. Ten adult Merinos-Sarda female sheep, aged 3.0 ± 0.5 years and weighing 65 ± 5 kg (Pancaldi, Bologna, Italy), were selected. The animals were housed in standard and controlled conditions (temperature, 22 ± 1° C; relative humidity, 55 ± 10 percent; and ventilation, 10 air changes per hour) and fed with a maintenance diet (Mucedola, Settimo Milanese, Italy), clover, and water at libitum. Ten days after surgery, the animals were allowed to graze until they were euthanized.

After premedication with intramuscular administration of 10 mg/kg ketamine (Imalgene 1000; Merial, Italia S.p.A., Milan, Italy) and 0.3 mg/kg xylazine (Rompun; Bayer, Milan, Italy) and 0.125 mg/kg subcutaneous atropine sulfate, general anesthesia was induced by

intravenous thiopentone sodium in 2.5% solution (6 mg/kg) (Thiopental Inresa; Inresa Arzneimittel, Freiburg, Germany). General anesthesia was maintained by endotracheal tube with administration of isoflurane 2% (Aerrane; Baxter S.p.A., Rome, Italy) in oxygen/nitrous oxide (60%/40%), 7 liters/minute (900D Servo Ventilator; Siemens, Munich, Germany).

With a linear midsagittal skin incision, the parietal bone was exposed and the skull defect was obtained by a standard craniectomy procedure by using an air driver craniotome (Codman & Shurtleff, Inc., a Johnson & Johnson Medical Division, Rome, Italy). The dura was exposed and the prosthesis was positioned and fixed to the bone with three silk stitches. The skin was closed and medication administered as for the standard procedure. Animals were divided into two groups: group A at 6 months and group B at 12 months.

Antibiotics [cephalosporin 1, g/day for 5 days (Cefamezin; Pfizer Italia S.r.l., Latina, Italy)] and analgesics [metamizole sodium, 50 mg/kg/day for 3 days (Farmolisina; Ceva Vetem, S.p.A., Agrate Brianza, Italy)] were administered. At the end of the experimental time, all of the animals were euthanized by means of Tanax (Hoechst, Frankfurt am Main, Germany) under general anesthesia. A new craniotomy was made to obtain a specimen composed of the prosthesis in the center part surrounded by host bone. The implants were subsequently analyzed macroscopically, radiographically (Nessey HF30, Raffaello; ACEM S.p.A., Bologna, Italy) histologically, histomorphometrically, microtomographically, and mechanically.

9.2.3 Histology and Histomorphometry

The samples were fixed in 4% paraformaldehyde, dehydrated in a graded series of alcohol, and embedded in polymethylmethacrylate (Merck, Darmstadt, Germany). Blocks were cut through the two main axes (longitudinal and sagittal), thus obtaining four quadrants: right anterior, left anterior, right posterior, and left posterior (Figure 9.1).

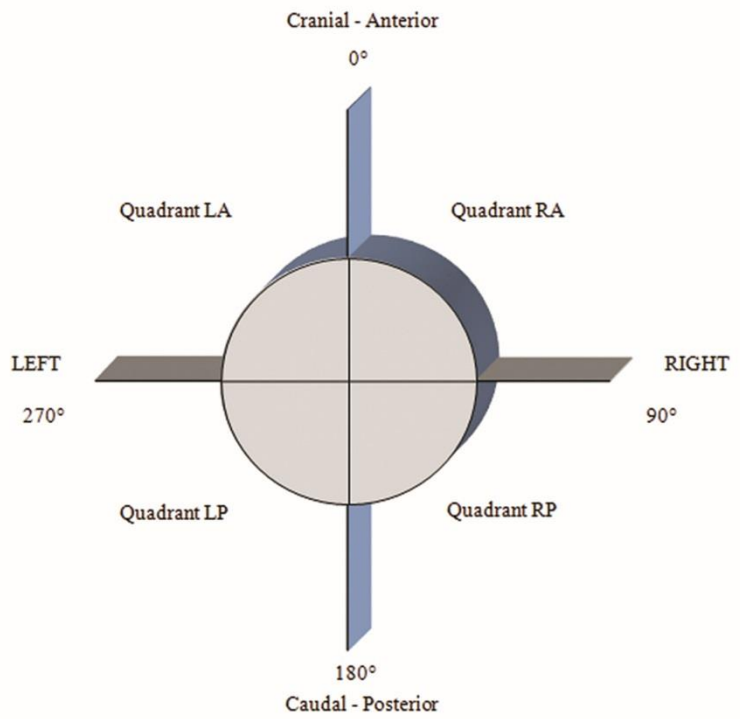

Figure 9.1 *– Scheme of skull divided into four quadrants: right anterior (RA), left anterior (LA), right posterior (RP), and left posterior (LP).*

From the surfaces of the right anterior and left posterior quadrants, 250 ±100-µm-thick sections were obtained, thinned to 40 ± 10 µm (EXAKT ApparatebauGmbH&Co., Norderstedt, Germany), and stained with toluidine blue, acid fuchsin, and chromoxane cyanine R. The histologic and histomorphometric analyses were carried out with computerized image analysis using AxioVision 4.6 (Carl Zeiss GmbH, Oberkochen, Germany).

Sections were analyzed by two blinded investigators considering the peri-implant bone, the implant, the subcutaneous space, and the suprameningeal space (Figure 9.2). Osteoconductivity responses, biocompatibility, bone formation, and the biological reaction in surrounding tissues were investigated. The histomorphometric parameters evaluated [117] are listed in Table 9.1.

Figure 9.2 *– Representation of the region of interest of cranioplasty: peri-implant bone, implant, subcutaneous space, and suprameningeal space. Image was generated by means of an Epson Perfection 2480 Photo scanner (Seiko Epson Corp., Nagano, Japan), with a resolution of 1200 dpi.*

9.2.4 Biomechanical Test

The left anterior quadrants of each sample were used for bone microhardness measurements using an indentation test with Microhardness VMHT 30 (Leica, Wien, Austria). Microhardness measurements were performed with a Vickers indenter applied to the bone with a load of 0.05 kgf for 5 seconds. Host bone microhardness, bone at the implant interface, prosthesis material, and newly formed bone microhardness in the implant area were divided into three smaller regions and measured as described in Table 9.2.

9.2.5 Micro-Computed Tomographic Analysis

The right posterior quadrants of all skull samples and those of five prostheses without implants were scanned using micro–computed

Parameter	Description
BIC (%)	The bone grown right up to the implant surface without interposed fibrous tissue
BV/TV (%)	Calculated by dividing the amount of trabecular bone (B.Ar) by the total area of the region of interest (T.Ar), multiple by $4/\pi \cdot 100$: $\frac{B.Ar}{T.Ar} \cdot \frac{4}{\pi} \cdot 100$
NewBV/BV (%)	Index of the newest formed bone
Tb.Th (μm)	Because the trabecular bone of the skull was different from other anatomical sites because of higher thickness of trabeculae, it was not possible to use the Parfitt formulas to calculate the Tb.Th, Tb.N, and Tb.Sp; therefore, an interactive measurement of the latter parameters was performed using a number of 10 repeated measures for each one
Tb.N (mm)	
Tb.Sp (μm)	
Fib.Tis.Th (μm)	Calculated the average of 10 repeated measures of the thickness of the fibrous connective tissue that grew at the interface between host bone and implant in the event that the BIC is lower than 25%
Mat.V/TV (%)	Calculated by dividing the amount of material by the total area of the region of interest (T.Ar), multiple by $4/\pi \cdot 100$: $\frac{Mat.Ar}{T.Ar} \cdot \frac{4}{\pi} \cdot 100$

BIC, bone-to-implant contact; BV/TV, trabecular bone volume; NewBV/BV, newly formed bone volume; Tb.Th, trabecular thickness; Tb.N, trabecular number; Tb.Sp, trabecular separation; Fib.Tis.Th, thickness of fibrous tissue; Mat.V/TV, material volume.

Table 9.1 *– Histomorphometric Parameters.*

tomography SkyScan 1172 (SkyScan, Kontich, Belgium); the nonimplanted prostheses were used as control material to evaluate the supposed remodeling process after implantation. The scans were performed with a voltage source of 100 kV, a current source of 100 μA, a 17μm pixel size, a 0.5-mm aluminium filter, a sample rotation of 180°, and a rotation step of 0.4°. Two related scans for each sample were made and reconstructed with the same alignment. Reconstruction was performed by using NRecon-Software (version 1.6.1.5; SkyScan): a specific alignment was used for each sample and a medium intensity ring artifact correction was applied. Three-dimensional analyses were performed using the CTAn Software (version 1.10.1.0; SkyScan), and images of the three-dimensional models were obtained by CTVol Software (version 2.1.1.2; SkyScan). The three-dimensional test was performed on the entire right posterior quadrant considering a volume of interest in the implant area. The morphometric parameters derived in part from those defined by Parfitt [117-118] are listed in Table 9.3.

Parameter	Description
The index of bone microhardness (HV)	Calculated by dividing the indentation strength for the imprint surface left on the bone and observed under the microscope
Bone maturation index (BMI %)	Calculated by dividing the HV of newly formed bone by the HV of host bone, multiplied by 100: $BMI = \frac{\text{bone microhardness (HV) of new done}}{\text{Hv of host bone}} \cdot 100$

HV, Vickers Hardness Index; BMI, bone mineralization index.

Table 9.2 – Microhardness Parameters.

9.2.6 Statistical Analysis

SPSS software version 12.1 (SPSS, Inc., Chicago, Ill.) was used. Data are reported as mean ± SD at a significance level of p 0.05. The t test was used to compare data. One-way analysis of variance and the post hoc Bonferroni test were used to compare micro–computed tomographic and microhardness results.

9.3 Results

All of the animals tolerated the surgical procedure without any sign of infection.

9.3.1 Radiographic Evaluation

Radiographic images at 6 months revealed that the implants had partially osteointegrated. Two implants showed microfragmentation located at the edges of the devices following the suture passage. After 12 months, the cranioplasties showed good osteointegration, and only one of the specimens showed signs of microfracture.

Parameters	Description
PoreV/TV (%)	Expressed as a ratio between the volume of material measured in the implant VOI and the total volume of the considered VOI
Pore connection (%)	Pore connection within the implant performed with a three-dimensional individual analysis on the pores: $\frac{V_{max\ detected\ pores}}{\sum V_{detected\ pores}} \cdot 100$
PoreTh (μm)	Index of porous width, within the implant measured as a true model-independent three-dimensional value
PoreSp (μm)	Pore separation within the implant derived from the volume-based local thickness by just applying the method to the space (material and bone) other than the pore voxels; this gives an indication of the amount of solid phase (hydroxyapatite and/or bone)
PoreSp distribution	Pore separation distribution within the implant that gives an indication of the behavior of material remodeling and new bone formation

VOI, volume of interest; PoreV/TV, porosity; PoreTh, pore thickness; PoreSp, pore separation.

***Table 9.3** – Micro–Computed Tomographic Three-Dimensional Morphometric Parameters.*

9.3.2 Histologic Evaluation

Group A revealed different conditions regarding the peri-implant bone and the prosthesis osteointegration. Two cases showed that the prosthesis was completely osteointegrated without the presence of connective tissue at the bone/hydroxyapatite interface (Figure 9.3, above, left). The newly formed bone was discernible from pre-existing peri-implant bone because of the smaller and thinner trabeculae. In the other three cases, the prosthesis was in direct contact with regrown bone, and a dense connective tissue layer between new and preexisting bone was observed (Figure 9.3, above, right). In the suprameningeal space, there was connective tissue interspersed with bone, except in one case, where there was only connective tissue. Newly formed bone was observed inside the implant and showed a lamellar structure indicating remodeling activity (Figure 9.3, below).

Group B showed that the prosthesis was closely osteointegrated with the peri-implant bone in all cases (Figure 9.4, above, left). In the suprameningeal space, a thin layer of connective tissue interspersed with bone was found. The presence of newly formed bone tightly compact and well adherent to the material of the prosthesis was observed at the bone/biomaterial interface and inside the implant (Figure 9.4, above, right and below). In all cases, there was an absence of inflammatory cells at both experimental times.

9.3.3 Histomorphometric Evaluation

Bone-to-implant contact increased significantly by approximately 49.6 percent between 6 and 12 months. No significant differences were found for trabecular bone volume in the peri-implant bone (Table 9.4) or in the suprameningeal space (group A, 19.4 ± 2.1 percent; group B, 13.0 ±11.1 percent) between 6 and 12 months. Trabecular bone volume inside the implant increased significantly ($p<0.05$) by over 300 percent between 6

and 12 months, becoming histologically more similar to the host bone architecture, as shown also by the measure of trabecular thickness (130 percent) ($p<0.0005$) and the decrease in the newest formed bone volume (–58.9 percent) ($p<0.0005$). Significant reductions of approximately 25 percent were observed in material volume ($p<0.0005$) and thickness of fibrous tissue ($p<0.05$) between experimental times inside the implant and in peri-implant bone, respectively.

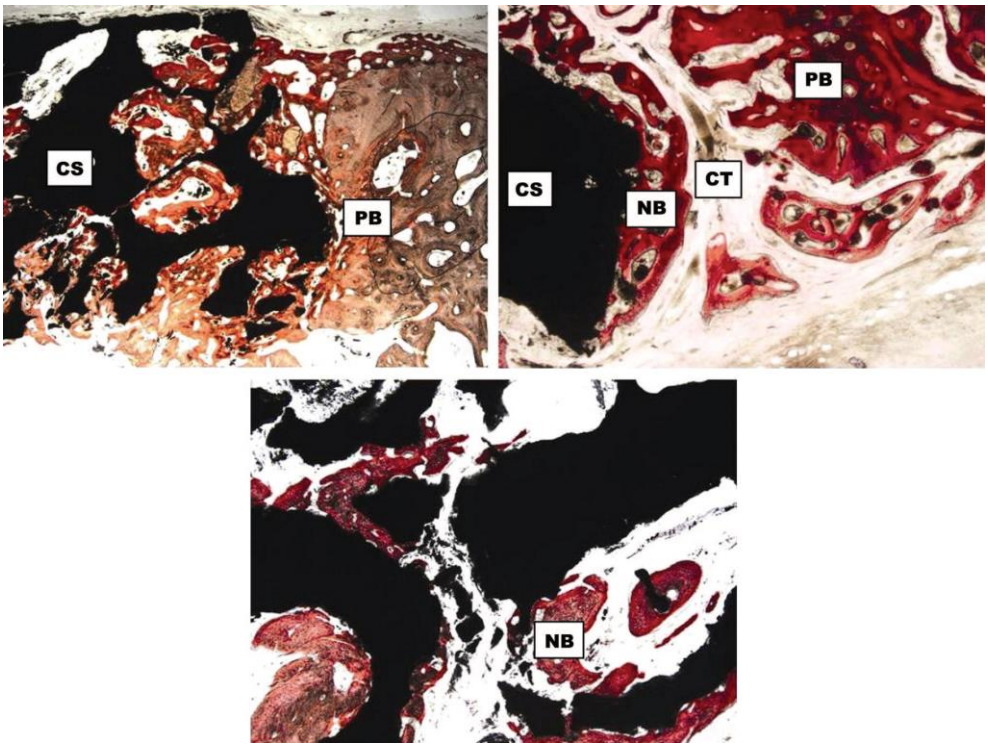

Figure 9.3 *– Light microscopic images of cranioplasty obtained 6 months postoperatively (toluidine blue, acid fuchsin, and chromoxane cyanine R staining; original magnification, X2). (Above, left) Cranial substitute in close contact with the peri-implant bone; (above, right) cranial substitute packed with a thin layer of newly formed bone and separated from peri implant bone by connective tissue; (below) cranial substitute with newly formed bone (original magnification, X4). PB, peri-implant bone; CS, cranial substitute; NB, newly formed bone; CT, connective tissue.*

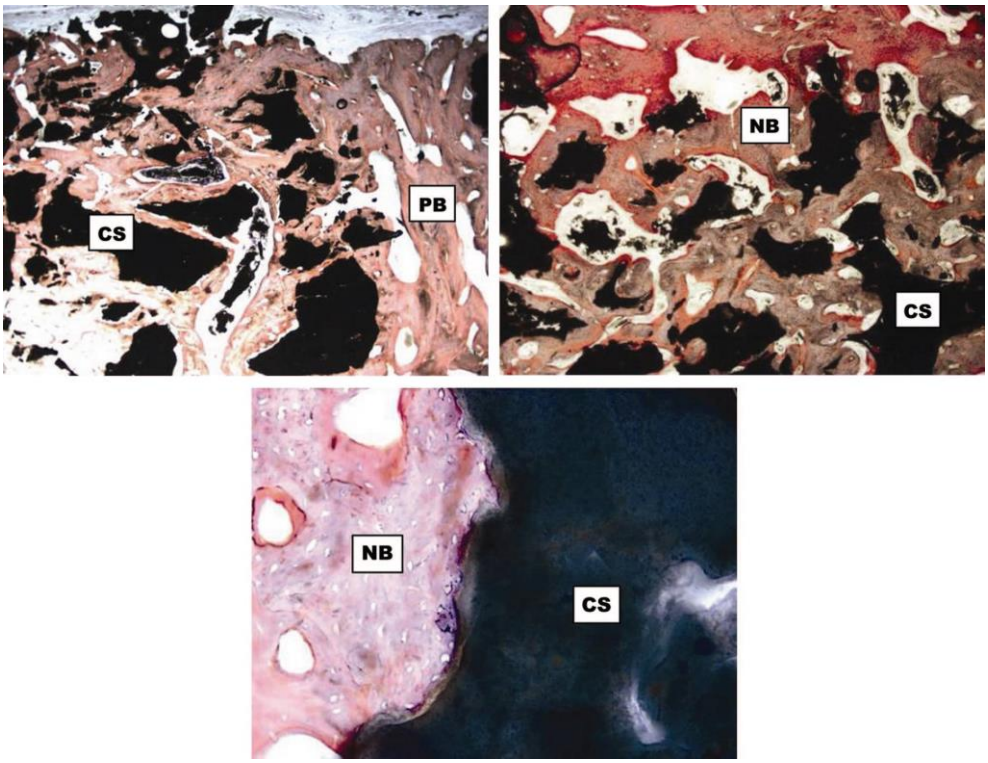

Figure 9.4 *– Light microscopic images of cranioplasty obtained 12 months postoperatively (toluidine blue, acid fuchsin, and chromoxane cyanine R staining; original magnification, X2). (Above, left) Cranial substitute in close contact with the peri-implant bone; cranial substitute and newly formed bone at 1.25X resolution (above, right) and 10X resolution (below). PB, peri-implant bone; CS, cranial substitute; NB, newly formed bone.*

Table 9.4 *– Data Obtained with Histomorphometric Analysis of the Materials 6 and 12 Months Postoperatively (Mean±SD).*

	Peri-Implant Bone		Implant	
Parameter	**Group A**	**Group B**	**Group A**	**Group B**
No.	5	5	5	5
BIC, %	49.8 ± 14.6	74.5 ± 8.7*	—	—
BV/TV, %	60.5 ± 12.2	53.0 ± 9.4	8.0 ± 3.8	37.3 ± 21.6*
NewBV/BV, %	45.8 ± 34.8	21.4 ± 18.1	94.6 ± 6.1	38.8 ± 13.0†
Tb.Th, μm	258 ± 66	262 ± 49	208 ± 9	489 ± 93†
Tb.N, mm^{-1}	4.0 ± 3.3	3.5 ± 1.4	9.4 ± 3.0	7.4 ± 1.8
Tb.Sp, μm	819 ± 325	798 ± 356	536 ± 296	407 ± 115
Mat.V/TV, %	—	—	54.7 ± 3.2	40.7 ± 4.5†
Fib.Tis.Th, μm	102 ± 18	77 ± 13*	—	—

BIC, bone-to-implant contact; BV/TV, trabecular bone volume; NewBV/BV, newly formed bone volume; Tb.Th, trabecular thickness; Tb.N, trabecular number; Tb.Sp, trabecular separation; Mat.V/TV, material volume; Fib.Tis.Th, thickness of fibrous tissue.
*$p < 0.05$ (t test).
†$p < 0.0005$ (t test).

9.3.4 Biomechanical test

The peri-implant bone hardness at 6 and 12 months was not affected negatively by the presence of the cranial substitute (Table 9.5). The newly formed bone at the bone-to-implant interface and in the bone implant areas did not show significant differences in the values of microhardness in comparison with normal host bone and in bone mineralization index at the two experimental times.

Parameter	No.	Host Bone	Bone-to-Implant Interface	New Bone			Material (HA)
				Region 1	Region 2	Region 3	
Microhardness, HV							
Group A	5	52.5 ± 1.4	52.1 ± 1.3	48.8 ± 3.0	63.5 ± 15.4	50.8 ± 5.5	133.9 ± 12.2
Group B	5	52.2 ± 1.1	49.1 ± 3.6	47.8 ± 3.7	49.5 ± 5.7	48.7 ± 2.9	127.3 ± 9.2
BMI, %							
Group A	5		0.99 ± 0.01	0.93 ± 0.06	1.18 ± 0.28	0.97 ± 0.08	
Group B	5		0.94 ± 0.09	0.91 ± 0.06	0.95 ± 0.10	0.93 ± 0.05	

HA, hydroxyapatite; HV, Vickers Hardness Index; BMI, Bone Mineralization Index.

Table 9.5 *– Data Obtained with Microhardness Analyses (Mean±SD).*

9.3.5 Micro-Computed Tomographic Evaluation

Significant differences were found for all parameters among prostheses before implantation and those at 6 and 12 months (Table 9.6), particularly for implanted prostheses in pore connection (12.0 percent), pore thickness (–18.3 percent), and pore separation (39.6 percent) at 6 months; and in porosity (43.6 percent), pore connection (10.4 percent), and pore separation (25.8 percent) at 12 months when compared with prostheses before implantation. Pore separation distribution values of the prostheses and within the implants at 6 and 12 months after surgery are shown in Figure 9.5.

	Implant				
Parameter	Material	Group A	Group B	ANOVA *F*	*p*
PoreV/TV, %	36.4 ± 4.1	41.6 ± 6.1	44.6 ± 4.1†	4.49	<0.005
Pore connection, %	87.5 ± 7.3	98.0 ± 1.1†	96.6 ± 2.1†	8.32	<0.0005
PoreTh, μm	699.9 ± 38.5	571.5 ± 77.5†	599.0 ± 103.6	4.89	<0.05
PoreSp, μm	723.1 ± 70.3	1009.6 ± 107.1†	909.5 ± 163.3†	9.45	<0.005

ANOVA, analysis of variance; PoreV/TV, porosity; PoreTh, pore thickness; PoreSp, pore separation.
*Mean ± SD ($n = 5$).
†Bonferroni post hoc t test ($p < 0.05$) versus material.

Table 9.6 – *Three-Dimensional Parameters of the Material before and after Implantation**

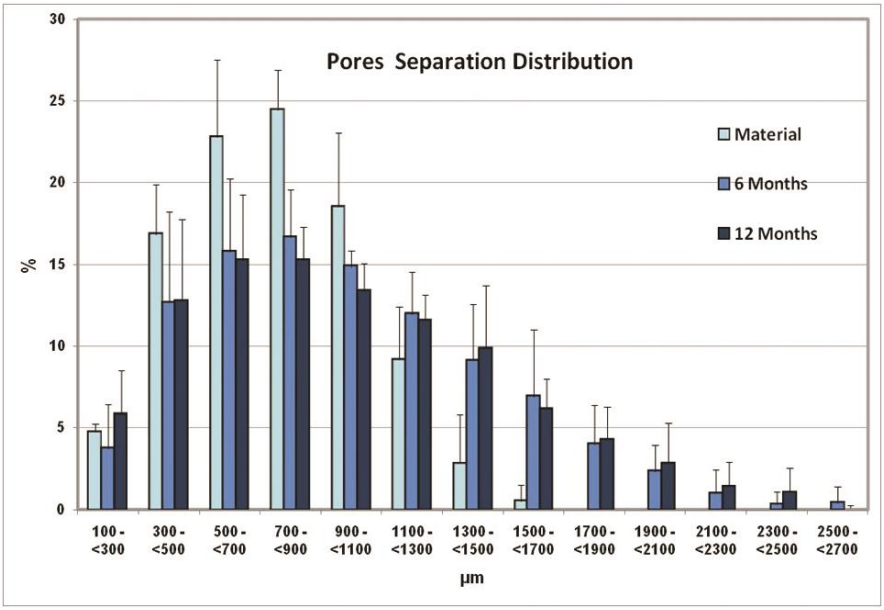

Figure 9.5 – *Graph of pore separation distribution within the bone cranial substitute at 6 and 12 months from the implant and within the material alone (mean ± SD).*

9.4 Discussion

Surgical removal of cranial bone and optimal reconstruction with a custom-made hydroxyapatite implant is a viable procedure that can be carried out in the same surgical setting to treat various cranial traumas, malformations, and diseases. No adverse events connected to the

prosthesis were reported in the current study and there was a total absence of interference in bone healing, thus supporting the findings of other studies on cranial reconstructive surgery [119-120]. Moreover, radiographic evaluation showed that the prosthesis held the correct position over time and its progressive osteointegration from the edges to the center, along with a progressive fragmentation and decreased density of ceramic structure.

Newly formed bone inside the prosthesis increased by over 300 percent between 6 and 12 months, corresponding to host bone architecture, as seen at 12 months by the increased thickness of the trabeculae and the decrease in newest bone volume. In some cases, the histologic observation of bone directly on the surface of the implant suggested that osteointegration might be the result of a combination of contact and distance osteogenesis, with both processes of bone apposition on the implant surface and bone approximating the implant surface [121-122]. At 12 months, no growing

phenomena or bone remodeling was observed, and there was also a significant reduction in material volume, indicating material resorption. Biomechanical evaluation showed that the cranial bone substitute does not cause changes in bone maturation and mineralization processes, and provides a newly formed bone tissue with the same mechanical strength as the host bone.

The results of the three-dimensional parameters did not show statistical differences between experimental times despite the significant increase in the bone formation shown by two-dimensional values (i.e., trabecular bone volume, newly formed bone volume). Besides porosity, the volume of interest shows two more factors that influence the measures performed: (1) the new bone that continues to grow and (2) the changes undergone by the material implanted. The further increase in new bone found at 12 months in the two-dimensional analysis might suggest a reduction in the porosity in the volume of interest, which may be explained by resorption of the material [108]. Therefore, the combined phenomenon of new bone formation and material resorption leads to invariability of the three-dimensional values.

The increase in porosity found at 12 months in comparison with the material before implantation may be explained by remodeling of the implanted material during the process of new bone formation or by its subsequent microfragmentation process. Concerning pore connection, the significant differences found in both experimental stages with respect to the material before implantation suggest a partial cracking of the material once implanted because of the mechanical load the implant undergoes or an initial degradation of the material.

The width of the pores (pore thickness) showed a significant reduction between the material before implantation and 6 months after implantation because of the start of new bone formation inside the pores, which leads to a change in the shape of the pores in the new bone/material/pore system. The fact that a predictable reduction in porosity is not found means that there is a compensation of the volumes caused by a degradation process of the material. The change in pore shape is explained by the significantly lower quantity of newly formed bone with respect to 12 months and that then starts to occupy portions of space in the pores in an uneven way. Material degradation, simultaneous with new bone formation, is more marked at 12 months, when a significant difference in the pore thickness value was not found in relation to the material before implantation. This suggests a growth in new bone degradation of the material inside the pores that is more even and widespread (Figure 9.6).

The increase in pore separation observed at both experimental times in comparison with material before implantation further explains the new bone formation in addition to widespread and constant material resorption (Figure 9.7). The distribution graph of the pore separation shows a similar trend and values between the two experimental times and an increase in the smaller separations at the expense of the larger ones, which are less or even not present at all, in the material before implantation. Considering that, between the material before implantation and that implanted at 6 and 12 months, there is an increase in the larger separations between the pores in the volume of interest, the presence of newly formed bone can be inferred. In fact, new bone

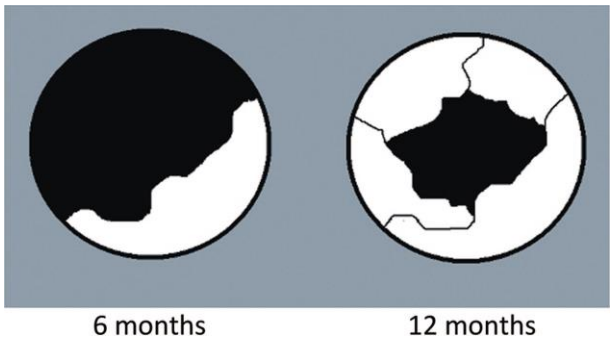

Figure 9.6 *– Drawings of new bone/material/pore system of custommade prosthesis (gray, material; white, new bone; black, pore): the growth of new bone spread nonuniformly inside the pores produces a three-dimensional pore thickness reduction.*

formation inside the porosities of the material occupies space, thus increasing the separation between the porosities at the two experimental times with respect to the porosity present in the material before implantation. The matching trend and the maintenance of the percentage distribution values between 6 and 12 months compared with the two-dimensional results, where both material resorption and new bone formation can be noted, is an indication of the simultaneousness of the two processes described.

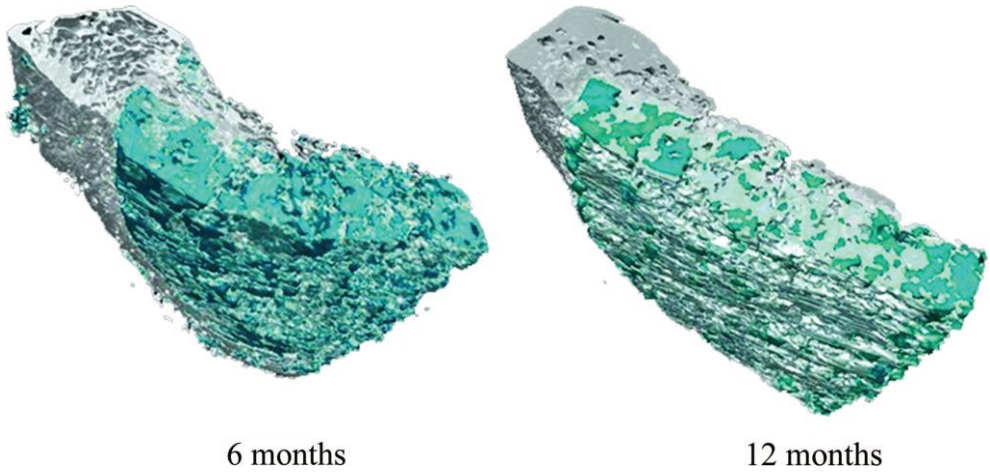

Figure 9.7 *– Three-dimensional virtual models of right posterior quadrants at 6 (left) and 12 (right) months (gray, new bone; green, cranial substitute material).*

This synchronous trend between material resorption and new bone formation is an important finding because this type of measure and analysis which, given the high resolution, cannot be performed in the clinical field, further corroborates the clinical success and explains the biological mechanism of this type of prosthesis. Regarding the animal model used, bone defect healing processes have been widely reported in the literature in different animal species and related to human beings [123-126]. The sheep is a representative animal model, extensively accepted for orthopedics [127] and maxillofacial surgery [101, 123, 128-129], with bone dimensions similar to those of humans. In this study, the defect was a critical-size defect for sheep skull that does not undergo spontaneous bony regeneration, as reported in the literature [101, 108, 130]. The experimental times were chosen according to the literature data regarding experimental and clinical experience with hydroxyapatite devices for cranioplasty [131-132].

No control materials were used because, to our knowledge, no other ceramic biomaterials are at present used clinically and are considered as the criterion standard for cranioplasty. The use of autologous bone grafts, which represent the criterion standard material in cranioplasty [133-135], was excluded for ethical reasons. This control group would have entailed removing the braincase from the animal, decellularization treatment and sterilization of the bone segment, and subsequent revision, thus leaving the animal for a period without repair of the skullcap or with the application of another type of device (i.e., titanium), thus increasing the risks connected to dual surgical procedures and further damage to the skullcap when removing any temporary device.

9.5 Summary

The current study showed rapid bone formation and mineralization inside the prosthesis, and the absence of chronic inflammation and

foreign body reaction through direct comparison between two-dimensional and three-dimensional analyses. The preclinical model gave insight into direct effects of hydroxyapatite on a biological *in vivo* process involved in bone healing and dynamic interactions between biomaterial and bone that would otherwise be difficult or impossible to obtain from in vitro models or clinical cases. The cranial prosthesis showed superior features concerning the reconstruction of cranial defects because of the ease of application, lack of chronic inflammation, and osteointegrative and osteoconductive ability when placed in contact with bone. Finally, the strength of the study was the ability to overcome the limitations of using two-dimensional analysis, where the histologic sections are a two-dimensional sector of a three-dimensional structure. Clearly, in a structure as complex as bone, micro–computed tomography provides a distinct advantage over conventional microscopy by allowing a more complete vision of the organization and structure of the sample.

ACKNOWLEDGMENTS

This work was supported by Rete Nazionale di Ricerca TISSUENET no. RBPR05RSM2. The authors thank Laura Dolcini for technical assistance and prosthesis manufacturing; Codman Italy, a Johnson&Johnson Medical Division, for technical support; and Keith Smith for assistance in language supervision.

Chapter 10
Histological, histomorphometric and microtomographic analyses of retrieval hip resurfacing arthroplasty failed at different times [136]

Open Access article in BMC Musculoskeletal Disorders 2013

Francesca Salamanna[1], Milena Fini[1,2], Annapaola Parrilli[1], Matteo Cadossi[3], Nicolò Nicoli Aldini[1,2], Gianluca Giavaresi[1,2], Deianira Luciani[3], Sandro Giannini[3]

[1] Biocompatibility, Technological Innovations and Advanced Therapies Laboratory (BITTA), Rizzoli RIT Department, Rizzoli Orthopaedic Institute, , Italy
[2] Laboratory of Preclinical and Surgical Studies, Rizzoli Orthopaedic Institute, , Bologna, Italy
[3] II Orthopaedic and Traumatology Clinic, Rizzoli Orthopaedic Institute, Bologna, Italy.

ABSTRACT

Background: Metal-on-metal hip resurfacing arthroplasty (HR) has been gaining popularity especially for young and active patients. Although different series report good mid-term results, the long-term outcome and failure mechanisms are still concerning. In this consecutive revision case series, 9 retrieved specimens of a failed Birmingham Hip Resurfacing (BHR) were divided according to the time to fracture: 3 specimens failed at less than 6 months (Group 1), 3 failed between 6 months and 3 years (Group 2) and 3 failed later than 3 years (Group 3). The objective of the study was to examine by a specific quantitative histomorphometry and microtomography (micro-CT) method the characteristics of bone quality and its microarchitecture in retrieved metal-on-metal HR.

Methods: A series of 948 BHR were performed between 2001 and 2009. Among these implants 10 failures occurred and nine of these underwent revision surgery and were examined by histomorphometry and micro-CT.

Results: Histomorphometry showed a significant increase in trabecular separation (Tb.Sp) in Group 3 in comparison with Group 1 (113%, $p < 0.05$). In the top region, micro-CT showed that Groups 2 and 3 presented significant lower bone volume (Group 2: 61%, $p < 0.005$; Group 3: 1%, $p < 0.05$), trabecular number (Group 2: 53%, $p < 0.005$; Group 3: 40%, $p < 0.05$), and higher Tb.Sp (Group: 71%,$p < 0.05$) when compared to Group 1. Additionally, histomorphometry showed that the top regions in Group 1 had a significantly lower mean percentage of empty osteocyte lacunae than the top regions in both Group 2 and 3 ($p<0.05$).

Conclusions: This study showed that the morphometric parameters considered are crucial for a good understanding of mechanical properties of HR and may be of significant importance in the pathogenesis of HR failure particularly in the development of late fractures.

Keywords: Hip resurfacing arthroplasty, Failure, Histomorphometry, Microtomography

10.1 Background

Joint replacement is continuously evolving to reduce the invasiveness of surgery, prolong the implant life, decrease complications and improve the patient's life quality. Resurfacing hip arthroplasty is emerging as an alternative to conventional total hip arthroplasty and has been proposed as an option for the treatment of degenerative hip disease in young, active individuals [137]. HR may present benefits over total hip replacement because femoral bone stock is maintained, there is reduced wear compared with high density polyethylene, it has a large femoral head that could be reduced dislocation rate, it is said to offer the patient increased levels of postoperative activity and is easy to convert into a stemmed prosthesis [138]. The general opinion about this procedure is mainly divided into a favorable one advocated by McMinn et al. [139] and negative one supported by Spierings et al. [140]. The mid-term results of Birmingham Hip Resurfacing (BHR) suggest a survival rate of about 98% at five years. However, Spierings et al. still consider resurfacing as an experimental design for investigational use only, until long-term follow up confirms its superiority in comparison with total hip replacement [139-140]. Recently various complications, such as femoral neck fracture [141-143], avascular necrosis [144-145] and pseudotumour formation [146-147], as well as unexplained pain, aseptic loosening [148], and osteolysis [140] have been reported. To improve the technique and the success of the treatment, experimental preclinical models can be used to allow the evaluation of biomechanics, biocompatibility, bioactivity and biofunctionality on innovative biomaterials, prosthetic devices and combined therapies. Nevertheless, the retrieval of failed prostheses and the analysis of human implanted devices is one of the most valuable tools to provide information about prostheses that have been submitted to clinical loading and biological and chemical micro-environment during their stay in the body [149]. Indeed, analysis of retrievals can show the histopathological response and the mechanisms of failure [150]. Currently, radiology and histology are the most common procedures to

study failed bone implants and some authors have used these techniques to evaluate bone necrosis and fracture risk [142,146,151-154]. Although it is clear that we require a better understanding of the failure mechanisms of the current generation of metal-on metal HR implants, no studies have ever used histomorphometric and microtomographic evaluation to evaluate the characteristics of bone quality and its microarchitecture in retrieved metal-on-metal HR. In fact, from a literature search of the entire MEDLINE database (PubMed research engine) using the MeSH database terms ("hip arthroplasty" [Mesh] OR "hip resurfacing" [Mesh]) AND ("histomorphometric evaluations" [Mesh] OR "x ray microtomography" [Mesh]) no studies were found. Histomorphometry provides information regarding bone tissue and cell dynamics. Similarly, a microtomographic evaluation of the bone structure gives a real estimate of its morphology, especially when it is carried out directly on the entire volume without using predefined volumetric models (plate or rod-model) [155]. Moreover, good correlations were found between the structural parameters determined by microtomography (μCT) images and those assessed on histomorphological slices [156].

Therefore, the main goal of this study was to analyze and examine the characteristics of bone quality and its microarchitecture in retrieved metal-on-metal BHR by a new and specific quantitative histomorphometry and μCT method, never used before. This novel and innovative technique was performed to evaluate whether these 2D and 3D quantitative measurements might be applied to this field of research and give further insight into the failure mechanisms of these implants. This methodology was applied to a small consecutive revision case series taking into account different times to fracture and bone areas located at different distances from the HR dome.

10.2 Methods

10.2.1 Patient cohort

This is a retrospective observational study in which the protocol was explained to the patients and they gave written informed consent before entering the study (Determination of 20 March 2008, Italian Medicines Agency – AIFA).

A series of 948 (373 female and 575 male) HR (Birmingham Hip Resurfacing, Midland Medical Technologies Ltd, Birmingham, UK: now Smith&Nephew) was performed in our ward at Rizzoli Orthopaedic Institute between early 2001 and late 2009 of whom 941 patients were available for follow-up. Among these implants 10 fractures occurred. Nine of these fractures underwent revision surgery at the Rizzoli Institute and they constitute the series of this study. All these patients underwent HR for primary arthritis of the hip through a posterolateral approach. The patients' characteristics of failed HR are reported in Table 10.1.

Fractures were divided into three groups:

- Gross fractures that occurred soon after surgery, earlier than 6 months (Group 1) which presented a pattern involving the implant rim. These fractures were characterized by diffuse reactive changes and varying degrees of perfusion of the proximal bone depending on the vascular injury. It was hypothesized that these aspects may be related to the surgical technique leading to biomechanical changes in the femoral neck by the notch (acute biomechanical fractures);

- Fractures that occurred between 6 months and 3 years (Group 2) and fractures that occurred later than 3 years (Group 3) were defined as late fractures, completely inside the femoral head, with extensive evidence of osteonecrosis. These two groups were divided arbitrarily to highlight the possible presence of a phenomenon that progresses with time. Macroscopically, in each group, necrotic bone tissue appeared pale and white-yellowish with scattered calcifications. One patient of Group 2

experienced a pseudotumor of ileopsoas with an aseptic lymphocytic vasculitis-associated lesions (ALVAL) at 3 years follow up. The acetabular inclination angle was 67°, thus suggesting the presence of edge wear. Metallic debris was evident macroscopically. All patients of Group 3 presented evident macroscopic signs of metallosis without soft tissue involvement, suggesting that osteonecrosis might be also developed by metal corrosion phenomena.

Group	Time to Revision	Age/Gender	Implant	Notching	Cup inclination	Stem Neck angle	Side
Group 1	3 weeks	70/M	46- mm head –52-mm cup	Present	54°	7°	Left
	2 month	60/F	46-mm head, 52-mm cup	Present	52°	0°	Right
	5 month	50/F	44- mm head –50-mm cup	Present	47°	6°	Right
Group 2	14 month	69/F	42- mm head –52-mm cup	Absent	45°	0°	Right
	36 month	47/F	46- mm head –52-mm cup	Absent	46°	0°	Right
	36 month	44/F	42–mm head-48-mm cup	Absent	67°	1°	Right
Group 3	4 years	53/M	50- mm head –56-mm cup	Absent	52°	3°	Left
	7 years	50/F	42- mm head –48-mm cup	Absent	60°	4°	Left
	8 years	51/F	46- mm head –52-mm cup	Absent	54°	10°	Left

Table 10.1 *– Summary of the cases: patients gender and age (at the time of the primary operation) implant sizes, operation site, time to revision (F: female; M: male).*

10.2.2 Surgery

With the patient well secured in the lateral position and under general or spinal anesthesia an extended posterior approach to the hip joint was used in a clean-air operating theatre. The short external rotators were released, the gluteus maximus was detached from its insertion at the linea aspera, and a circumferential capsulotomy was performed. The femoral head was dislocated anteriorly and the acetabulum reamed sequentially. Peripheral acetabular osteophytes were excised and a trial component which was 1 mm smaller than the intended final implant was used to confirm that a tight fit had been obtained. If this fixation was satisfactory, the definitive acetabular component was then impacted. Standard instrumentation was used to align and position the guide rod for the preparation of the femoral head using the lateral cortical pin and out-rigger. The head was reamed to house a femoral component that matched the implanted acetabular component. The femoral implant was

positioned and secured with Simplex (Howmedica International, Limerick, Ireland) low viscosity cement. The hip was then reduced and the short external rotators and gluteus maximus tendon repaired.

10.2.3 Histological and histomorphometric analyses

At revision, the femoral component together with the femoral head and neck bone was resected en bloc and immediately placed in buffered 4% paraformaldehyde. No acetabular components were removed. After fixation, the bone-metal composite specimens were dehydrated by placing them in graded series of increasing percentage of alcohol with one step in 50% alcohol, one step in 75% alcohol, two steps in 95% alcohol, and two steps in 100% alcohol, for 48 hrs per each step. After dehydration, the undecalcified specimens were infiltrated by exposing them to methyl methacrylate solution (Merck, Germany). The infiltration was completed with use of methyl methacrylate combined with benzoyl peroxide (Sigma-Aldrich) and poly-methyl-methacrylate (PMMA) (Sigma-Aldrich) under vacuum condition for four days. The different steps of the study are summarized in Figure 10.1. The embedded specimens were cut in middle along the coronal plane by a saw with a diamond-coated band (EXAKT, GmbH & Co., Norderstedt, Germany). The orientation of the specimens during the cutting process was preserved, thus maintaining a low feed force coupled with the automatic control of the cutting band. One section of about 0.5 cm thick and two sections of 350 ± 100 μm thick were obtained for each HR sample. The implanted device was removed from the first section and the section was analyzed by μCT as described below. Then, it was automatically thinned (EXAKT Systems) to 15 ± 5 μm with different abrasive papers (EXAKT Abrasive Disc), from 80 to 2000 grit in steps of 15 minutes each and used for histomorphometric measurements. By the same procedure the other two sections of HR retrieved were automatically thinned to 60 ± 10 μm and used to measure the contact

between bone and prosthetic stem. Next, the sections were stained with Toluidine Blue, Acid Fuchsin, Fast Green, and processed for routine histological analyses. Histological analyses were performed by using a transmission and polarized light AxioSkop Microscope (Carl Zeiss GmbH, Germany) at a magnification from 1.25x to 20x. After prosthesis removal, two different compartments of the femoral head were considered: A lateral and B medial. Each compartment was split into 3 regions of interest (ROI) depending on the distance from the HR dome: within 0.8 cm (top), from 0.8 to 1.6 cm (central) and from 1.6 to 2.4 cm (bottom). Finally, histomorphometric analyses were carried out with computerized image analysis Axio-Vision-4.6 (Carl Zeiss). Bone histomorphometry measurements were taken semi-automatically at a magnification of 1.25x by two experienced blinded investigators, by dividing the sections of compartments A and B into different quadrants. The bone-to-implant-contact (BIC) was measured at the interface between bone and prosthesis stem as the rate between the stem surface directly in contact with bone without the interposition of fibrous tissue/the total interface length x 100 (%). The bone histomorphometric parameters were measured in accordance with the Histomorphometry Nomenclature by the Committee of the American Society for Bone and Mineral Research [157]:

- Bone Volume (BV/TV,%): the whole spongy bone area, expressed as a percentage of the total tissue area in the sampling site and converted to a volume;
- Trabecular Number (Tb.N, mm-1): index of density of trabeculae;
- Trabecular Thickness (Tb.Th, μm): index of the width of trabeculae;
- Trabecular Separation (Tb.Sp, μm): index of the distance of trabeculae;
- Cement Thickness (Cm.Th): index of the width of the cement on the dome surface.

For each sample, the mean percentage of empty lacunae in five regions of interest in the top, central and bottom part, at a magnification of 20x, was determined by two experienced blinded investigators using the method of Steffen et al. [158].

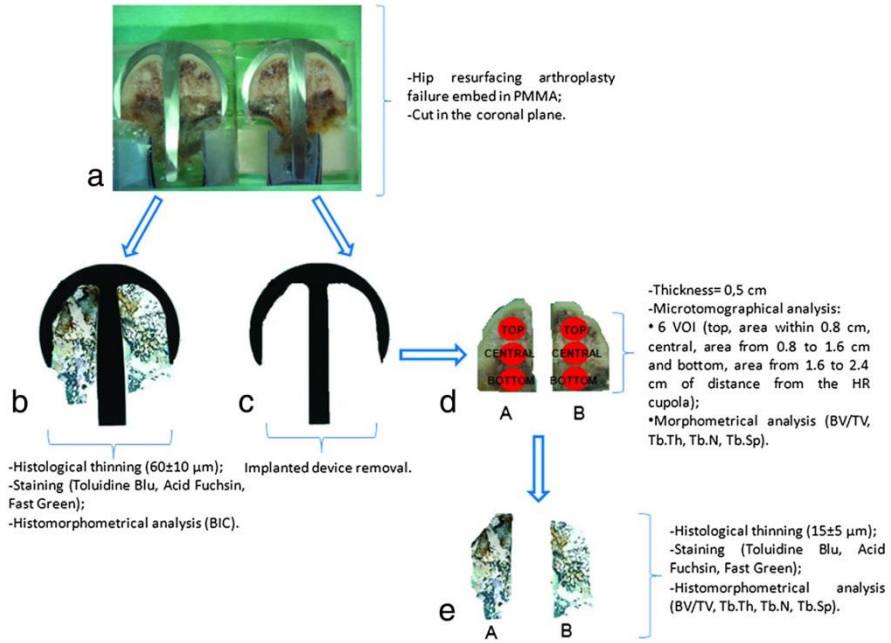

Figure 10.1 *– Schematic representation of the methodology for sample analyses. Epson 2480 Scanner, 600dpi of resolution. a) The specimens were embedded in PMMA and cut along the coronal plane, b) sections containing the implants were used for histology and histomorphometric measurement (BIC), c) after the removal of the prosthesis, d) two bone compartments (A and B) were used for µCT, e) thinned and processed for routine histological and histomorphometric analyses.*

10.2.4 Microtomographic analysis

As shown in Figure 1, µCT assessment was carried out on a 0.5-cm-thick embedded section of the samples using the Skyscan 1172 computed microtomographic system (Kontich, Belgium). The scans were performed with a 100 kV voltage source and 100 µA current source. Images were acquired with a pixel size of 12 µm, an aluminum filter 0.5 mm, and a sample rotation step of 180° and 0.4°. The scans were later reconstructed to obtain microtomographic sections. Reconstruction was performed by using NRecon (v1.6.2.0) software: a specific alignment was used for each sample and a medium intensity ring artifact correction was applied. Microtomographic 3D analyses were performed using CTAn (v.1.10.1.3)

software and, as for histologic evaluation, considering 3 Volumes of interest (VOI) in each compartment (A and B): at the top, within 0.8 cm from the HR dome, in the centre, from 0.8 to 1.6 cm from the HR dome, and at the bottom, 1.6 to 2.4 cm from the HR dome. The morphometric parameters considered were derived in part from those already defined by Parfitt [157]:

- Bone volume density (BV/TV,%), expressed as a ratio between the volume of bone measured in the VOI and the total volume of the considered VOI;
- Trabecular thickness (TbTh, μm) measured as a true model-independent 3D value;
- Trabecular separation (TbSp, μm), derived from the volume-based local thickness just applying the method to the space between trabeculae;
- Trabecular number (TbN,mm-1), defined as: 1/(TbTh + TbSp).

10.2.5 Statistical analysis

Statistical analysis was performed by using the SPSS Inc v.12 software. Data were reported as Mean ± SD at a significant level of $p<0.05$. After checking normal distribution (Shapiro-Wilks test) and homogeneity of variance (Levene test), the non-parametric Kruskall-Wallis test followed by Mann–Whitney test with Monte Carlo methods to compute probability were carried out to compare histomorphometric results among groups.

10.3 Results

10.3.1 Histological results

Group 1

The mean time-to-revision was 10.3 ± 8.7 weeks. No difference was found by histological analysis in this group (Figure 10.2). A thin layer of cement was present at the bone-dome interface and intraosseous cement penetration was recognized by its hard consistency, fine granular structure, and color in the top regions. Focal areas of osteonecrosis with trabecular lamellar bone with empty lacunae were observed in the central and bottom regions (Figure 10.2a,b). In the bone areas adjacent to the HR dome (top ROI) normal bone microarchitecture and morphology with osteocyte nuclei in the lacunae were observed (Figure 10.2a). In the 5-month case the areas of focal osteonecrosis with bone trabeculae without stainable osteocytes were associated with signs of appositional new bone formation.

Group 2

The mean time–to-revision was 28.6 ± 12.7 months. No differences were observed among the 3 analyzed prostheses that had failed from 14 to 36 months (Figure 10.2c,d). A cement mantle was present at the dome and intraosseous cement penetration was observed in the top region and in a small part of the central region. An absence of osteocyte nuclei within bone lacunae was observed in all cases in all ROIs. Thickened cancellous bone trabeculae were sometimes observed with extensive formation of appositional new bone on the surface of necrotic trabeculae (Figure 10.2c). Signs of metallosis with infiltration and accumulation of metallic wear debris inside the periprosthetic structures were clearly visible in the two patients that failed at longer follow up times (Figure 10.2d). At 36 months a considerable amount of connective tissue was observed.

Group 3

The mean time-to-revision was 6.3 ± 2.1 years. Sectioning of the implant revealed a thin layer of cement at the dome and a penetration of cement deep into the bone was observed in the top and central region. Femoral head section analyses showed a decrease in bone mass with partial necrosis in each examined sample. Histological examination confirmed the presence of a massive metallosis revealing granulomatous tissue with extensive pigmented deposits in all examined cases, which was more evident at 7 and 8 years with bone rarefaction present in all ROIs of the femoral head (Figure 10.2e,f).

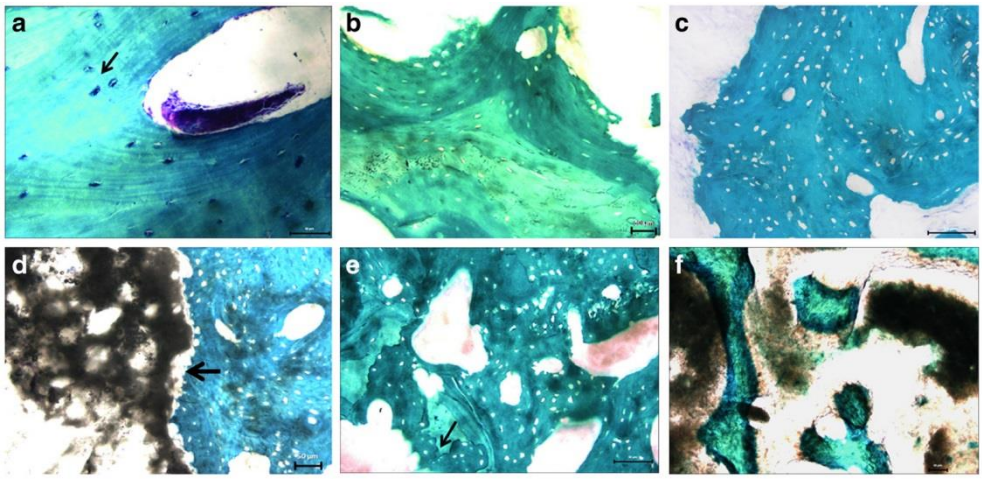

Figure 10.2 *– Histology of specimens revised in Group 1 (a, b), Group 2 (c, d) and Group 3 (e, f); sections are representative of bone tissue at increasing distances from the HR dome: within 0.8 cm (top) (a, c, e), from 1.6 to 2.4 cm (b, d, f) (bottom). Toluidine Blue, Acid Fuchsin, Fast Green staining. a) trabecular lamellar bone with evident evenly spread osteocytes, orientated with the longest axis in the direction of the lamellae contained in the bone lacunae (arrows), resolution 20x; b) necrotic bone tissue, resolution 10x; c) necrotic tissue, resolution 20x; d) necrotic bone tissue infiltrated with aggregates of small dark metal wear-debris particles (metallosis) (arrows), resolution 10x; e) loss of normal trabecular bone microarchitecture, uneven edges due to the resorption of necrotic bone (arrows) resolution 20x; f) metallosis in close association with the necrotic bone trabeculae, resolution 10x.*

10.3.2 Histomorphometric results

The 2D histomorphometric tests were performed on the sections where the implanted device was present for BIC and Cm.Th measurement and in those where the HR had been removed for BV/TV, Tb.Th, Tb.N, Tb.Sp and percentage of empty lacunae measurements. The results of histomorphometric parameters are reported in Figure 10.3a and b. The Kruskal-Wallis test highlighted statistically significant differences between groups for BIC (p=0.004). The Mann–Whitney test showed that Group 3 presented statistically significantly lower BIC values (71%, p=0.004) when compared to those of Group 1. The results of the percentage of empty lacunae obtained from each separate ROI (top, middle and bottom) are summarized in Figure 10.3b. Statistically significant differences were found for empty lacunae in Group 1 (p=0.05) between the top region and the others. Additionally, the top regions in Group 1 had a significantly lower mean percentage of empty osteocyte lacunae than top regions in both Group 2 and Group 3 (p=0.05).

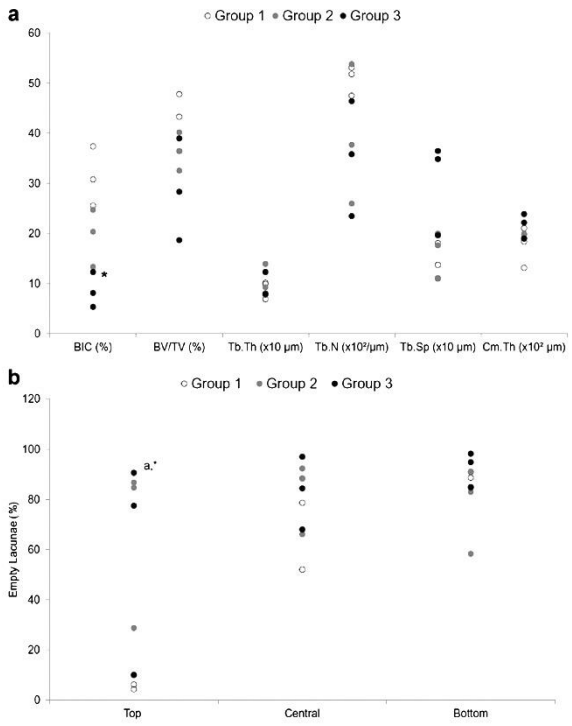

Figure 10.3 *– Dot plot of (a) histomorphometric parameters and (b) percentage of empty osteocyte lacunae in the different ROIs (top, central, bottom) for each Group. Mann Whitney test: (a) Group 3 versus Group 1 (*, p<0.05); (b) a, Top region versus central and bottom regions (p<0.05).*

10.3.3 Microtomographic results

The 3D microtomographic analysis was carried out on the sections after the removal of the implanted device. The results of μCT parameters for each patient are reported in Figure 10.4. Data are in parallel with those of histomorphometric results and showed that bone rarefaction (as measured by BV/TV, Tb.N, Tb.Sp) progressively changes over time (Figure 10.5a,b). The comparison between Group 1 and Group 3 showed that BV/TV and Tb.N decreased by about 28% and 37%, respectively, whereas Tb.Sp increased by about 37%, but the differences did not reach statistical significance. Microtomographic data obtained from each separate ROI (top, middle and bottom) are reported in Figure 10.6a-d. Statistically significant differences between Groups in the top ROI were found for BV/TV (p=0.025), Tb.N (p=0.025) and Tb.Sp (p=0.028). In the top ROI, the Mann–Whitney test showed that Group 2 and Group 3 presented significantly lower BV/TV (Group 2: 61%, p=0.05; Group 3: 41%, p=0.05) and Tb.N (Group 2: 53%, p=0.05; Group 3: 40%, p=0.05), and higher Tb.Sp (Group 3: 71%, p=0.05) when compared to those of Group 1.

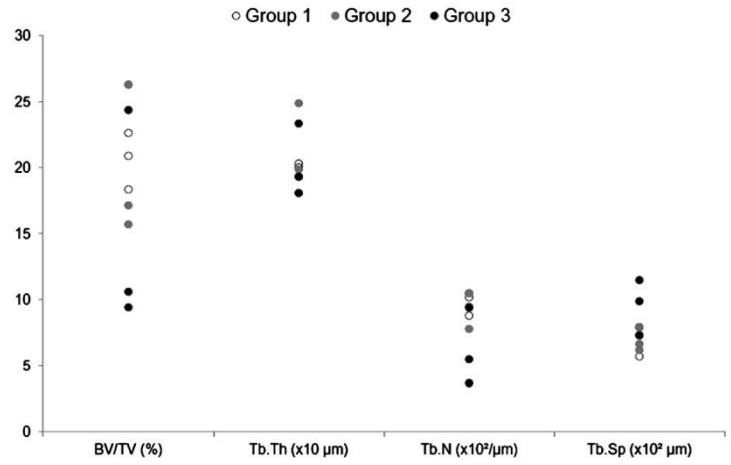

Figure 10.4 *– Dot plot of microtomographic analysis for each Group.*

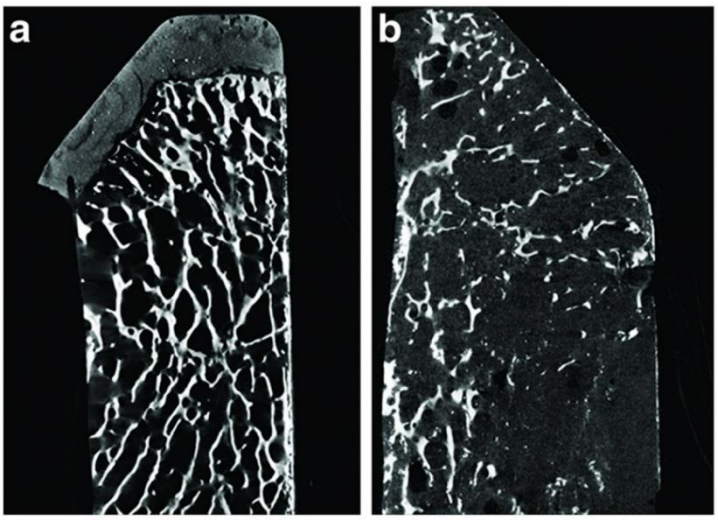

Figure 10.5 *– Microtomographic sections of HR failure after prostheses removal. a) Group 1 (5 months); b) Group 3 (7 years) showing an important bone rarefaction.*

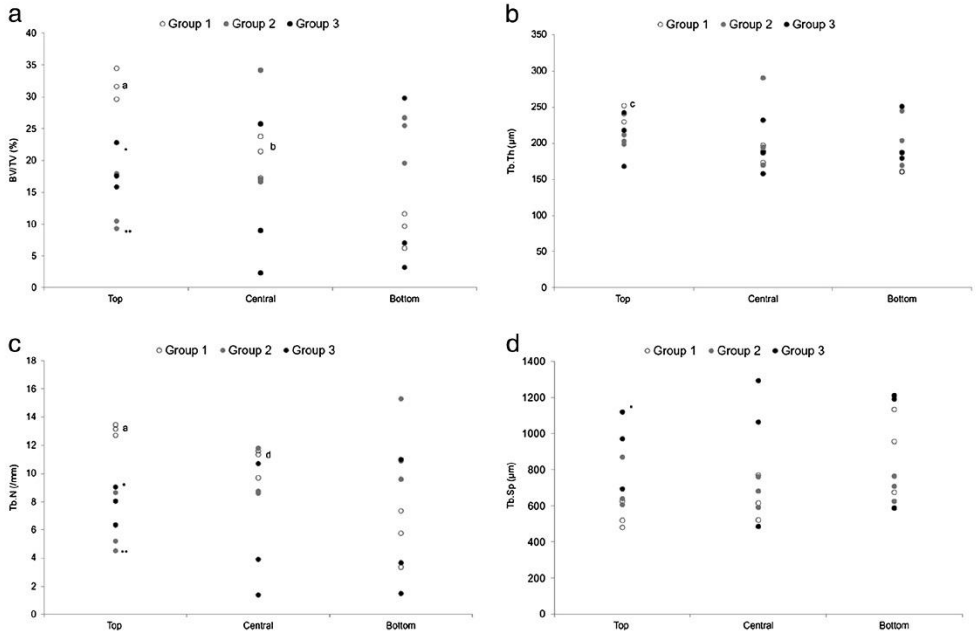

Figure 10.6 *– Dot plot of microtomographic data split into the different ROIs (top, central, bottom) (a) BV/TV; (b) Tb.Th; (c) Tb.N; (d) Tb.Sp. Mann–Whitney test: - comparison between terms: medium Group 2 and long-term Group 3 groups versus short term group Group 1 (*, p<0.05; **, p<0.005); -a, Top region versus bottom region(p<0.005); b, Central region versus top and bottom regions (p<0.05); c, Top region versus central and bottom regions (p<0.05); d, Central region versus bottom region (p<0.05).*

10.4 Discussion

The main goal of this study was to evaluate the characteristics of bone quality and its microarchitecture in a series of femoral heads that failed at different times for different reasons by adopting an innovative and specific quantitative histomorphometry and μCT methodology. To do this nine failures were considered, which were split into groups depending on the failure time: 3 specimens failed at less than 6 months (Group 1), 3 failed between 6 months and 3 years (Group 2) and 3 failed at more than 3 years (Group 3) after HR surgery. In comparison with other studies, in this one the Groups were divided arbitrarily to highlight the possible presence of a phenomenon that progresses over time.

Histological evaluation showed the presence of focal areas of osteonecrosis with empty lacunae in the Group 1. In Group 2 and Group 3 partial osteonecrosis also was present; nevertheless, newly formed bone was visible on the surface of the necrotic bone trabeculae. These data were in agreement with those of Steffen et al. who showed that the necrotic changes were associated with appositional new bone formation and marrow fibrosis [150]. In fact, proliferating cells spread through the narrow spaces between the dead trabeculae, differentiate into osteoblast, and subsequently form appositional new bone on the surface of dead trabeculae. At the same time, they initiate osteoclastic resorption of necrotic bone. Osteoclastic resorption, modulated by cytokines released from osteoblast, is crucial for the balance of the repair processes. The bone may be markedly weakened if resorption occurs at the interface of the viable and dead bone, or if revascularization and new bone formation in necrotic areas is prevented by the formation of a fibrous scar [158]. Bone atrophy was observed at histological analyses only in Groups 2 and 3 and these results were confirmed by micro-CT (BV/TV, Tb.N, Tb.Sp) thus suggesting a possible role of mechanical factors (stress shielding). Metallosis, with infiltration and accumulation of metallic wear debris, was visible in Group 2 and 3. Therefore, as shown by other authors who studied the failure mechanism of HR prostheses by conventional

radiography and qualitative histology, the present histological analyses confirmed that aseptic necrosis and bone rarefaction might play a crucial role in late failures of HR [142, 150-151,153, 159-161].

Unlike previous studies, the present one took into consideration 3 groups of patients according to failure times (from 3 weeks to 8 years); quantitative measurements were performed with histomorphometry and μCT and 3 peri-implant bone regions at different distances from the HR dome (within 0.8 cm (top), from 0.8 to 1.6 cm (central) and from 1.6 to 2.4 cm (bottom)) were considered. This was possible through resin embedding of the femoral heads containing the prostheses, cutting along the coronal plane of the macro-sections and subsequent removal by pressure of the prosthesis that permitted the accurate evaluation of bone histology and microarchitecture with both 2D (histomorphometry) and 3D (μCT) techniques. A different bone architecture was highlighted within each group and, in particular, between the Group 1 and Group 3. Both 2D and 3D measurements showed that bone density decreases over time especially in Group 3 if compared with Group 2 and Group 1. 3D data of different ROIs (top, central, bottom) of both lateral and medial compartments showed a significant decrease in bone quality over time in the top ROI near the dome. This was confirmed by the significant differences in BV/TV, Tb.N and Tb.Sp between Group 1 versus Group 2 and Group 3 in the top ROI. This tendency was visible also in the lower ROIs but bone values did not reach statistical significance.

In the present study bone resorption was observed within the resurfaced femoral head and around the proximal part of the stem. Whereas bone remodeling is a feature of normal metabolism in healthy and osteoarthritic bone, the BHR may result in stress shielding with consequent resorption and narrowing of the femoral neck due to altered loading conditions. This stress shielding is probably due to the implant design with long-stems. In fact, Bidyut Pal and coworkers showed that bone resorption was considerably less for short-stem designs; the short-stem design having stem-bone contact not only led to a more physiological stress distribution but also to bone apposition in the superior side of the resurfaced head [162]. Moreover, 2D results showed

significant differences also in the percentage of empty lacunae between Group 1 versus Group 2 and Group 3 in the top ROI. The proportion of empty lacunae gradually increased over the time after surgery.

The present results were in agreement with those of Steffen et al. who showed that samples from late fractures had a significantly higher proportion (84%) of empty osteocyte lacunae within the trabecular bone compared with those of samples from fractures occurring within the first month (48%) after HR [150]. Moreover, in the present study the higher mean percentage of empty lacunae in the central and bottom regions of Group 1 was probably due to a vascular injury. This controversial result might be explained by analyzing the surgical technique. During femoral head preparation the top region is always removed, thus eliminating the bone volume more subjected to osteonecrosis. Moreover, the residual blood supplied comes from the lateral femoral circumflex artery and a recent report [163] shows two more possible sources of blood supply to the femoral head. These two vessels were identified as the anterior nutrient artery of the femoral neck which origins from the lateral femoral circumflex artery and the inferior branch of the deep branch of the superior gluteal artery.

In the present series all the operations were performed through a posterior approach which is known to disrupt the medial circumflex artery; nevertheless, the failure rate due to bone necrosis was low. Similar findings were observed by Mcbride et al. who reported the same implant survival regardless of surgical approach [164]. By using a surgical approach that preserves the blood supply it might be possible to obtain an improved implant survival at longer follow up [150,155,165].

The BIC measurement should not be considered as an index of osteointegration because the surgical procedure of HR insertion is not aimed at achieving primary fixation between the bone and the stem as for traditional arthroplasties. However, a progressive decrease of bone in contact around the stem was observed and the difference was significant between Group 1 and Group 3 patients. The decrease in BIC was probably due to the bone rarefaction, which involves the femoral head; it remains to be seen whether it might also be related to a progressive

prosthesis loosening over time. In the present study histological and microtomographic analyses suggest that both processes, bone rarefaction and osteonecrosis, start from the bottom of the peri-implant bone and reach the top region adjacent to the HR dome in the Group 2 and 3. Osteonecrosis is expected to start from the top ROI which is far away from blood vessels and probably more influenced by the presence of cement but the findings in the present study showed the contrary. In fact, some sort of stress shielding due to its close relationship with the implant might be the true reason for this particular finding.

The current study has several limitations. First of all the small number of cases prevents any solid conclusions to be drawn about the real failure mechanisms of HR and the progression of femoral head damage. The inter-individual variability between patients and osseous changes should also be taken into account. Nevertheless, it was not the primary objective of this study to define the pathophysiology of HR prosthesis failure. To the present authors' knowledge, quantitative methodologies for measuring bone quality and its microarchitecture have never been used to study retrieved HR prostheses. In the present study the histomorphometric and microtomographicevaluations allowed bone microarchitecture alterations to be quantified.

10.5 Conclusions

The objective of the study was to examine the characteristics of bone quality and its microarchitecture in retrieved metal-on-metal HR by a specific quantitative histomorphometry and μCT method. The results showed that the morphometric parameters considered were crucial for a good understanding of the mechanical properties of HR and may be of significant and essential importance in the pathogenesis of HR failure particularly in the development of late fractures. Although there are several good reports on the survival rate of HR at midterm follow up, the biological changes of the femoral head underlying the implant over time should always be considered. It remains to be seen whether other late

failures will occur. HR is still a good indication for young and active patients; nevertheless good bone quality remains the crucial element to support the implant at longer follow-up.

ACKNOWLWDGEMENTS

This work was supported by Rete Nazionale di Ricerca TISSUENET (n. RBPR05RSM2). None of the authors has professional and financial affiliations that may be perceived to have biased the presentation.

Chapter 11
MicroCT preliminary analysis on granules charachteristics from *in vivo* study using a new injectable multiphasic bone substitutes based on gel-coated OsproLife® HA/TTCP [166]

Abstract presented at MiMe 1st International Conference on Materials in Medicine, Faenza, Italy, 8-11 October 2013

Parrilli A[1,2], Maglio M[2], Giavaresi G[1,2], Pierini M[3], Lucarelli E[3], Preve E[4], Prosperi S[4], Piccinini M[4], Bucciotti F[4], Donati D[3,5], Fini M[1,2], Giannini S[3,5]

[1] Biocompatibility, Technological Innovations and Advanced Therapies Laboratory (BITTA), Rizzoli RIT Department, Rizzoli Orthopaedic Institute, Italy

[2] Laboratory of Preclinical and Surgical Studies, Rizzoli Orthopaedic Institute, Bologna, Italy

[3] Osteoarticular Regeneration Laboratory, Rizzoli Orthopaedic Institute, Bologna

[4] Eurocoating S.p.A, Pergine Valsugana, Trento, Italy

[5] Orthopaedic and Trauma Clinic III, Rizzoli Orthopaedic Institute, Bologna, Italy

Chapter 11. MicroCT preliminary analysis on granules characteristics from *in vivo* study using a new injectable multiphsic bone substitute based on gel-coated OsroLife® HA/TTCP

11.1 Introduction

In the field of preclinical orthopaedic studies, microCT can be used in several different kinds of evaluations allowing 3D quantitative analysis in a non-destructive way [3]. In this study, injectable calcium phosphates bioceramics were used in an ovine model in order to stimulate bone regeneration. The in vivo behaviour of a new injectable multiphasic bone substitutes (MBS) based on gel-coated OsproLife HA/TTCP granules (gel-HA/TTCP) (Eurocoating SpA) was investigated and compared to OsproLife® HA/TTCP.

11.2 Materials and Methods

Under general anaesthesia, 4 sheep underwent surgical implants of 4 HA/TTCP and 4 gel-HA/TTCP specimens, randomly, in lateral femoral condyles. Six weeks later, microtomographic (microCT system Skyscan-1172) analysis was carried out on the explanted condyles. The evaluated parameters on materials were:

- material volume MatV/TV (in %), as the ratio between material volume and the total volume of the created bone defect;
- 3D granules diameter (in mm), as volume-equivalent sphere diameter (Mat.p.ESDV) or surface-equivalent sphere diameter (Mat.p.ESDA);
- average volume of granules Mat.p.V (in mm3);
- granules connectivity Mat.Conn (N), indicating the number of redundant connections between structures per unit volume can be considered as an estimation of "packing" between granules.

11.3 Results

The preliminary results on materials parameters analysed are summarized in Figure 11.1.

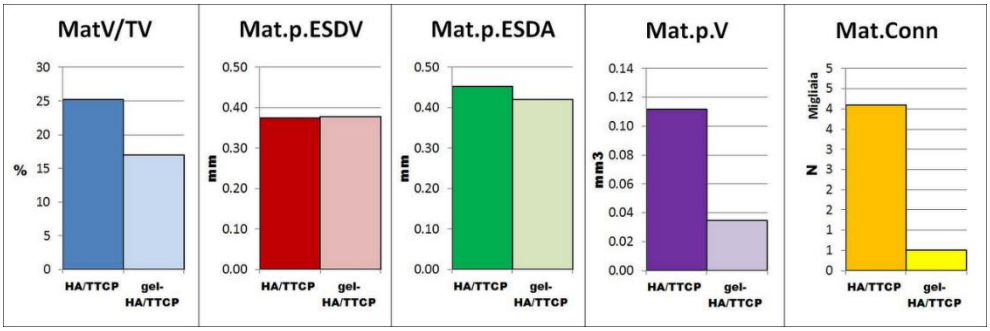

Figure 11.1 *– Histograms of the preliminary microCT results on materials.*

11.4 Conclusions

The results shows that gel-coated granules are less packed (Figure 11.2) and could, in this way, stimulate bone colonization with more efficacy.

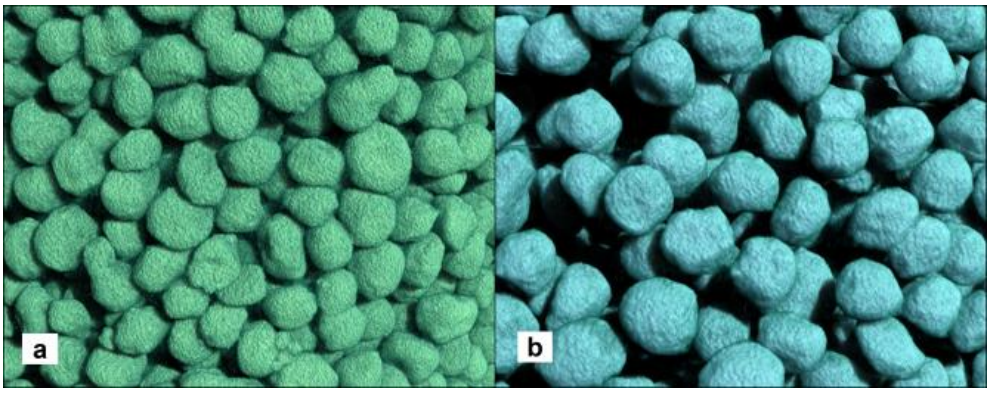

Figure 11.2 *– a) 3D rendering of OsproLife HA/TTCP granules; b) 3D rendering of gel-HA/TTCP granules.*

ACKNOWLEDGMENTS

The work is part of "CaP Project" cosponsored by Eurocoating SpA and Provincia Autonoma di Trento (Regional Public Authority).

Chapter 12
Osteoinductive *in vivo* behaviour of three-dimensional interconnected porous scaffolds over time

12.1 Introduction

Micro-CT, deriving from clinical CT, is an important non destructive tool that can allow studying the interactions between biomaterials and bone tissue also in a longitudinal way. The statistical power of longitudinal studies compared to cross-sectional studies has a greater meaning principally because the effect of an implanted biomaterial can be evaluated over time in the same sample. In fact, an in vivo micro-CT analysis allows an assessment and quantification of the development over time in healing processes due to the application of engineered devices. The ability to study the time evolution of anatomical changes occurring in the course of the experiment could exclude the use of different experimental groups and, thus, has a significant ethical meaning that should not be underestimated.

Limitations of the in vivo micro-CT image acquisition are: the complexity of displaying small structures that are moving dynamically due principally to breathing and heart beating; the limitation in administered x-ray dose distribution per animal due to the destructive effects on living organisms and cells; and the linear attenuation coefficient specific for every material including animal soft and hard tissues.

12.2 Materials and Methods

Male nude mice were used to study the development of osteoinduction of scaffolds implanted subcutaneously up to 8 weeks of experimental time. Three types of biomaterials were used: a gelatin crosslinked with genipin and washed in glycine and water (GEL); GEL with 10% hydroxyapatite (GEL-HA10), and a control biomaterial based only on hydroxyapatite (HA). Biomaterials without cells were implanted in the left surgically created subcutaneous pockets, while scaffolds engineered with commercial mesenchymal cells (hMSC) induced to osteogenic differentiation were implanted in the right pockets. The animals were divided into three groups: group 1): 10 mice, implanted on the right with GEL and on the left with the GEL + hMSC; group 2): 10 mice, implanted on the right with GEL-HA10 and on the left with the GELHA10 + hMSC; Group 3): implanted on the right with HA and on the left with the HA + hMSC. At every the experimental times (surgical implant, 4 weeks and 8 weeks), each implant was analyzed by micro–CT using computed microtomographic in vivo equipment Skyscan 1176. The scans were performed with a voltage source of 50kV and a current source of 500μA. Images were acquired with a pixel size of 9μm. Reconstruction was performed by using software NRecon (v1.6.8.0, Bruker): a specific alignment was used for each sample,a medium intensity ring artifacts correction and a beam hardening correction were applied.

12.3 Results and discussion

Mineralization was observed in group 1 at 4 and 8 weeks only in the left implants (Figure 12.1). In group 2, the mineralization was present in both the implant sites (Figure 12.2). In the control group, no bone formation or mineralization was observed (Figure 12.3).

The in vivo micro-CT acquisition allowed the evaluation over time of the mineralization grade of the implanted scaffolds.

ACKNOWLEDGMENTS

This research has been supported by a grant from the Italian Ministry of Health: Firb n. RBAP10MLK7 "Scaffold per la rigenerazione dei tessuti scheletrici: valutazione preclinica della loro compatibilità ed efficienza"

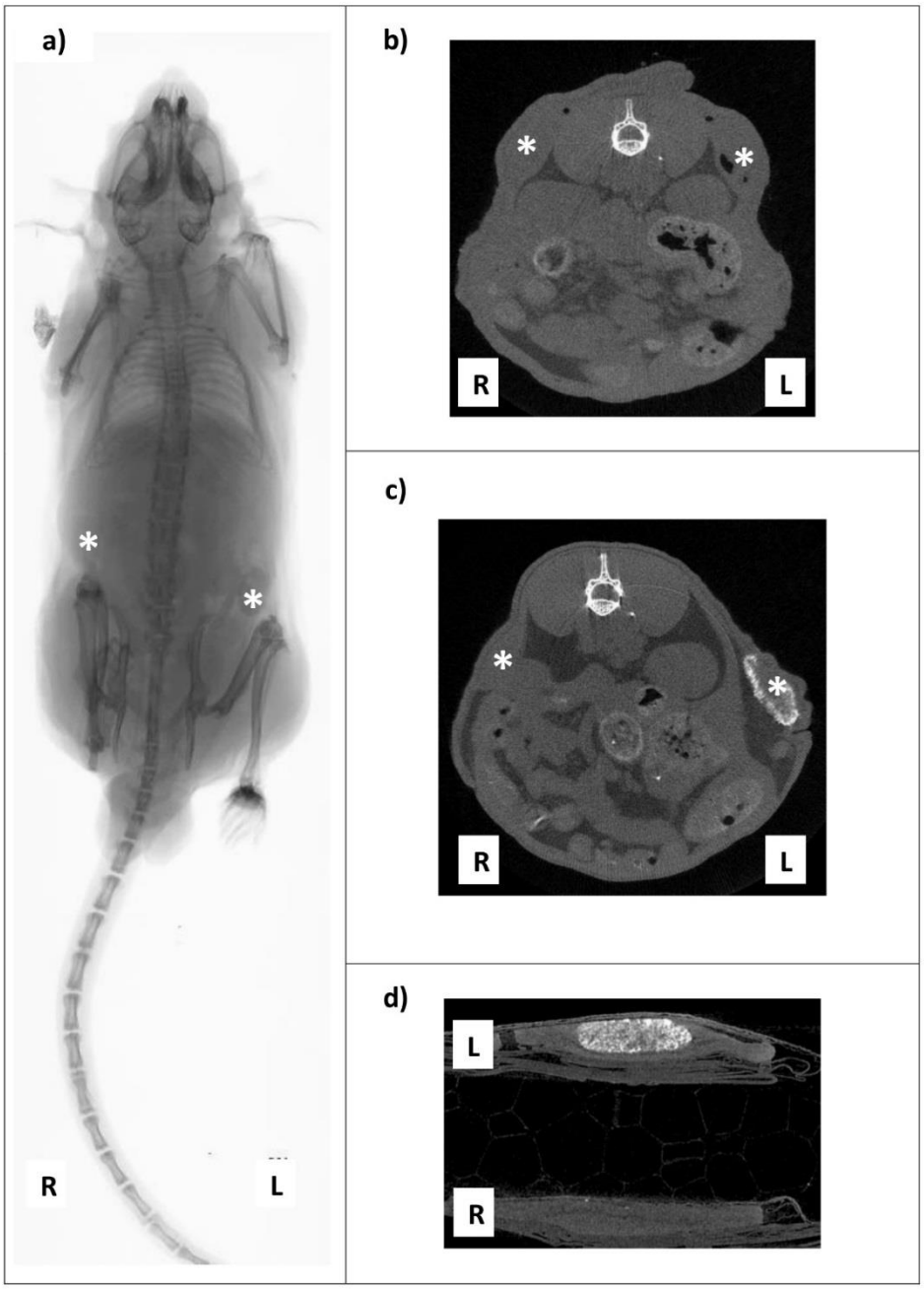

Figure 12.1 *– Micro-CT images of samples in group 1 of the study for the evaluation of the osteoinductive behaviour of three-dimensional interconnected porous scaffolds of gelatin. GEL was implanted on the right side, while GEL + hMSC was implanted on the left side. a) Radiographic micro-CT scan of a sample at 4 weeks of experimental time. Subcutaneous implants are highlighted with asterisks. b) Micro-CT sections of a sample just after the surgical implantation of the scaffold. c) Micro-CT sections of a sample at 4 weeks of experimental time. Sign of mineralization are present in the left side. d) Micro-CT sections of an explanted sample at 8 weeks of experimental time. Sign of mineralization are still present only in the left side.*

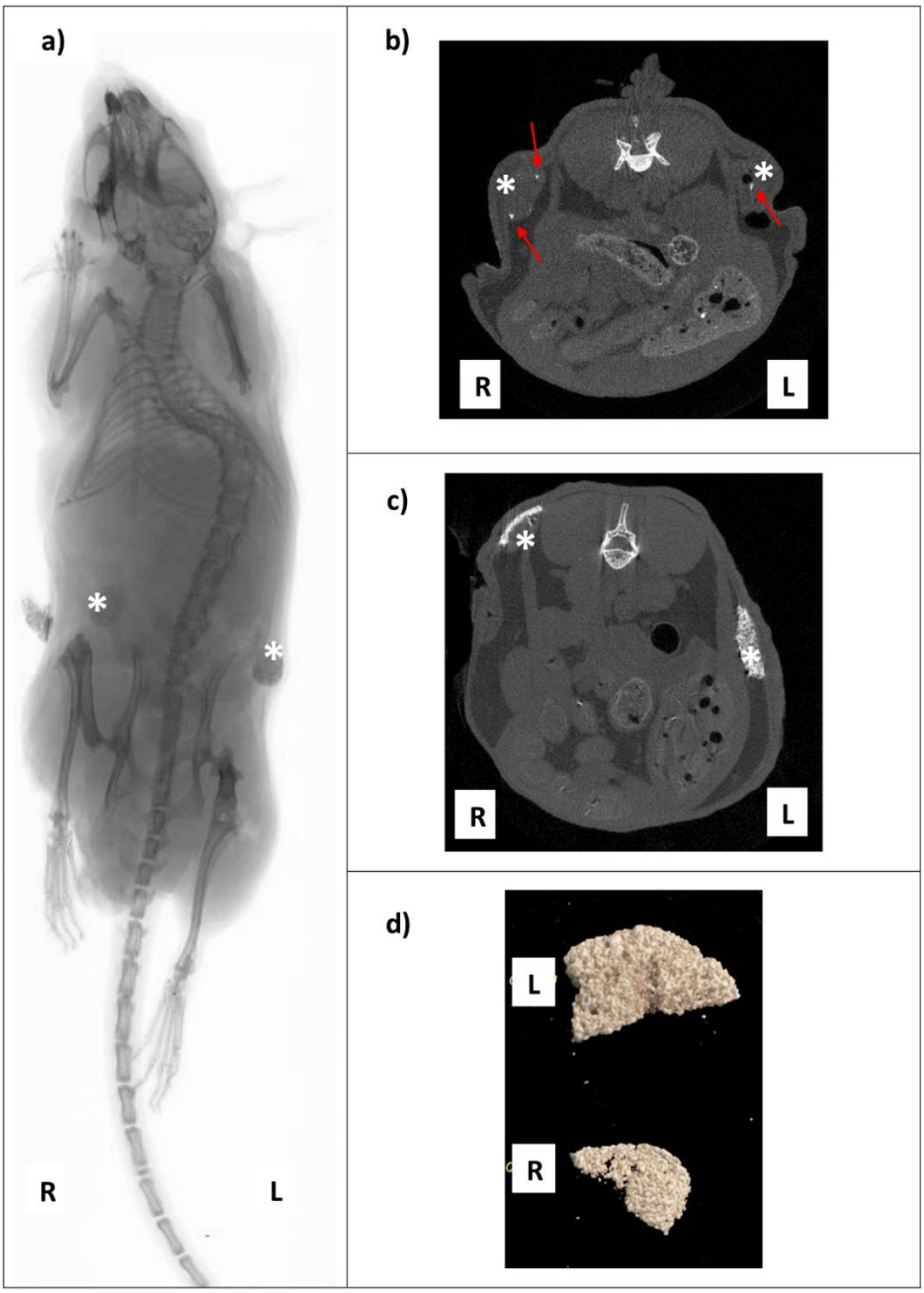

Figure 12.2 *– Micro-CT images of samples in group 2 of the study for the evaluation of the osteoinductive behaviour of three-dimensional interconnected porous scaffolds of gelatin. GELHA10 was implanted on the right side, while GELHA10 + hMSC was implanted on the left side. a) Radiographic micro-CT scan of a sample at 8 weeks of experimental time. Subcutaneous implants are highlighted with asterisks. b) Micro-CT sections of a sample just after the surgical implantation of the scaffold. The red arrows highlight the HA particles of the scaffold. c) Micro-CT sections of a sample at 8 weeks of experimental time. Sign of mineralization are present both in the left and in the right sides. d) 3D models of the mineralization in the scaffolds.*

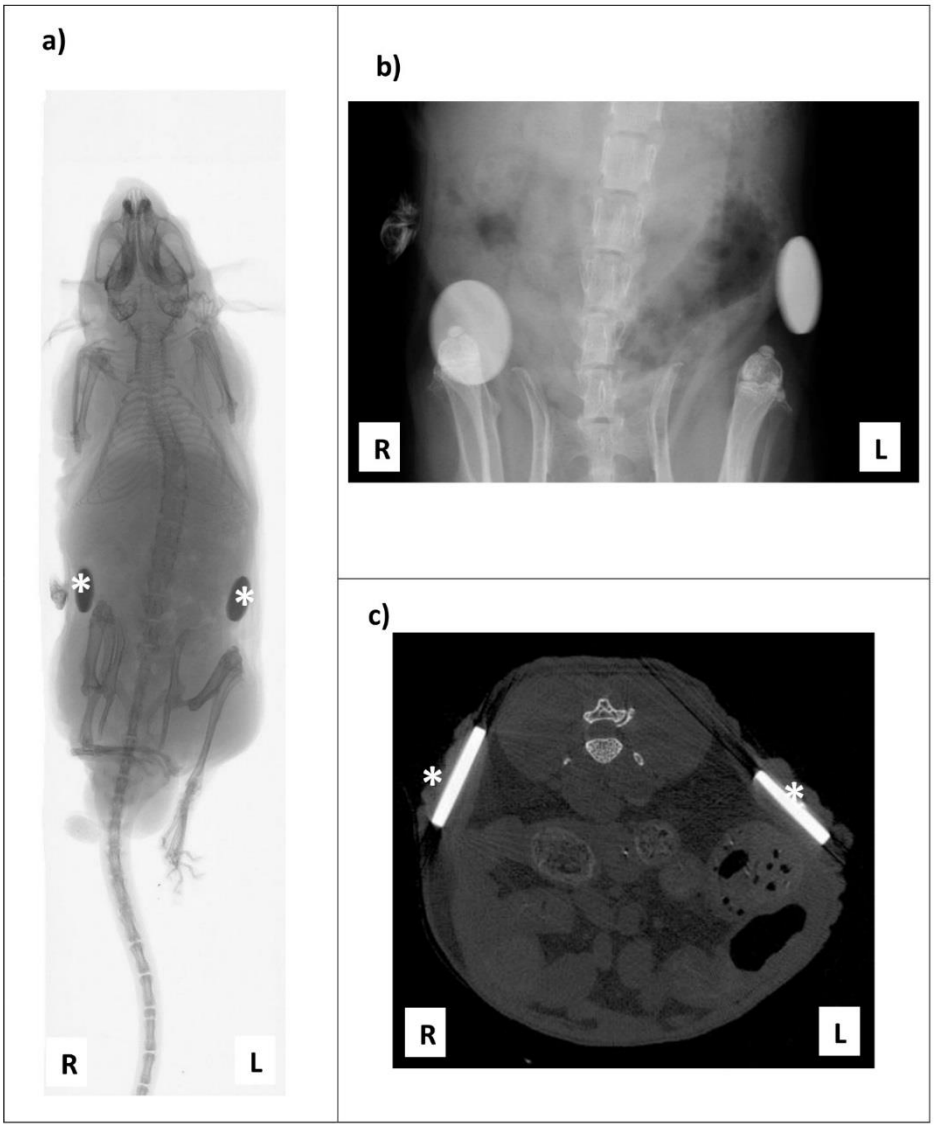

Figure 12.3 *– Micro-CT images of samples in group 3 of the study for the evaluation of the osteoinductive behaviour of three-dimensional interconnected porous scaffolds of gelatin. HA was implanted on the right side, while HA + hMSC was implanted on the left side. a) Radiographic micro-CT scan of a sample at 8 weeks of experimental time. Subcutaneous implants are highlighted with asterisks. b) Radiographic micro-CT scan detail of a sample at 8 weeks of experimental time. c) Micro-CT sections of a sample at 8 weeks of experimental time. No sign of mineralization are present in both sides.*

Chapter 13
Osteoarthritis treatment with engineered hyaluronic acid scaffolds: a densitometric analysis

13.1 Introduction

In addition to the evaluation over time of morphological 3D parameters, it is possible to evaluate the mineral content and its variations due to the principle that the gray levels of every micro-CT section give a map of the distribution of the absorption coefficients of the X-rays related to the analyzed sample. Such coefficients depend on the material density, from the atomic number of the elements that constitute it and from the incidental energy used. In orthopedic preclinical studies, usually two different densitometric parameters are evaluated: Bone Mineral Density (BMD) and Tissue Mineral Density (TMD) [34]. The main differences is that TMD is calculated from only the volume of calcified tissue excluding the surrounding soft tissue or "non-bone" voxels. Mineralization is an important aspect in several bone disease evolution such as, for example, osteoporosis or osteoarthritis.

13.2 Materials and Methods

Densitometric analysis of bone quality was carried out in the in vivo study for the evaluation of the use in large animals of mesenchymal stem cells from bone marrow (expanded in vitro or prepared with "one step" technique in the operating room) in combination with a hyaluronic acid scaffold for the treatment of osteoarthritis (OA). The animals were divided into five groups: group 1): OA animals implanted with hyaluronic scaffold engineered with in vitro expanded mesenchymal stem cells from bone marrow MSC+HYAFF; group 2): OA animals implanted with hyaluronic scaffold engineered with mesenchymal stem cells from bone marrow isolated with "one step" technique BMC+HYAFF; group 3) OA animals implanted with hyaluronic scaffold HYAFF; group 4): OA animals with no treatment MMX; and group 5): healthy animals CONTROL. Micro-CT assessment was carried out ex-vivo on the explanted femur condyles and tibiae plates using the Skyscan 1176 system. The scans were performed with a 65kV voltage source and 385μA current source. Images were acquired with a pixel size of 35 μm, an aluminum filter 0.5 mm, and a sample rotation step of 0.7°. The same specifications were set to acquire two calibration phantoms with a specific content of CaHA (calcium Hydroxyapatite). Reconstruction was performed by using NRecon (v1.6.8.0) software: a specific alignment was used for each sample, a ring artifact correction and a beam hardening correction were applied. Microtomographic 3D densitometric analyses were performed using CTAn (v.1.13) software and the following parameters were calculated:

– Bone mineral density (BMD, $g \cdot cm^3$)
– Tissue mineral density (TMD, $g \cdot cm^3$

13.3 Results and Discussion

The results of micro-CT parameters for each group are reported in Figure 13.1. Results, in terms of mineral content, showed a greater effectiveness in OA treatment when the hyaluronic scaffold is engineered with in vitro expanded cells. This effect is more evident in the cortical subchondral bone of the femur component of the joint.

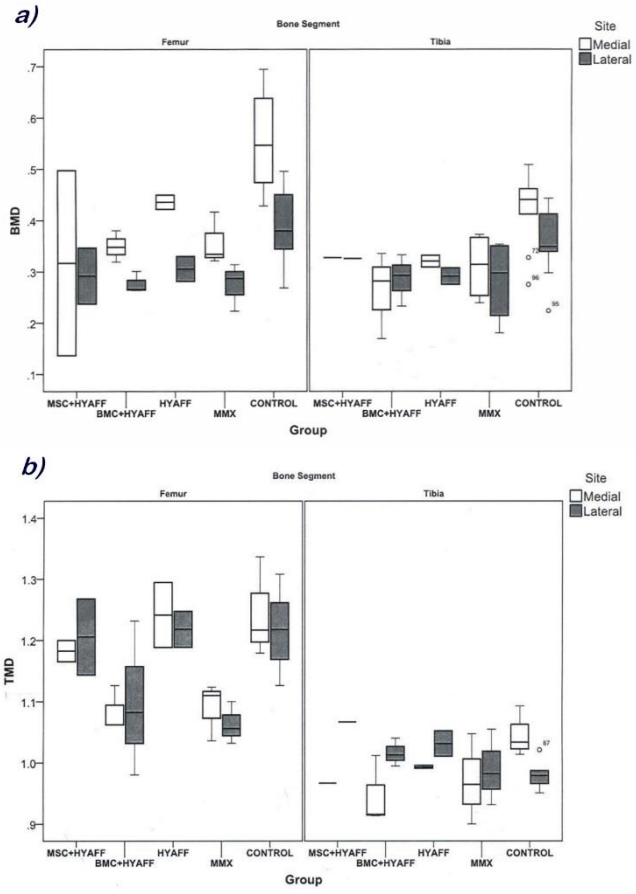

Figure 13.1 *– Box plot of results of a) BMD and b) TMD of the study for the evaluation of bone quality in terms of mineral content in a study of osteoarthritis treatment in a large animal model with engineered hyaluronic acid scaffolds.*

ACKNOWLEDGMENTS

This research has been supported by the project of the Italian Ministry of Healt (2011-2013) "Development of novel methodology for the translation of adult stem cell therapy to the clinical regeneration of cartilage". This work was conducted in collaboration with the Laboratory of Immunorheumatology and tissue regeneration of the Rizzoli Orthopaedic Institute.

PART IV
CONCLUSIONS

Chapter 14
Summary and Conclusions

Micro-CT is a very useful non-destructive technique for the 3D study of bone, biomaterials and their interactions because it is able to supply structural and densitometric information by obtaining images of the internal structure of a small object with a high spatial resolution. Besides, Micro-CT is an important tool to study the interactions between biomaterials and bone tissue from a 3D point of view

Typical uses in biomedical fields include the study of *in vitro* bone samples and biomaterials such as hydroxyapatite (HA), bioactive glasses, pharmaceutical granules, metals and composites (polymers + HA or calcium phosphate). Usually, the most evaluated material parameter is porosity because it plays a dominant role in the biomechanical characteristics, the initial cell attachment and thus the subsequent tissue regeneration.

Due to the linear attenuation coefficient specific for every material, is important to set X-ray source voltage and image reconstruction corrections depending on involved materials.

More specifically, bone is a connective tissue composed by an average of about 2/3 of inorganic substances and 1/3 of organic substances. The main constituents of the inorganic matrix of bone is a mixture of HA and TCP while biomaterials in orthopedics can be enclosed within two categories:

- biomaterials used as replacement of bone to stimulate tissue regeneration and that can be completely absorbed and degraded (mainly ceramic and polymers);

- biomaterials for prosthetic implants that have mechanical properties that ensure stabilization of fractures or damaged joints (mainly metals, ceramics or high density polymers).

Moreover, micro-CT, deriving from clinical CT, allow studying the interactions between biomaterials and bone tissue also in a longitudinal way. The statistical power of longitudinal studies compared to cross-sectional studies has a great meaning principally because the effect of an implanted biomaterial can be evaluated over time in the same sample. In fact, an *in vivo* micro-CT analysis allows an assessment and quantification of the development over time in healing processes due to the application of engineered medical devices. The ability to study the time evolution of anatomical changes occurring in the course of the experiment could exclude the use of different experimental groups and, thus, has a significant ethical meaning that should not be underestimated. Limitations of the *in vivo* micro-CT image acquisition are: the complexity of displaying small structures that are moving dynamically due principally to breathing and heart beating; the limitation in administered X-ray dose distribution per animal due to the destructive effects on living organisms and cells; and the linear attenuation coefficient specific for every material including animal soft and hard tissues.

The evaluation of the mineral content is another important and peculiar task of micro-CT. The variations in mineral content are determinable due to the principle that the gray levels of every micro-CT section give a map of the distribution of the absorption coefficients of the X-rays related to the analyzed sample. Such coefficients depend on the material density, from the atomic number of the elements that constitute it and from the incidental energy used. In orthopedic preclinical studies, usually two different densitometric parameters are evaluated: Bone Mineral Density (BMD) and Tissue Mineral Density (TMD). Mineralization is an important aspect in several bone disease evolution such as, for example, osteoporosis or osteoarthritis.

The first year of the research was dedicated to the micro-CT analysis of different kinds of biomaterials in the pre-implantation phase studying new procedures to widen the acquisition possibilities and the kinds of quantitative analytical methods.

In particular the project followed 3 different research lines:

a) the study of thixotropic carboxymethylcellulose (CMC) hydrogels added with iron magnetic-nanoparticles (CMC-NPs) examining the differences in magnetic particles distribution and using a micro-CT freezing chamber to overcome the limitation of movements during the acquisition;

b) the study of the 3D cell (MG63) distribution seeded onto a polymeric scaffold using osmium tetroxide as contrast agent and developing a new micro-CT segmentation protocol;

c) the study of dimensional metrology establishing an approach for the quantification of wear in ZrO_2 head prosthesis components using micro-CT and to validate the method comparing it with the gold standard, i.e. the gravimetric analysis.

The second year was dedicated to the study of the interactions between different types of biomaterials implanted in bone tissue. The micro-CT analyses were performed as a result of *in vivo* preclinical studies and clinical retrieved studies. During this year, the project was divided in the following research lines:

a) the evaluation of the *in vivo* behaviour of ceramic custom made prosthesis in a suitable animal model (adult sheep) at 6 and 12 months from surgical cranioplasty;

b) the evaluation of the characteristics of bone quality and its microarchitecture in retrieved metal-on-metal Metal-on-metal HR;

c) the analysis of granules characteristics using a new injectable multiphasic bone substitutes based on gel-coated OsproLife® HA/TTCP.

During the third year, the non “functional”, i.e. non quantitative, information obtainable from a micro-CT analysis was deepened, testing the most important computer algorithms for 3D visualization and

modelling: maximum intensity projection (MIP), shaded surface display (SSD) and volume rendering (VR).

Moreover, the Micro-CT analyses performed were divided in the following research lines:

a) the evaluation of the *in vivo* osteoinductive behaviour of three-dimensional interconnected porous scaffolds of gelatin with or without contents of nanocrystalline HA over time;

b) the evaluation of bone quality in terms of mineral content in a study of osteoarthritis treatment in a large animal model with engineered hyaluronic acid scaffolds.

The main objective of this PhD research was to develop innovative techniques and procedures of 3D image analysis for the characterization of polymeric, ceramic and metal biomaterials used in various fields of bone tissue preclinical research.

In detail the aims can be summarized in:

– assessing micro-CT procedures applicable to pre-implanted biomaterials through both metrological studies and *in vitro* studies of 3D cell scaffold colonization, with the definition of effective segmentation techniques;

– developing micro-CT techniques to evaluate different kinds of implanted biomaterials both *ex vivo* and *in vivo* establishing standard test protocols and identifying the mechanisms of material resorption and degradation in physiological environment and the mechanisms of bone remodeling;

– exploring the densitometric analysis in relation to the contribution of mineralization in healing process at peri-implant site.

These program objectives have been achieved through the development of reliable experimental procedures for the morphological and mechanical evaluation of implantation biomaterials (scaffold and prostheses); the investigation of a large number of possible applications of biomaterials in orthopedic preclinical studies through *in vitro*, *ex-vivo* and *in vivo* micro-CT analysis; the elaboration of new interpretative models of the bone regeneration mechanisms through 3D morphometric

parameters; and the extension of the knowledge and the expertise in 3D biomaterial evaluations used in orthopedic research.

Chapter 14. Summary and conclusions

References

[1] Giardino R, Fini M, Nicoli Aldini N, **Parrilli A**. Testing the in vivo biocompatibility of biocomposites Chapter 16 of the book "Biomedical composites" Edited by Luigi Ambrosio Published by Woodhead Publishing Limited

[2] ASTM E1441-11. Standard guide for computed tomography (CT) imaging. Technical report, American Society for Testing and Materials, 2011.

[3] Stock SR. MicroComputed Tomography - methodology and applications. CRC Press Taylor & Francis Group, 2009.

[4] Hounsfield GN. Computerized transverse axial scanning (tomography): Part1. description of system. British Journal of Radiology, 1973;46:1016-1022.

[5] Sasov A, Van Dyck D. Desktop X-ray microscopy and microtomography. Journal of Microscopy, 1998;191(2):151-158.

[6] Van de Casteele E. Model-based approach for beam hardening correction and resolution measurements in microtomography, Faculty Wetenschappen, Department Natuurkunde Antwerpen: University Antwerpen, 2004

[7] Gonzalez RC. Digital image processing. Addison-Wesley Publishing Company, Reading (USA) 1987.

[8] Kak AC, Slaney M. Principles of computerized tomographic imaging. IEEE press, New York, 1998.

[9] Brooks RA Di Chiro G. Beam hardening in X-ray reconstructive tomography. Physics in Medicine and Biology, 21(3):390-398, 1976.

[10] De Paiva RF, Lynch J, Rosenberg R, Bisiaux M. A beam hardening correction for x-ray microtomography. Nondestructive testing and evaluation, 31(1):17-22, February 1998.

[11] Kasperl S, Hiller J, Krumm M. Computed Tomography Metrology in Industrial Research & Development. Development. 2008.

[12] Krumm M, Kasperl S, Franz M. Reducing non-linear artifacts of multi-material objects in industrial 3D computed tomography. NDT & E International. 2007

[13] Meng F, Zhang N, Wang W. Virtual experimentation of beam hardening effect in X-ray CT measurement of multiphase flow. Powder Technology. 2009;194(1-2):153-157.

[14] Amini AR, Laurencin CT, Nukavarapu SP. Bone tissue engineering: recent advances and challenges. Crit Rev Biomed Eng. 2012;40(5):363-408. Review. PubMed PMID: 23339648; PubMed Central PMCID: PMC3766369.

[15] Furth ME, Atala A, Van Dyke ME. Smart biomaterials design for tissue engineering and regenerative medicine. Biomaterials. 2007 Dec;28(34):5068-73. Epub 2007 Aug 15. PubMed PMID: 17706763.

[16] Biodegradable Systems in Tissue Engineering and Regenerative Medicine Edited by Rui L . Reis and Julio San Román CRC Press 2004 Print ISBN: 978-0-8493-1936-5 eBook ISBN: 978-0-203-49123-2.

[17] Dimitriou R, Jones E, McGonagle D, Giannoudis PV. Bone regeneration: current concepts and future directions. BMC Med. 2011 May 31;9:66. doi: 10.1186/1741-7015-9-66. Review. PubMed PMID: 21627784; PubMed Central PMCID: PMC3123714.

[18] Le Meng Bao C, Teo EY, Chong MSK, Liu Y, Choolani M, Chan JKY. Advances in Bone Tissue Engineering, Regenerative Medicine and Tissue Engineering, Prof. Jose A. Andrades (Ed.), 2013, ISBN: 978-953-51-1108-5, InTech, DOI: 10.5772/55916.

[19] Bilezikian Lawrence G. RaiszT. In Principles of Bone Biology (Third Edition), edited by John P. John Martin, Academic Press, San Diego, 2008, ISBN 9780123738844

[20] Burr DB and Akkus O, Chapter 1 - Bone Morphology and Organization, In Basic and Applied Bone Biology, edited by David B. BurrMatthew R. Allen, Academic Press, San Diego, 2014, Pages 3-25, ISBN 9780124160156, http://dx.doi.org/10.1016/B978-0-12-416015-6.00001-0.

[21] Jang JH, Castano O, Kim HW. Electrospun materials as potential platforms for bone tissue engineering, Advanced Drug Delivery Reviews, Volume 61, Issue 12, 5 October 2009, Pages 1065-1083, ISSN 0169-409X.

[22] Gilbert SF. Developmental Biology. 6th edition. Sunderland (MA): Sinauer Associates; 2000. Osteogenesis: The Development of Bones. Available from: http://www.ncbi.nlm.nih.gov/books/NBK10056/

[23] Coxon JP, Oades GM, Colston KW, Kirby RS. Advances in the use of bisphosphonates in the prostate cancer setting. Prostate Cancer Prostatic Dis. 2004;7(2):99-104. Review.

[24] Consensus Conference of European Society of Biomaterials, Sorrento, 2005

[25] Hollinger JO, Sfeir C. Bone Tissue Engineering Edited by Bruce A . Doll , Thomas A . Einhorn , CRC Press 2004 Print ISBN: 978-0-8493-1621-0 eBook ISBN: 978-0-203-49509-4

[26] Biomaterials Principles and Applications. Edited by Joon B . Park and Joseph D . Bronzino CRC Press 2002 Print ISBN: 978-0-8493-1491-9 eBook ISBN: 978-1-4200-4003-6

[27] Handbook o Biomaterials properties. Edited by Johnatan Black and Garth Hastings. Published by Chapman & Hall 1998 ISBN 0 412 603306

[28] Williams DF. Biocompatibility of orthopaedic implants. Vol.I, CRC Press, Boca Raton, Florida. 1982

[29] Schouten C, Meijer GJ, van den Beucken JJ, Spauwen PH, Jansen JA. The quantitative assessment of peri-implant bone responses using histomorphometry and micro-computed tomography. Biomaterials. 2009 Sep;30(27):4539-49

[30] Boyne P.J. Performance of bone grafts in reconstructive surgery. In: Biocompatibility of bone natural tissues and their synthetic analogues., D.F.Williams ed., CRC Press, Boca Raton, Florida.1984

[31] Albrektsson T, Johansson C. Osteoinduction, osteoconduction and osseointegration. Eur spine J 2001 10:S96-S101

[32] Legeros RZ, Craig R G. Strategies to affect bone remodeling: Osteointegration. J Bone Miner Res, 1993, 8: S583–S596.

[33] Parfitt AM, Drezner MK, Glorieux FH, Kanis JA, Malluche H, Meunier PJ, Ott SM, Recker RR (1987) Bone Histomorphometry: standardization of nomenclature, symbols and units. J. Bone Miner. Res. 2 (6): 595-610.

[34] Bouxsein ML, Boyd SK, Christiansen BA, Guldberg RE, Jepsen KJ, Müller R. Guidelines for assessment of bone microstructure in rodents using micro-computed tomography. J Bone Miner Res. 2010 Jul;25(7):1468-86. Review.

[35] Ko HF, Sfeir C, Kumta PN. Novel synthesis strategies for natural polymer and composite biomaterials as potential scaffold for tissue engineering, Philos Transact A Math Phys Eng Sci; 2010; 368:1981-97.

[36] Pasqui D, De Cagna M, Barbucci R. Polysaccharide-Based Hydrogels: The Key Role of Water in Affecting Mechanical Properties. Polymers. 2012; 4(3):1517-1534.

[37] Okay, O. General properties of hydrogels. In Hydrogel Sensors and Actuators, 1st ed., Gerlach, G., Arndt, K.-F. Eds., Springer: Berlin, Germany, 2009; pp. 1–14.

[38] Giani G, Fedi S, Barbucci R. Hybrid Magnetic Hydrogel: A Potential System for Controlled Drug Delivery by Means of Alternating Magnetic Fields. Polymers. 2012; 4(2):1157-1169.

[39] **Parrilli A**, Pagani S, Maltarello MC, Santi S, Salerno A, Netti PA, Giardino R, Rimondini L, Fini M. Three-dimensional cellular distribution in polymeric scaffolds for bone regeneration: a microCT analysis compared to SEM, CLSM and DNA content. J Microsc. 2014 Jul;255(1):20-9.

[40] Duan B, Wang M, Zhou WY, Cheung WL, Li ZY, Lu WW. Three-dimensional nanocomposite scaffolds fabricated via selective laser sintering for bone tissue engineering. Acta Biomater. 2010;6:4495-4505.

[41] Scherberich A, Müller AM, Schäfer DJ, Banfi A, Martin I. Adipose tissue-derived progenitors for engineering osteogenic and vasculogenic grafts. J Cell Physiol. 2010;225:348-353.

[42] Sundelacruz S, Kaplan DL. Stem cell- and scaffold-based tissue engineering approaches to osteochondral regenerative medicine. Semin Cell Dev Biol. 2009;20:646-655.

[43] Rajagopalan S, Robb RA. Schwarz meets Schwann: Design and fabrication of biomorphic and durataxic tissue engineering scaffolds. Med. Image Anal. 2006;10:693-712.

[44] Dorsay SM, Lin-Gibson S, Simon CG Jr. X-ray microcomputed tomography for the measurement of cell adhesion and proliferation in polymer scaffolds. Biomaterials. 2009;30:2967-2974.

[45] Hiu-Yan Y, Ling Q, Kwong-Man L, Ming Z, Kwok-Sui L, Chun-yiu CJ. Novel approach for quantification of porosity for biomaterial implants using microcomputed tomography (μCT). J Biomed Mater Res B. 2005;75:234-242.

[46] Karageorgiou V, Kaplan D. Porosity of 3D biomaterial scaffold and osteogenesis. Biomaterials. 2005;26:5474-5491.

[47] Malafaya PB, Santos TC, Van Griensven M, Reis RL. Morphology, mechanical characterization and in vivo neo-vascularization of chitosan particle aggregated scaffold architectures. Biomaterials. 2008;29:3914-3926.

[48] Mathieu LM, Mueller TL, Bourban PE, Pioletti DP, Müller R, Månson JAE. Architecture and properties of anisotropic polymer composite scaffold for bone tissue engineering. Biomaterials. 2006;27:905-916.

[49] Shum AWT, Mak AFT. Morphological and biomechanical characterization of poly(glycolic acid) scaffolds after in vitro degradation. Polym Degrad Stabil. 2003;81:141-149.

[50] Intranuovo F, Howard D, White LJ, Johal RK, Ghaemmaghami AM, Favia P, et al. Uniform cell colonization of porous 3-D scaffolds achieved using radial control of surface chemistry. Acta Biomater. 2011;7:3336-3344.

[51] Zehbe R, Goebbels J, Ibold Y, Gross U, Shubert H. Three-dimensional visualization of in vitro cultivated chondrocytes inside porous gelatine scaffolds: A tomographic approach. Acta Biomater. 2010;6:2097-2107.

[52] Metsher BD. MicroCT for developmental biology: a versatile tool for high-contrast 3D imaging and histological resolutions. Dev Dynam. 2009;238:632-640.

[53] Salerno A, Guarnieri D, Iannone M, Zeppetelli S, Netti PA. Effect of Micro- and Macroporosity of Bone Tissue Three-Dimensional-Poly(ε-Caprolactone) Scaffold on Human Mesenchymal Stem Cells Invasion, proliferation, and Differentiation in Vitro. Tissue Eng A. 2010;16:2661-2673.

[54] Chen Y, Zhou S, Li Q. Microstructure design of biodegradable scaffold and its effect on tissue regeneration. Biomaterials. 2011;32:5003-5014.

[55] Jones CW, Smolinski D, Keogh A, Kirk TB, Zheng MH. Confocal laser scanning microscopy in orthopaedic research. Prog Histochem Cytochem. 2005;40(1):1-71.

[56] Otsu N. Threshold selection method from grey level histograms. IEEE T Syst Man Cyb C. 1979;9:62-66.

[57] Shaw M, Faruqui N, Gurdak E, Tomlins P. Three-Dimensional cell morphometry for the quantification of cell-substrate interactions. Tissue Eng C. 2013;19(1):48-56.

[58] Mechels FPW, Barradas AMC, Van Bitterswijk CA, De Boer J, Feijen J, Grijpma DW. Effect of the architecture of tissue engineering scaffolds on cell seeding and culturing. Acta Biomater. 2010;6:4208-4217.

[59] Levi B, Nelson ER, Brown K, James AW, Xu D, Dunlevie R, et al. Differences in osteogenic differentiation of adipose-derived stromal cells from murine, canine, and human sources in vitro and in vivo. Plast Reconstr Surg. 2011;128(2):373-386.

[60] Rada T, Reis RL, Gomes ME. Adipose Tissue-derived stem cells and their application in bone and cartilage tissue engineering. Tissue Eng B 2009;15:113-125.

[61] Casteilla L, Planat-Benard V, Laharrague P, Cousin B. Adipose-derived stromal cells: their identity and uses in clinical trials, an update. World J Stem Cell. 2011;3:25-33.

[62] Gimble JM, Katz AJ, Bunnel BA. Adipose-derived stem cells for regenerative medicine. Circ Res. 2007;100:1249-1260.

[63] Nakagami H, Morishita R, Maeda K, Kikuchi Y, Ogihara T, Kaneda Y. Adipose Tissue-derived stromal cells as novel option for regenerative cell therapy. J Atheroscler Thromb. 2006;13:77-81.

[64] Zuk PA, Zhu M, Ashjian P, De Ugarte DA, Huang JI, Mizuno H, et al. Human adipose tissue is a source of multipotent stem cells. Mol Biol Cell. 2002;13:4279-4295.

[65] Affatato S, Spinelli M, Zavalloni M, Mazzega-fabbro C, Viceconti M. Tribology and total hip joint replacement : Current concepts in mechanical simulation. Medical Engineering & Physics. 2008;30:1305-1317.

[66] Bills P, Blunt L, Jiang X. Development of a technique for accurately determining clinical wear in explanted total hip replacements. Wear. 2007;263:1133-1137.

[67] Bowden AE, Kurtz SM, Edidin AA. Validation of a micro-CT technique for measuring volumetric wear in retrieved acetabular liners. Journal of biomedical materials research. Part B, Applied biomaterials. 2005;75(1):205-9.

[68] Carmignato S, Savio E. Traceable volume measurements using coordinate measuring systems. CIRP Annals - Manufacturing Technology. 2011;60(1):519-522

[69] Soto MO, Rodriguez Ja, Ranawat CS. Clinical and radiographic evaluation of the Harris-Galante cup: incidence of wear and osteolysis at 7 to 9 years follow-up. The Journal of arthroplasty. 2000;15(2):139-45.

[70] Sugano N, Saito M, Yamamoto T, et al. Analysis of a retrieved UHMWPE acetabular cup crosslinked in air with 1000 kGy of gamma radiation. Journal of orthopaedic research: official publication of the Orthopaedic Research Society. 2004;22(4):828-31

[71] Bradford L, Baker DA, Graham J, Chawan A, Ries MD, Pruitt LA. Wear and surface cracking in early retrieved highly cross-linked polyethylene acetabular liners. The Journal of bone and joint surgery. American volume, vol. 86-A, 2004, pp. 1271-82

[72] Affatato S, Bersaglia G, Emiliani D, et al. The performance of gamma- and EtO-sterilised UHMWPE acetabular cups tested under severe simulator conditions . Part 2: wear particle characteristics with isolation protocols. Biomaterials. 2003;24:4045-4055

[73] Affatato S, Spinelli M, Zavalloni M, et al. Ceramic-on-metal for total hip replacement: mixing and matching can lead to high wear. Artificial organs. 2010;34(4):319-23

[74] Carmignato S, Spinelli M, Affatato S, Savio E. Uncertainty evaluation of volumetric wear assessment from coordinate measurements of ceramic hip joint prostheses. Wear. 2011;270(9-10):584-590

[75] Spinelli M, Carmignato S, Affatato S, Viceconti M. CMM – based procedure for polyethylene non-congruous unicompartmental knee prosthesis wear assessment. Wear. 2009;267:753-756.

[76] Teeter MG, Naudie DD, McErlain DD, et al. In vitro quantification of wear in tibial inserts using microcomputed tomography. Clinical orthopaedics and related research. 2011;469(1):107-12.

[77] Day JS, Macdonald DW, Olsen M, et al. Polyethylene wear in retrieved reverse total shoulder components. Journal of shoulder and elbow surgery / American Shoulder and Elbow Surgeons ... [et al.]. 2011:1-8.

[78] Bills P, Brown L, Jiang X, Blunt L. A metrology solution for the orthopaedic industry. Journal of Physics: Conference Series. 2005;13:316-319.

[79] ISO14242-2:2000 – Implants for surgery – wear of total hip-joint prostheses – Part 2: methods of measurement – ISO – 2000

[80] Carmignato S, Dreossi D, Mancini L, Marinello F, Tromba G, Savio E. Testing of x-ray microtomography system using a traceable geometrical standard. Measurent Science and Technology. 2009; 20 084021

[81] Kruth J, Bartscher M, Carmignato S, et al. Computed tomography for dimensional metrology. CIRP Annals - Manufacturing Technology. 2011;60(2):821-842

[82] Tan Y, Kiekens K, Kruth J, Voet A, Dewulf W. Material Dependent Thresholding for Dimensional X-ray Computed Tomography. International Symposium on Digital Industrial Radiology and Computed Tomography. 2011:3-10.

[83] Weckenmann a, Jiang X, Sommer K, et al. Multisensor data fusion in dimensional metrology. CIRP Annals - Manufacturing Technology. 2009;58(2):701-721.

[84] Stock SR. Microcomputed tomography - Methodology and Applications. 2009 CRC Press

[85] Kasperl S, Hiller J, Krumm M. Computed Tomography Metrology in Industrial Research & Development. Development. 2008.

[86] Krumm M, Kasperl S, Franz M. Reducing non-linear artifacts of multi-material objects in industrial 3D computed tomography. NDT & E International. 2007

[87] Meng F, Zhang N, Wang W. Virtual experimentation of beam hardening effect in X-ray CT measurement of multiphase flow. Powder Technology. 2009;194(1-2):153-157.

[88] Macdonald D, Bowden A, Kurtz SM. MicroCT Analysis of Wear and Damage in UHMWPE. Scanning.:511-511.

[89] Teeter MG, Naudie DD, Milner JS, Holdsworth DW. Determination of reference geometry for polyethylene tibial insert wear analysis. The Journal of arthroplasty. 2011;26(3):497-503.

[90] Otsu N. A Tlreshold Selection Method from Gray-Level Histograms. IEEE Transaction on Systems, Man, and Cybernetics. 1979;9(1):62-66.

[91] Liao PS, Chen TS, Chung PC. A Fast Algorithm for Multilevel Thresholding. Journal of Information Science and Engineering. 2001;17:713-727

[92] Pal NR, Pal SK. A review on image segmentation techniques. Pattern recognition. 1993;9:1277-1294

[93] Teeter MG, Naudie DD, Charron KD, Holdsworth DW. Three-dimensional surface deviation maps for analysis of retrieved polyethylene acetabular liners using micro-computed tomography. The Journal of Arthoplasty. 2010;25-2:330-332.

[94] Teeter MG, Naudie DD, Charron KD, Holdsworth DW. Highly cross-linked polyethylene acetabular liners retrieved four to five years after revision surgery: a report of two cases. Journal of the Mechanical Behavior of Biomedical Materials. 2010;3:464-469.

[95] Kiekens K, Tan Y, Kruth J, Voet A, Dewulf W. Parameter Dependent Thresholding for Dimensional X-ray Computed Tomography. International Symposium on digital Industrial Radiology and Computed Tomography. 2011: Poster12.

[96] Martini L, Staffa G, Giavaresi G, Salamanna F, **Parrilli A**, Serchi E, Pressato D, Arcangeli E, Fini M. Long-term results following cranial hydroxyapatite prosthesis implantation in a large skull defect model. Plast Reconstr Surg. 2012 Apr;129(4):625e-35e.

[97] Gladstone HB, McDermott MW, Cooke DD. Implants for cranioplasty. Otolaryngol Clin North Am. 1995;28:381-400.

[98] Pistner H, Reuther J, Reinhart E, Kübler N, Priessnitz B. New hydroxylapatite cement for craniofacial surgery. Mund Kiefer Gesichtschir. 1998;2 Suppl 1:37-40.

[99] Costantino PD, Hiltzik D, Govindaraj S, Moche J. Bone healing and bone substitutes. Facial Plast Surg. 2002;18:13-26.

[100] De Bonis P, Pompucci A, Mangiola A, Rigante L, Anile C. Post-traumatic Hydrocefalus after de compressive craniectomy: an understimated risk factor. Journal of Neurotrauma. 2010;27:1-6.

[101] Szpalski C, Barr J, Wetterau M, Saadeh PB, Warren SM. Cranial bone defects: current and future strategies. Neurosurg Focus. 2010;29(6):E8.

[102] Verheggen R, Merten HA. Correction of skull defects using hydroxyapatite cement (HAC)–evidence derived from animal experiments and clinical experience. Acta Neurochir. 2001;143(9):919–926.

[103] Ducic Y. Titanium mesh and hydroxyapatite cement cranioplasty: a report of 20 cases. J Oral Maxillofacial Surg. 2002;60:272–276.

[104] Staffa G, Nataloni A, Compagnone C, Servadei F. Custom made cranioplasty protheses in porous hydroxy-apatite using 3D design techniques. 7 years experience in 25 patients. Acta Neurochir (Wien). 2007;149:161-170.

[105] Cangini F, Arcangeli E, Nataloni A, Pressato D, Staffa G. Cranial reconstruction surgery: 10 years experience with CustomBone service cranioplasty. Proceedings 12th Meeting Ceramic, cells and tissues, Faenza, Italy; 2009; 170-175,

[106] Cavalcanti S, Pereira C, Mazzonetto R et al. Histological and histomorphometric analyses of calcium phosphate cement in rabbit calvaria. J Craniomaxillofac Surg. 2008;36:354-359.

[107] Ji C, Ahn JG. Clinical experience of the brushite calcium phosphate cement for the repair and augmentation of surgically induced cranial defects following the pterional craniotomy. J Korean Neurosurg Soc. 2010; 47(3):180-184.

[108] Costantino PD, Friedman CD, Jones K, Chow LC, Sisson GA. Experimental hydroxyapatite cement cranioplasty. Plast Reconstr Surg. 1992;90:174-185.

[109] Eppley BL. Hydroxyapatite cranioplasty: I. Experimental results from a new quick-setting material. J Craniofacial Surgery. 2003;14(1):85-88.

[110] Blum KS, Schneider SJ, Rosenthal AD. Methyl methacrylate cranioplasty in children: long term results. Pediatr Neurosurg. 1997;26:33–35.

[111] Jones AC, Milthorpe B, averdunk H, et all. Analysis of 3D bone ingrowth into polymer scaffolds via micro-computed tomography imaging. Biomaterials. 2004;25:4947-4954.

[112] Itokawa H, Hiraide T, Moriya M, et al. A 12 month in vivo study on the response of bone to a hydroxyapatite-polymethylmethacrylate cranioplasty composite. 2007,28:4922-4927.

[113] Cabraja M, Klein M, Lehmann TN. Long-term results following titanium cranioplasty of large skull defects. Neurosurgery Focus. 2009;26(6):1-7.

[114] Ashby R, Rudkin GH, Ishida K, Miller TA. Evaluation of a novel osteogenic factor, bone cell stimulation substance in a rabbit cranial defect model. Plast. Reconstr. Surg. 1996;98:420–426.

[115] Eppley BL. Resorbable biotechnology for craniomaxillofacial surgery. J Craniofac Surg. 1997;8(2):85-6.

[116] Flautre B, Descamps M, Delecourt C, Blary MC, Hardouin P. Porous HA ceramic for bone replacement: role of the Poress and interconnections - experimental study in the rabbit. J Mater Sci Mater Med. 2001;12(8):679-862.

[117] Parfitt AM. Bone histomorphometry: standardization of nomenclature, symbols and units. Summary of proposed system. Bone Miner. 1988;4(1):1-5.

[118] Hildebrand T, Rüegsegger P. A new method for the model-independent assessment of thickness in three-dimensional images. J of Microscopy. 1997;185:67-75.

[119] Costantino PD, Friedman CD, Shindo ML, Houston G, Sisson GA Sr. Experimental mandibular regrowth by distraction osteogenesis. Long-term results. Arch Otolaryngol Head Neck Surg. 1993;119(5):511-516.

[120] Chen TM, Wang HJ, Chen SL, Lin FH. Reconstruction of post-traumatic frontal-bone depression using hydroxyapatite cement. Ann Plast Surg. 2004;52(3):303-308.

[121] Davies JE. Understanding peri-implant endosseous healing. J Dent Educ 2003;67(8):932-949.

[122] Annaz B, Hing KA, Kayser M, Buckland T, Di Silvio L. An ultrastructural study of cellular response to variation in porosity in phase-pure hydroxyapatite. J Microsc. 2004;216(Pt 2):97-109.

[123] Veigel E, Moore RJ, Zarrinkalam MR, et al. Osteopenia in the maxillofacial area: a study in sheep. Osteoporos Int. 2011;22(4):1115-21.

[124] Gugala Z, Gogolewski S. Regeneration of segmental diaphyseal defects in sheep tibiae using resorbable polymeric membranes: a preliminary study. J Orthop Trauma. 1999;13(3):187-95.

[125] Heckman JD, Boyan BD, Aufdemorte TB, Abbott JT. The use of bone morphogenetic protein in the treatment of non-union in a canine model. J Bone Joint Surg Am. 1991;73(5):750-64.

[126] Gosain AK, Santoro TD, Song LS, Capel CC, Sudhakar PV, Matloub HS. Osteogenesis in calvarial defects: contribution of the dura, the pericranium, and the surrounding bone in adult versus infant animals. Plast Reconstr Surg. 2003;112(2):515-27

[127] Martini L, Fini M, Giavaresi G, Giardino R. Sheep model in orthopedic research: a literature review. Comp Med. 2001;51(4):292-299.

[128] Swennen G, Dempf R, Schliephake H. Cranio-facial distraction osteogenesis: a review of the literature. Part II: Experimental studies. Int J Oral Maxillofac Surg. 2002;31(2):123-135.

[129] Cancedda R, Giannoni P, Mastrogiacomo M. A tissue engineering approach to bone repair in large animal models and in clinical practice. Biomaterials. 2007 ;28(29):4240-4250.

[130] Viljanen VV, Lindholm TS. Comparison of native xenogeneic and allogeneic bone morphogenetic proteins in the sheep skull defect assay model. Ann Chir Gynaecol. 1997;86(3):255-9

[131] Gosain AK. Hydroxyapatite cement paste cranioplasty for the treatment of temporal hollowing after cranial vault remodeling in a growing child. J Craniofac Surg. 1997;8(6):506-511.

[132] Gosain AK, Riordan PA, Song L, Amarante MT et al. A 1-year study of osteoinduction in hydroxyapatite-derived biomaterials in an adult sheep model: part II. Bioengineering implants to optimize bone replacement in reconstruction of cranial defects. Plast Reconstr Surg. 2004;114(5):1155-1163.

[133] Ropper AE, Rogers GF, Ridgway EB, Proctor MR. Repair of a large congenital frontal bone defect with autologous exchange cranioplasty. J Neurosurg Pediatr. 2010;6(5):464-467.

[134] Brevi BC, Magri AS, Toma L, Sesenna E. Cranioplasty for repair of a large bone defect with autologous and homologous bone in children. J Pediatr Surg. 2010;45(4):17-20.

[135] Spetzger U, Vougioukas V, Schipper J. Materials and techniques for osseous skull reconstruction. Minim Invasive Ther Allied Technol. 2010 ;19(2):110-121.

[136] Salamanna F, Fini M, **Parrilli A**, Cadossi M, Aldini NN, Giavaresi G, Luciani D, Giannini S. Histological, histomorphometric and microtomographic analyses of retrieval hip resurfacing arthroplasty failed at different times. BMC Musculoskelet Disord. 2013 Jan 30;14:47

[137] McMinn D, Treacy R, Lin K, Pynsent P: Metal on metal surface replacement of the hip: experience of the McMinn prosthesis. Clin Orthop 1996, 329:89–98.

[138] Van Gerwen M, Shaerf DA, Veen RM: Hip resurfacing arthroplasty. Acta Orthop 2010, 81(6):680–3.

[139] McMinn DJ, Daniel J, Ziaee H, Pradhan C: Indications and results of hip resurfacing. Int Orthop 2011, 35(2):231–7.

[140] Spierings PT: Hip resurfacing: expectations and limitations. Acta Orthop 2008, 79(6):727–30.

[141] Shimmin AJ, Back D: Femoral neck fractures following Birmingham hip resurfacing: a national review of 50 cases. J Bone Joint Surg Br 2005, 87-B:463–474.

[142] Zustin J, Krause M, Breer S, Hahn M, von Domarus C, Rüther W, Sauter G, Morlock MM, Amling M: Morphologic analysis of periprosthetic fractures after hip resurfacing arthroplasty. J Bone Joint Surg Am 2010, 92(2):404–10.

[143] Prosser GH, Yates PJ, Wood DJ, Graves SE, de Steiger RN, Miller LN: Outcome of primary resurfacing hip replacement: evaluation of risk factors for early revision. Acta Orthop 2010, 81(1):66–71.

[144] Daniel J, Pynsent PB, McMinn DJ: Metal-on-metal versus polyethylene in hip arthroplasty: a randomized clinical trial. Clin Orthop Relat Res 2004, 422:271.

[145] Ullmark G, Sundgren K, Milbrink J, Nilsson O, Sörensen J: Osteonecrosis following resurfacing arthroplasty. Acta Orthop 2009, 80(6):670–4.

[146] Amstutz HC, Campbell PA, Le Duff MJ: Fracture of the neck of the femur after surface arthroplasty of the hip. J Bone Joint Surg Am 2004, 86:1874–7.

[147] Glyn-Jones S, Pandit H, Kwon YM, Doll H, Gill HS, Murray DW: Risk factors for infammatory pseudotumour formation following hip resurfacing. J Bone Joint Surg Br 2009, 91(12):1566–1574.

[148] Campbell P, Shimmin A, Walter L, Solomon M: Metal sensitivity as a cause of groin pain in metal-on-metal hip resurfacing. J Arthroplasty 2008, 23(7):1080–5.

[149] Daniel J, Ziaee H, Kamali A, Pradhan C, Band T, McMinn DJ: Ten-year results of a double-heat-treated metal-on-metal hip resurfacing. J Bone Joint Surg Br 2010, 92(1):20–7.

[150] Carrothers AD, Gilbert RE, Jaiswal A, Richardson JB: Birmingham hip resurfacing: the prevalence of failure. J Bone Joint Surg Br 2010, 92(10):1344–50.

[151] Amstutz HC, Beaulé PE, Dorey FJ, Le Duff MJ, Campbell PA, Gruen TA: Metal-on-metal hybrid surface arthroplasty: two to six-year follow-up study. J Bone Joint Surg Am 2004, 86-A(1):28–39.

[152] Treacy RB, McBryde CW, Shears E, Pynsent PB: Birmingham hip resurfacing: a minimum follow-up of ten years. J Bone Joint Surg Br 2011, 93(1):27–33.

[153] Ollivere B, Darrah C, Barker T, Nolan J, Porteous MJ: Early clinical failure of the Birmingham metal-on-metal hip resurfacing is associated with metallosis and soft-tissue necrosis. J Bone Joint Surg Br 2009, 91(8): 1025–30.

[154] Giannini S, Cadossi M, Chiarello E, Faldini C, Moroni A, Romagnoli M: Hip resurfacing arthroplasty: a series of 140 consecutive hips with a minimum five year follow-up. A clinical, radiological and histological analysis. Hip Int 2011, 21(1):52–58.

[155] Hildebrand T, Rüegsegger P: A new method for the model-independent assessment of thickness in three-dimensional images. J Microscopy 1997, 185:67–75.

[156] Martini L, Staffa G, Giavaresi G, Salamanna F, **Parrilli A**, Serchi E, Pressato D, Arcangeli E, Fini M: Long-term Results following a Cranial Hydroxyapatite Prosthesis implantation in a large Skull Defect Model. Plast Reconstr Surg 2012, 129(4):625–35.

[157] Parfitt AM: Bone histomorphometry: standardization of nomenclature, symbols and units Summary of proposed system. Bone Miner 1988, 4(1):1–5.

[158] Steffen RT, Athanasou NA, Gill HS, Murray DW: Avascular necrosis associated with fracture of the femoral neck after hip resurfacing: histological assessment of femoral bone from retrieval specimens. J Bone Joint Surg Br 2010, 92(6):787–93.

[159] Mont MA, Jones LC, Einhorn TA, Hungerford DS, Reddi AH: Osteonecrosis of the femoral head. Potential treatment with growth and differentiation factors. Clin Orthop Relat Res 1998, 355(Suppl):314–335.

[160] Morlock MM, Bishop N, Rüther W, Delling G, Hahn M: Biomechanical, morphological, and histological analysis of early failures in hip resurfacing arthroplasty. Proc Inst Mech Eng H 2006, 220(2):333–44.

[161] Lazarinis S, Milbrink J, Hailer NP: Avascular necrosis and subsequent femoral neck fracture 3.5 years after hip resurfacing: a highly unusual late complication in the absence of risk factors--a case report. Acta Orthop 2008, 79(6):763–768.

[162] Pal B, Gupta S, New AM: Influence of the change in stem length on the load transfer and bone remodelling for a cemented resurfaced femur. J Biomech 2010, 43(15):2908–14.

[163] Zlotorowicz M, Czubak J, Kozinski P, Boguslawska-Walecka R: Imaging the vascularisation of the femoral head by CT angiography. J Bone Joint Surg Br 2012, 94(9):1176–9.

[164] McBryde CW, Revell MP, Thomas AM, Treacy RB, Pynsent PB: The influence of surgical approach on outcome in Birmingham hip resurfacing. Clin Orthop Relat Res 2008, 466(4):920–6.

[165] Ganz R, Gill TJ, Gautier E, Ganz K, Krügel N, Berlemann U: Surgical dislocation of the adult hip a technique with full access to the femoral head and acetabulum without the risk of avascular necrosis. J Bone Joint Surg Br 2001, 83(8):1119–24.

[166] **Parrilli A**, Maglio M, Giavaresi G, Pierini M, Lucarelli E, Preve E, Prosperi S, Piccinini M, Bucciotti F, Donati D, Fini M, Giannini S. MicroCT preliminary analysis on granules charachteristics in an in vivo study using a new injectable multiphasic bone substitutes based on gel-coated Osprolife HA/TTCP. MiMe 1st International Conference on Materials in Medicine, Faenza, Italy, 8-11 October 2013.